

# Auger electron-emitting nanotheranostics for image-guided radio-chemotherapy against triple-negative breast cancer

Von der Fakultät für Mathematik, Informatik und Naturwissenschaften der RWTH  
Aachen University zur Erlangung des akademischen Grades einer Doktorin der  
Naturwissenschaften genehmigte Dissertation

vorgelegt von

Laura Schäfer (M. Sc.)

geboren in Eschweiler

Berichter: Univ.-Prof. Dr. rer. nat. Stefan Schillberg  
Univ.-Prof. Dr. rer. nat. Andreas Herrmann

Tag der mündlichen Prüfung: 02.06.2025

Diese Dissertation ist auf den Internetseiten der Universitätsbibliothek verfügbar.



To my family and loved ones.

## Declaration of Authorship

Laura Schäfer

erklärt hiermit, dass diese Dissertation und die darin dargelegten Inhalte die eigenen sind und selbstständig, als Ergebnis der eigenen originären Forschung, generiert wurden.

Hiermit erkläre ich an Eides statt

1. Diese Arbeit wurde vollständig oder größtenteils in der Phase als Doktorand dieser Fakultät und Universität angefertigt;
2. Sofern irgendein Bestandteil dieser Dissertation zuvor für einen akademischen Abschluss oder eine andere Qualifikation an dieser oder einer anderen Institution verwendet wurde, wurde dies klar angezeigt;
3. Wenn immer andere eigene- oder Veröffentlichungen Dritter herangezogen wurden, wurden diese klar benannt;
4. Wenn aus anderen eigenen- oder Veröffentlichungen Dritter zitiert wurde, wurde stets die Quelle hierfür angegeben. Diese Dissertation ist vollständig meine eigene Arbeit, mit der Ausnahme solcher Zitate;
5. Alle wesentlichen Quellen von Unterstützung wurden benannt;
6. Wenn immer ein Teil dieser Dissertation auf der Zusammenarbeit mit anderen basiert, wurde von mir klar gekennzeichnet, was von anderen und was von mir selbst erarbeitet wurde;
7. Ein Teil oder Teile dieser Arbeit wurden zuvor veröffentlicht, und zwar in:

L. Schäfer, J. Pena, A. Wang, T. Lammers, A. Mottaghy-Morgenroth, F. Mottaghy, E. Buhl, C. Bolm, 2023. Auger Electron Emitter Labelled PARPi Drug Delivery System for TNBC Therapy. Nuklearmedizin 2023; 62(02): 140,  
DOI: 10.1055/s-0043-1766310

Datum, Unterschrift:

Aachen, den 08.07.2025

---

## Scientific Publications

- Current Approaches of Nuclear Molecular Imaging in Breast Cancer  
**Schäfer, Laura**, Betül Altunay, Amelie Heesch, Thiemo van Nijnatten, Sofia Vaz, Malik Eid Juweid, and Felix Manuel Mottaghy.  
Cancers 2025 17, no. 13: 2105. <https://doi.org/10.3390/cancers17132105>
- Neural Stem Cells as Carriers of Nucleoside-Conjugated Nanogels: A New Approach toward Cell-Mediated Delivery Agnieszka Morgenroth, Fatima Baazaoui, Aisa Hosseinnejad, **Laura Schäfer**, Andreas Vogg, Smriti Singh, and Felix M. Mottaghy  
ACS Applied Materials & Interfaces 2023 15 (18), 21792-21803 DOI: 10.1021/acsami.2c23283
- Validation of Dual-Action Chemo-Radio-Labeled Nanocarriers with High Efficacy against Triple-Negative Breast Cancer Shaista Ilyas, Sabri E. M. Sahnoun, Annika Szymura, Jonas Pes, Shahin Habib, Alexandru Florea, **Laura Schäfer**, Eva Miriam Buhl, Agnieszka Morgenroth, Pardes Habib, Felix M. Mottaghy, and Sanjay Mathur  
ACS Applied Materials & Interfaces 2023 15 (42), 48963-48977 DOI: 10.1021/acsami.3c10579
- PARP targeted Auger emitter therapy with [125I]PARPi-01 for triple-negative breast cancer. Ambur Sankaranarayanan, R., Florea, A., Allekotte, S., A. T. J. Vogg, J. Maurer, **Laura Schäfer**, C. Bolm, S. Terhorst, A. Classen, M. Bauwens, A. Morgenroth, F. M. Mottaghy  
EJNMMI Res 12, 60 (2022). <https://doi.org/10.1186/s13550-022-00932-9>
- Radiosynthesis, Quality Control, and Small Animal Positron Emission Tomography Imaging of <sup>68</sup>Ga-labelled Nano Molecules. Betül Altunay, Matthias Bauwens, **Laura Schäfer**, Amelie Heesch, Agnieszka Morgenroth, Felix M. Mottaghy, Alexandru Florea  
J Vis Exp. 2024 Oct 4;(212). doi: 10.3791/67048. PMID: 39431771.
- **L. Schäfer**, J. Pena, A. Wang, T. Lammers, A. Mottaghy-Morgenroth, F. Mottaghy, E. Buhl, C. Bolm, 2023. Auger Electron Emitter Labelled PARPi Drug Delivery System for TNBC Therapy.  
Nuklearmedizin 2023; 62(02): 140, DOI: 10.1055/s-0043-1766310

# Table of Contents

<b>Declaration of Authorship</b>	<b>II</b>
<b>Scientific Publications</b>	<b>III</b>
<b>Table of Contents</b>	<b>IV</b>
<b>List of Abbreviations</b>	<b>VI</b>
<b>List of Figures</b>	<b>VIII</b>
<b>List of Tables</b>	<b>X</b>
<b>Summary</b>	<b>XI</b>
<b>Zusammenfassung</b>	<b>XIII</b>
<b>1 Introduction</b>	<b>1</b>
1.1 <i>Radiotheranostics in Oncology</i>	1
1.1.1 Radionuclide selection - Auger Electron Emitters	3
1.1.2 Auger Electron Emitters in the Clinic	5
1.2 <i>Radiotheranostics for Triple-Negative Breast Cancer</i>	6
1.2.1 The BRCA Mutation – Biological Effects and Clinical Implications	7
1.2.2 Synthetic Lethality Induced by PARP Inhibitors in BRCA <sup>mut</sup> TNBC	8
1.2.3 Radiotheranostic PARP Inhibitors and Clinical Challenges	10
1.3 <i>Radio-Nanomedicine: Nanocarriers for Radiotheranostics</i>	13
1.3.1 Radioactive Nanomedicines for Cancer Theranostics	16
1.3.2 Formulation of PARP Inhibitors in Polymeric Micelles	19
1.3.3 $\pi$ electron-stabilized PEGylated HPMA-Based Micelles	21
1.4 <i>Motivation and Goals</i>	22
<b>2 Materials and Methods</b>	<b>24</b>
2.1 <i>Equipment and Chemicals</i>	24
2.1.1 Chemicals, Kits and Consumables	24
2.1.2 Buffers	27
2.1.3 Cell Lines	27
2.1.4 Antibodies	28
2.1.5 Devices	28
2.1.6 Softwares	29
2.2 <i>Methods</i>	30

	V
2.2.1 Statistical Analysis	30
2.2.2 High-Performance Liquid Chromatography (HPLC)	30
2.2.3 Radiolabeling of PARPi-01	30
2.2.4 Micelle Synthesis and Characterization	31
2.2.5 <i>In Vitro</i> Experiments	34
2.2.6 <i>In Vivo</i> Experiments	36
2.2.7 <i>Ex Vivo</i> Experiments	40
<b>3 Results and Discussion</b>	<b>42</b>
3.1 <i>Formulation of Auger Electron-Emitting PARP inhibitors in Polymeric Micelles</i>	42
3.1.1 Preparation of PARP inhibitor Single-Loaded $\pi$ electron-stabilized HPMA-based micelles	42
3.1.2 Co-Loading non-radioactive and radioactive PARP inhibitor in Polymeric Micelles	44
3.1.3 Concentrated Fluorescent Micelles for <i>In Vivo</i> Applications	50
3.2 <i>In Vitro Evaluation of Drug-Loaded Micelles in TNBC</i>	54
3.2.1 PARP Status in TNBC and Comparative Uptake of Free and Encapsulated Forms	54
3.2.2 Protection of the Radiotracer from Enzymatic Degradation Using Polymeric Micelles	58
3.2.3 Synergistic Cytotoxicity of I-PARPi-01 and [ $^{125}$ I]-PARPi-01 <i>in vitro</i>	60
3.3 <i>In Vivo Evaluation of PARP inhibitor-Loaded Micelles in TNBC Xenografts</i>	67
3.3.1 Biodistribution and Tumor Accumulation of [ $^{123}$ I]-PARPi-01 in Polymeric Micelles	67
3.3.2 <i>In vivo</i> therapy study of [ $^{125}$ I]-PARPi-01 in Polymeric Micelles	79
3.4 <i>Ex Vivo Evaluation</i>	89
3.4.1 Micelle Therapy Induces Enhanced Cytotoxic Effects in TNBC	90
3.4.2 Interactions of Co-Loaded Micelles with the Tumor Microenvironment	92
<b>4 Conclusions and Outlook</b>	<b>96</b>
<b>5 References</b>	<b>98</b>
<b>6 Acknowledgments</b>	<b>113</b>

## List of Abbreviations

Abbreviation	Definition
ACN	Acetonitrile
ATO	Active targeting olaparib nanoparticles
BFCs	Bifunctional chelators
BRCA1/2	Breast cancer gene 1/2
BRCA <sup>mut</sup>	Breast cancer gene mutated
BSA	Bovine serum albumin
CD	Cluster of differentiation
Cy7	Cyanine 7
DLS	Dynamic light scattering
DMEM	Dulbecco's modified eagle's medium
DSB	Double-strand breaks
EE	Encapsulation efficiency
EGF	Endothelial growth factor
EPR	Enhanced permeability and retention
EtOH	Ethanol
FBS	Fetal bovine serum
FDA	Food and drug administration
H&E	Hematoxylin and eosin
HER2	Human epidermal growth factor receptor 2
HPLC	High-performance liquid chromatography
HR	Homologous recombination
ips	impulses per second
iv	Intravenous
JNK	C-jun N-terminal kinase
LC	Loading efficiency
LET	Linear energy transfer
MIP	Maximum intensity projection
mPEG- <i>b</i> - p(HPMAm-Bz)	mPEG- <i>b</i> -pHPMAm (methoxy poly(ethylene glycol)- <i>b</i> -(N-(2-benzoyloxypropyl) methacrylamide))



MPS	Mononuclear phagocyte system
NC	Nanocarrier
NHEJ	Non-homologous end joining
NIS	Sodium iodide symporter
NOD.Scid	NOD.CB17-Prkdcscid/scid/Rj
p.i	Post-injection
PARP	Poly(ADP-ribose) polymerase
PARPi	Poly(ADP-ribose) polymerase inhibitor
PBS	Dulbecco's phosphate buffered saline
PDI	Polydispersity index
PET	Positron emission tomography
PLGA	Poly(lactic-co-glycolic acid)
PRRT	Peptide receptor radionuclide therapy
PTX	Paclitaxel
RBE	Relative biological effectiveness
RCA I	Ricinus communis agglutinin I
RPMI	Roswell park memorial institute media
RT	Room temperature
SD	Standard deviation
SPECT	Single photon emission computed tomography
SSBs	Single-strand DNA breaks
TBR	Target-to-background ratio
TEM	Transmission electron microscopy
TFA	Trifluoroacetic acid
THF	Tetrahydrofurane
TME	Tumor microenvironment
TNBC	Triple-negative breast cancer

## List of Figures

Figure 1. Different types of radiation for imaging and therapy.	3
Figure 2. PARP inhibitors in triple-negative breast cancer treatment.	10
Figure 3. Biodistribution results of [ $^{123}\text{I}$ ]-PARPi-01 in NOD/SCID mice bearing-subcutaneous MDA-MB-231 xenograft. [79]	13
Figure 4. Overview, functionalization and radiolabeling of different nanocarriers for radio theranostics.	15
Figure 5. Overview of this PhD thesis work: Auger electron-emitting nanotheranostics for image-guided radio-chemotherapy against triple-negative breast cancer.	23
Figure 6. Micelle synthesis procedure.	32
Figure 7. Formulation and characterization of PARPi-loaded [mPEG- <i>b</i> -p(HPMA-Bz)]-based micelles.	44
Figure 8. Radiolabeling of [ $^{125}\text{I}$ ]-PARPi-01.	46
Figure 9. Co-loading of non-radioactive and radioactive PARPi in mPEG- <i>b</i> -p(HPMAm-Bz) polymeric micelles.	49
Figure 10. Pharmaceutical evaluation of I-PARPi-01 single-loaded Cy7-labelled polymeric micelles.	52
Figure 11. PARP1 expression and tracer uptake in TNBC.	56
Figure 12. Enzymatic degradation of radiotracer.	59
Figure 13. Cell viability assessment of I-PARPi-01 treated breast cancer and non-tumorigenic cell lines.	61
Figure 14. Assessment of DNA damage in the HCC1937 TNBC cell line following treatment with combinations of I-PARPi-01 and [ $^{125}\text{I}$ ]-PARPi-01.	64
Figure 15. <i>In vivo</i> biodistribution study setup.	69
Figure 16. <i>In vivo</i> biodistribution of [ $^{123}\text{I}$ ]-PARPi-01 formulations.	71
Figure 17. Target-to-background ratios of different [ $^{123}\text{I}$ ]-PARPi-01 formulations.	75
Figure 18. Impact of different formulations of [ $^{123}\text{I}$ ]-PARPi-01 radiotracer on tumor accumulation.	78
Figure 19. Comprehensive overview of the <i>in vivo</i> therapy study conducted to evaluate the effects of various formulations of [ $^{125}\text{I}$ ]-PARPi-01.	80

Figure 20. Therapeutic efficacy of three injections with co-loaded micelles in HCC1937 BRCA<sup>mut</sup> xenograft models. 81

Figure 21. Drug clearance *in vivo*. 84

Figure 22. Therapeutic efficacy of one injection with co-loaded micelles in HCC1937 BRCA<sup>mut</sup> xenograft models. 87

Figure 23. Therapy-induced DNA damage evaluation of tumor and off-target organs. 91

Figure 24. *Ex vivo* co-localization of Cy7-labeled micelles with leaky blood vessels and macrophages. 93

Figure 25. Radiotracer is predominantly trapped in extra cellular matrix of the tumor. 95

## List of Tables

Table 1. Characteristics of different types of radiation.	4
Table 2. Preclinical theranostic applications of radiolabeled PARP-ligands over the past five years.	12
Table 3. Overview of radiolabeled nanocarriers targeting triple-negative breast cancer.	17
Table 4. Polymeric nanoformulations of PARP inhibitors.	20
Table 5. Characteristics of cell lines used in this study.	54

## Summary

Radio-nanomedicine, the combination of radiation technology or nuclear medicine with nanomedicine, is an emerging and promising field in nuclear imaging and therapy. BRCA-mutated (BRCA<sup>mut</sup>) triple-negative breast cancer (TNBC), the most aggressive form of breast cancer that is often treated with poly(ADP-ribose) polymerase inhibitors (PARPi) has been evaluated as a potential tumor entity using radio-nanomedicine. While PARPi can prolong survival, they do not provide a curative effect. Auger electron-emitting radiotherapeutics have shown promise for radionuclide therapy of BRCA<sup>mut</sup> TNBC by effectively inducing DNA double-strand breaks, when located in close proximity to the DNA. In this context, an Auger-electron emitting therapeutic based on [<sup>123/125</sup>I]-PARPi-01 was recently developed and evaluated for BRCA<sup>mut</sup> TNBC. However, as many other radiotracers, it presented several drawbacks when administered *in vivo*, particularly low water-solubility, a rapid enzymatic degradation, rapid clearance, and low tumor accumulation, thereby resulting in suboptimal therapeutic performance.

To overcome these issues, encapsulating drugs within nanocarriers has shown promise. Nanoscale drug delivery systems have proven effective in enhancing drug stability and improving biodistribution and tumor targeting, together potentiating anticancer therapy performance. Among the different drug delivery systems, polymeric micelles are widely used for hydrophobic drug delivery and hold high promise as modular platforms for multidrug delivery, thus enabling drug combination nanotherapies.

In this thesis, a theranostic polymeric micelle co-formulation of Auger electron-emitting and SPECT-imageable <sup>123/125</sup>I-PARPi with the non-radioactive counterpart was developed for improved radio-chemotherapy combination in BRCA<sup>mut</sup> TNBC. For that purpose, physically stabilized micelles have been employed based on mPEG-*b*-p(HPMAm-Bz) block copolymers to co-encapsulate the hydrophobic radiolabeled poly (ADP-ribose) polymerase inhibitor [<sup>123/125</sup>I]-PARPi-01 and the non-radioactive counterpart I-PARPi-01. The co-loaded micelles showed diameters around 70 nm, with homogeneous size distribution and spherical morphology. Both drugs were efficiently encapsulated and effectively co-delivered by the micelles. The micelle formulation improved the PARPi tracer stability in biological media. *In vivo* SPECT/CT measurements using <sup>123</sup>I

corroborated these findings and demonstrated prolonged circulation times, enhanced tumor accumulation, and slowed tracer degradation when encapsulated in polymeric micelles as compared to the free tracer. The double (Auger electron-emitting  $^{125}\text{I}$ -radioactive and non-radioactive PARPi) drug-loaded micelles showed improved antitumor efficacy after a single intravenous administration, with a 50 % reduction in tumor volume observed after 14 days of treatment, in comparison to the co-administration of the free drugs (also confirmed via *ex vivo* immunohistochemical analysis), while being well-tolerated.

Taken together, this newly developed Auger electron emitting co-loaded micelle formulation demonstrated enhanced *in vivo* tracer stability, prolonged blood circulation, and improved tumoral uptake, together potentiating PARPi therapeutic performance in BRCA<sup>mut</sup> TNBC and underscoring the potential of radio-nanomedicine combinations in difficult-to-treat cancers, including beyond TNBC and towards eventual clinical investigations.

## Zusammenfassung

Radio-Nanomedizin, die Kombination von Strahlentechnologie oder Nuklearmedizin mit Nanomedizin, ist ein aufstrebendes und vielversprechendes Feld in der nuklearmedizinischen Bildgebung und Therapie. Ein besonderes Interessengebiet ist der BRCA-mutierte (BRCA<sup>mut</sup>) triple-negative Brustkrebs (TNBC), eine aggressive Krebsform, die häufig mit Poly(ADP-Ribose)-Polymerase-Inhibitoren (PARPi) behandelt wird. Obwohl PARPi das Überleben verlängern können, bieten sie keinen kurativen Effekt. Auger-Elektron-emittierende Radiopharmaka haben sich als vielversprechend für die Radionuklidtherapie von BRCA<sup>mut</sup> TNBC erwiesen, indem sie effektiv DNA-Doppelstrangbrüche induzieren, wenn sie sich in unmittelbarer Nähe zur DNA befinden. In diesem Zusammenhang wurde bereits ein Auger-Elektron-emittierendes Radiopharmakon [<sup>123/125</sup>I]I-PARPi-01 entwickelt und in BRCA<sup>mut</sup> TNBC evaluiert. Allerdings wies es, wie viele andere Radiopharmaka, mehrere Nachteile *in vivo* auf, insbesondere eine geringe Wasserlöslichkeit, eine schnelle enzymatische Zersetzung, eine rasche Ausscheidung und eine geringe Tumorakkumulation, was zu einer suboptimalen therapeutischen Wirksamkeit führte.

Um diese Probleme zu beheben, hat sich die Verpackung von kleinen Molekülen in Nanopartikeln als vielversprechend erwiesen. Sogenannte „Drug-Delivery-Systeme“ im nanogrößen-Bereich haben sich als effektiv erwiesen, um die Stabilität von Arzneimitteln zu erhöhen und die Biodistribution zu verbessern, wodurch die therapeutische Wirksamkeit der Arzneimittel gesteigert wird.

Unter den verschiedenen Drug-Delivery-Systemen werden polymere Mizellen häufig für die Verpackung hydrophober Arzneimittel gegen Krebs verwendet. Sie bieten zudem eine modulare Plattform, die die simultane Verpackung mehrerer Arzneimittel ermöglicht, wodurch Kombinationsnanotherapien realisiert werden können.

In dieser Dissertation wurden physikalisch stabilisierte Mizellen auf der Basis von mPEG-*b*-p(HPMAm-Bz) Blockcopolymeren verwendet, um den hydrophoben, radioaktiv markierten Poly(ADP-Ribose)-Polymerase-Inhibitor [<sup>123/125</sup>I]I-PARPi-01 und das nicht-radioaktive Gegenstück I-PARPi-01 simultan zu verpacken. Die co-beladenen Mizellen wiesen Durchmesser von etwa 70 nm auf, mit einer homogenen Größenverteilung und sphärischer Morphologie. Die Verkapselungseffizienz für beide Moleküle lag bei über 80

%, und beide Moleküle wurden effektiv aus den Mizellen freigesetzt. Die Verpackung des Radiopharmakons in Mizellen verbesserte seine Stabilität *in vitro* um etwa das 10-fache. *In vivo* SPECT/CT-Messungen unter Verwendung von  $^{123}\text{I}$  bestätigten diese Ergebnisse und zeigten eine verlängerte Zirkulationszeit, verbesserte Tumorakkumulation und verlangsamte enzymatische Zersetzung des Radiopharmakons, wenn er in polymeren Mizellen im Vergleich zum freien Radiopharmakon verpackt war. Die doppelt (radioaktiv und nicht-radioaktiv) beladenen Mizellen zeigten, im Vergleich zur Co-Verabreichung der freien Arzneimittel, nach einer einmaligen intravenösen Verabreichung eine verbesserte antitumorale Wirksamkeit. 14 Tage nach der Verabreichung wurde eine Reduktion des Tumorumfanges um 50 % festgestellt. Darüber hinaus bestätigten *ex vivo* immunhistochemische Analysen der Tumoren diese Ergebnisse, indem sie zytotoxische Effekte in der Gruppe, die mit den Mizellen behandelt wurde, zeigten, während in den Exkretionsorganen keine zytotoxischen Effekte festgestellt werden konnten.

Zusammenfassend zeigte diese neu entwickelte co-beladene Mizellenformulierung *in vivo* eine verbesserte Abschirmung des Radiopharmakons vor enzymatischer Degradierung, eine verlängerte Blutzirkulation und eine verbesserte tumorale Aufnahme, was insgesamt zu einer erhöhten therapeutischen Wirksamkeit in einem BRCA-mutierten triple-negativen Brustkrebsmodell im Vergleich zur Verabreichung der Verbindungen in ihrer nicht verpackten Form führte. Das aufstrebende Feld der Radio-Nanomedizin birgt das Potenzial, die Wirksamkeit und Sicherheit der traditionellen endogenen Strahlentherapie zu verbessern.



# 1 Introduction

## 1.1 Radiotheranostics in Oncology

In the beginning of the 20<sup>th</sup> century, the German Nobel laureate Paul Ehrlich introduced the concept of the "magic bullet" [1], envisioning drugs with precise targeting abilities to eliminate diseases without harming healthy tissues. Ehrlich's groundbreaking work in dyes, histology, and immunology paved the way for modern chemotherapy and targeted therapies in medicine [2]. Over a century later, the "magic bullet" concept continues to shape the development of tailored, safe treatments for diseases like cancer, now referred to as personalized medicine, targeted medicine, or precision medicine [3].

The term "theranostics", officially coined in the early 2000s refers to the combination of therapy and diagnostics [4]. While the term may be relatively new, the concept of theranostics has already been utilized before. A theranostic system combines therapeutic interventions with diagnostic information tailored to a specific target [5]. While it can be applied to multiple different diseases, the term theranostics has been often related in the literature to the application of nuclear medicine in oncology. This includes the application of radionuclide isotopes for both diagnostics and therapy, leading to the specialized term "radiotheranostics" [6]. Radiotheranostics leverage the principle of combining radioactive isotopes with specific molecules, monoclonal antibodies and their fragments, or other (macromolecular) agents that actively target mechanisms, specific receptors or biomarkers crucial to a particular disease, such as cancer [5, 7]. This targeted approach enables precise treatment while minimizing damage to surrounding healthy tissues [5]. The combination of radionuclides and targeting molecules is referred to as radiopharmaceuticals, radiotracers, or radioligands [6].

The diagnostic aspect of radiotheranostics often involves specific imaging techniques, such as positron emission tomography (PET) or single photon emission computed tomography (SPECT). These imaging modalities are utilized to assess the presence and quantity of specific molecular targets, particularly in cancer lesions across the body [5, 8]. This information helps to identify the extent of the diseases, as well as which patients

## Introduction

would benefit from radiotracer therapy approaches, also known as molecular radiotherapy, endoradiotherapy, or radioligand therapy [8]. PET, which is the most sensitive diagnosis method of the two, utilizes  $\gamma$ -rays produced in the process of positron–electron annihilation and requires radionuclides emitting positrons [7]. SPECT uses a series of contiguous two-dimensional images of the distribution of the radiotracer using  $\gamma$ -emitters to provide a three-dimensional distribution of radiotracers [7]. PET and SPECT exhibit high sensitivity by enabling the detection of radiolabeled probes within the range of approximately  $10^{-11}$  to  $10^{-12}$  molecules and  $10^{-10}$  to  $10^{-11}$  molecules, respectively [7]. This sensitivity facilitates the acquisition of high-quality three-dimensional images, which are especially valuable for identifying and characterizing neoplasms.

Similarly, radionuclide therapy, which constitutes the therapeutic component of radiotheranostics, utilizes radiotracers designed to specifically target and kill diseased/malignant cells [6]. Since the beginning of the 20<sup>th</sup> century, it has been recognized that administering a sufficient radiation dose to tumors at an appropriate rate leads to the destruction of cancer cells [9]. While the radionuclides used for nuclear medicine imaging typically emit  $\gamma$ -rays, capable of penetrating deeply into the body, those employed for therapeutic purposes need to emit radiation with a relatively short path length (Figure 1A) [7]. This characteristic is crucial for ensuring that the radiation energy is deposited locally, thereby minimizing exposure and potential damage to surrounding healthy tissues [8]. In the context of radionuclide therapy, three types of radiation are particularly significant:  $\beta$ -particles,  $\alpha$ -particles, and Auger electrons (Figure 1B) [7]. Each of these types of radiation has distinct properties and mechanisms of action, making them suitable for different therapeutic applications based on the specific characteristics of the disease being treated (see chapter 1.1.1).

## Introduction

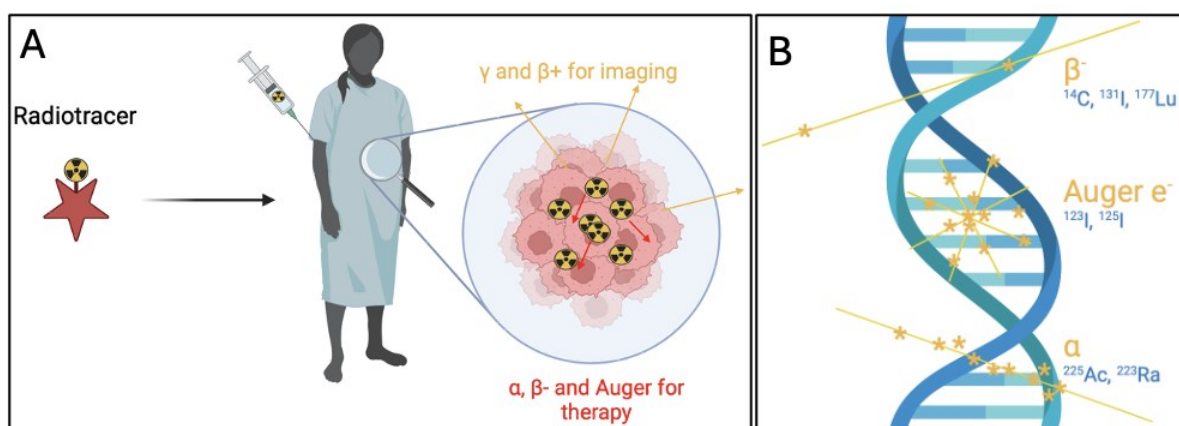


**Figure 1. Different types of radiation for imaging and therapy. (A)** Introductory overview of radiotheranostics. Specific agents may be labeled with a  $\gamma$ -emitting radionuclide for PET/SPECT imaging, or with an  $\alpha$ -,  $\beta^-$  particle- or Auger electron-emitting radionuclide suitable for therapy. **(B)** Illustration of local densities of therapeutic ionization processes (\*), which are produced along the travel path of emitted  $\alpha$ - and  $\beta^-$  particles, and Auger electrons ( $e^-$ ) [10].

Patients with metastatic cancers are often not suitable candidates for standard curative external-beam radiotherapy or surgical interventions, necessitating the use of systemic therapies such as radiotracers or chemotherapy to address both the primary tumor and distant metastases [11]. Radiotheranostics are therefore becoming increasingly important in the field of oncology. A wide variety of radiotracers are currently under development and investigation, allowing for personalized therapy planning for each individual patient, maximizing the destruction of cancer cells while minimizing damage to healthy tissues [6].

This precision not only enhances treatment efficacy but also facilitates personalized therapy planning, ensuring that each patient receives tailored interventions based on their specific tumor characteristics [12, 13]. As research continues to expand the repertoire of available radiotracers, the role of radiotheranostics in oncology will become increasingly vital, paving the way for improved outcomes and more effective management of (metastatic) cancers.

### 1.1.1 Radionuclide selection - Auger Electron Emitters

In addition to the general consideration of the type of radiation emitted, there are several key factors to take into account when choosing the most suitable radionuclide (Table 1). Firstly, the size of the targeted structures should align with the range of the emitted radiation. Variability in the uptake of the carrier molecule could also impact the optimal

## Introduction

range; greater heterogeneity can be balanced out by using emitters with longer ranges. Careful consideration should be also given to the half-life of the radionuclide; the pharmacokinetics of the carrier molecule will dictate the best timing for delivering the maximum energy to the target tissue. The number of emitted photons is crucial for both radiation safety and imaging strategies. While potential radioactive decay products may contribute to the total energy released, their potential redistribution should be taken into consideration [14].

**Table 1. Characteristics of different types of radiation.** Overview and characteristics of different types of therapeutic radiation (LET = Linear Energy Transfer, RBE = Relative Biological Effectiveness) [14].

Type of Radiation	Particle	Mass [kg]	Typical Energy	Typical Range in Tissue	LET [keV/ $\mu$ m]	RBE
$\alpha$	2 protons, 2 neutrons	$6.6 \times 10^{-27}$	Discrete; ~ 4 - 10 MeV	~ 20 - 70 $\mu$ m	~ 50 - 300	~5
$\beta^-$	Electron	$9.1 \times 10^{-31}$	Continuous; max. of some hundred keV to some MeV	Less than 1 mm to some mm	~ 0.1 - 2	~1
<b>Auger electron</b>	Electron	$9.1 \times 10^{-31}$	< 10 keV	< 1 $\mu$ m	~ 4 - 26	~1 or higher

The linear energy transfer (LET) is a physical parameter that characterizes the energy loss of charged particles per unit length. This value is influenced by the mass, charge, and energy of the particle and can vary along the particle's trajectory as it dissipates energy while moving through a material. Generally,  $\alpha$ -particles possess higher LET values compared to Auger electrons, with Auger electrons having higher LET values than  $\beta$ -particles (Table 1) [10]. Auger electrons are produced through processes like electron capture or internal conversion following an isomeric transition, distinguishing them from  $\beta$ -particles. They are often released in cascades and have a very limited range, leading to their elevated LET values [15, 16].

In addition to its correlation with range, the LET plays a significant role in selecting the appropriate emitter due to its potential influence on the Relative Biological Effectiveness

## Introduction

(RBE)[14]. The RBE quantifies the impact of radiation, such as cell destruction, and is influenced by both the characteristics of the radiation and biological variables. It represents the biologically equivalent absorbed doses of a specific radiation concerning a reference radiation (typically 250 keV photons) [14]. Auger electrons have been associated with increased RBE values when they are localized within the nucleus of cells. Even in cases where the emitters are not directly incorporated into the nucleus, indirect effects may lead to cell death, caused by radical species that are produced during the radiolysis of water by these electrons [15, 16]. The biological effects produced by Auger electrons are critically dependent on their sub-cellular (and nuclear) localization due to their very short particle range. Considerations of cellular uptake and intracellular localization are, therefore, especially important for Auger electron emitters [14, 15]. Research conducted in *in vitro* cell cultures has demonstrated that when combined with targeting agents capable of directing these short-range radiations to the vicinity of cellular DNA, these emitters can lead to highly efficient and precise destruction of tumor cells [17-19]. The most common Auger electron emitters include bromine-77 ( $^{77}\text{Br}$ ), indium-111 ( $^{111}\text{In}$ ), iodine-123 ( $^{123}\text{I}$ ), and iodine-125 ( $^{125}\text{I}$ ).

### 1.1.2 Auger Electron Emitters in the Clinic

Currently, there are no Food and Drug Administration (FDA), or European Medicines Agency approved therapeutic treatments utilizing Auger electron emitters. However, diagnostic radiotracers coupled to radionuclides, which decay through electron capture and internal conversion processes leading to the generation of Auger electrons in smaller proportions, have been approved for a long time, such as technetium-99m ( $^{99\text{m}}\text{Tc}$ ),  $^{123}\text{I}$ , and  $^{111}\text{In}$  [20-22].

While some clinical trials involving Auger electron emitters for therapeutic purposes have been studied over the past twenty years, none have transitioned into standard clinical practice so far. One reason might be that, unlike  $\alpha$ -emitters, Auger electrons still pose a risk of significant photon irradiation and free radical generation [23]. For instance, in peptide receptor radionuclide therapy (PRRT), yttrium-90 ( $^{90}\text{Y}$ )-labeled somatostatin analogs resulted in lower red marrow absorbed doses compared to  $^{111}\text{In}$  analogs, primarily due to reduced photon emissions from the entire body [24].

## Introduction

Nevertheless, the future of cancer therapies using Auger electron emitters is promising, as these high-energy but short-range particles have the potential to selectively destroy tumor cells while sparing the healthy tissues around. By advancing carrier molecules that protect and selectively deliver these Auger electron emitters to tumor cells, safe and effective therapies can be developed. Additionally, combination therapies with other treatment modalities such as chemotherapy or immunotherapy could further enhance treatment efficacy.

Currently, there are four clinical trials investigating the use of the  $\beta^-$ /Auger electron emitter  $^{161}\text{Tb}$  for the treatment of castration-resistant prostate cancer (NCT06343038, NCT05521412, NCT04833517) and gastroenteropancreatic neuroendocrine tumors (NCT05359146). Furthermore, many clinical studies investigate  $^{125}\text{I}$  seed brachytherapy to treat several kinds of cancer (NCT04077710, NCT06062589, NCT05421507, NCT05869474, NCT05322356, NCT05608213, and more). Additionally,  $^{123}\text{I}$  (NCT05591092, NCT04510311) and  $^{111}\text{In}$  (NCT05945875, NCT05901545, NCT05605522) are under clinical investigation for imaging applications.

Therefore, it is likely that in the upcoming years further clinical trials will be conducted to evaluate the safety and efficacy of (more) Auger electron emitters in cancer therapy, potentially leading to their clinical approval.

## 1.2 Radiotheranostics for Triple-Negative Breast Cancer

Breast cancer is globally the most prevalent cancer in women. Additionally, there are 43,780 breast cancer-associated deaths annually, positioning it as the fifth highest cause of mortality on a global scale [25]. It predominantly affects Caucasian women, with age being a significant risk factor [26, 27]. Five years after diagnosis, 87 % of patients are still alive. However, breast cancers have the risk of local recurrences or metastases even after a longer period, necessitating long-term follow-ups, unlike many other cancer types [28]. Treatment options and prognosis vary depending on the cancer type and stage. The classification of different subtypes is primarily based on the receptor expression status, which serves as a target for personalized treatment approaches [29]. The main receptors in this context are the estrogen receptor, the progesterone receptor, and the human epidermal growth factor receptor 2 (HER2) [30].

## Introduction

Approximately 15 % of breast cancer cases do not express any of the three above mentioned receptors (i.e., estrogen receptor, progesterone receptor, or HER2), categorizing them as triple-negative breast cancer (TNBC) [30]. This highly aggressive subtype is associated with an earlier age of onset compared to other breast cancer types. Additionally, TNBC tumors are typically larger and at higher grade at the time of diagnosis than other subtypes. They often present with poorly differentiated histology and have a propensity for lymph node metastases, with a high likelihood of metastasizing to the lung and brain [31, 32]. The absence of the three receptors poses a challenge in directly targeting TNBC cells. The diversity of TNBC is demonstrated through its six molecular subtypes, comprising two basal-like, an immunomodulatory, a mesenchymal, a mesenchymal stem-like, and a luminal androgen receptor subtype [33]. Each subtype presents distinct characteristics such as modified biological pathways, genetic mutations, and varying cell compositions [33]. Current clinical interventions for TNBC involve cytotoxic chemotherapy, radiation therapy, and surgical procedures [30]. However, due to the non-specific nature of these treatments, their effectiveness is limited, resulting in a less favorable prognosis for TNBC patients [34, 35]. To enhance the long-term survival, increasingly more studies are focusing on understanding origin and progression of this disease via molecular and cellular analyses [30, 36, 37].

### 1.2.1 The BRCA Mutation – Biological Effects and Clinical Implications

Roughly 5 % - 10 % of breast cancer cases are inherited, with up to 25 % of them being linked to genetic mutations [38]. The most well-researched genes associated with hereditary breast cancer are Breast Cancer Gene 1 (BRCA1) and Breast Cancer Gene 2 (BRCA2). Mutations in these genes are strongly linked to Hereditary Breast/Ovarian Cancer Syndrome, which increases a woman's risk of developing breast and ovarian cancer [39, 40]. Women with BRCA1/2 mutations (BRCA<sup>mut</sup>) have a lifetime risk of 45 % to 75 % for breast cancer and 18 % to 40 % for ovarian cancer [41-43].

The BRCA1/2 genes function as tumor-suppressor genes and play essential roles in DNA damage repair and recombination, cell-cycle checkpoint control, apoptosis, and transcriptional regulation [44]. The primary mechanisms responsible for repairing DNA double-strand breaks (DSB) are homologous recombination (HR) [45] and non-

## Introduction

homologous end joining (NHEJ) [46]. HR predominantly operates during the S and G2 phases of the cell cycle and is a conservative process that aims to restore the original DNA sequence at the damaged site [47]. This process involves removing a portion of the DNA sequence surrounding the DSB (referred to as resection) and utilizing the DNA sequence on a homologous sister chromatid as a template for synthesizing new DNA at the DSB site. Key proteins involved in facilitating HR include those encoded by the BRCA1, BRCA2, RAD51, and PALB2 genes. In contrast, NHEJ is active throughout the cell cycle [47].

BRCA1 plays a multifaceted role in responding to DNA damage, participating in DNA repair and checkpoint activation. BRCA1 operates upstream of BRCA2 in the BRCA1/2-mediated HR pathway, while BRCA2 acts as a key player in the core process of HR. BRCA1 is involved in various steps of the DNA damage response, serving as a sensor, mediator, and effector of repair processes. It undergoes phosphorylation by checkpoint kinases like ATM, ATR, and CHK2, which regulate cell cycle checkpoints and aid in DNA damage repair [48].

Several studies have indicated that individuals with BRCA1<sup>mut</sup> are more likely to develop estrogen receptor-negative/progesterone receptor-negative breast cancer [49-51]. In contrast, those with BRCA2<sup>mut</sup> appear to exhibit pathological characteristics similar to individuals without BRCA mutations [52]. Furthermore, it is estimated that around 15 to 25 % of all patients with TNBC carry germline BRCA1/2<sup>mut</sup>, which are associated with a more aggressive disease phenotype [53].

Although existing data suggest that breast cancer patients with BRCA1<sup>mut</sup> are more likely to have TNBC, high nuclear grade, and larger tumor burden [54], Comen et al. (2011) discovered that the link between TNBC and BRCA<sup>mut</sup> is not exclusive to BRCA1, as a significant number of women with TNBC also have BRCA2<sup>mut</sup> [55]. The relationship between the presence of BRCA<sup>mut</sup> and the status of estrogen receptor, progesterone receptor, HER2/neu receptors, and P53 protein is, thus, not yet fully elucidated [56, 57].

### 1.2.2 Synthetic Lethality Induced by PARP Inhibitors in BRCA<sup>mut</sup> TNBC

In 2005, two groundbreaking studies revealed that tumor cells lacking the key tumor-suppressor proteins BRCA1 or BRCA2, are particularly sensitive to small molecule



## Introduction

inhibitors targeting the poly(ADP-ribose) polymerase (PARP) family of DNA repair enzymes [58, 59]. This discovery was rooted in the concept of synthetic lethality, where the loss of either BRCA1 or BRCA2 alone is not lethal, but simultaneous inactivation results in cell death. The primary target of PARP inhibitors (PARPi), PARP1, is mainly involved in repairing single-strand DNA breaks (SSBs). Inhibiting PARP1 alone is not fatal because other DNA repair pathways, such as HR, can repair the DNA lesions caused by these drugs. However, in the absence of BRCA1/2 and the resulting HR deficiency, the DNA lesions induced by PARPi remain unrepaired, leading to cell death [59, 60]. Cell lines deficient in BRCA1/2 exhibit sensitivity to PARPi, whereas cells with heterozygous loss of BRCA1/2 genes or those without BRCA1/2 abnormalities have not shown the same sensitivity [58].

PARPi were initially designed as drugs to enhance the sensitivity of cancer cells to radiotherapy and chemotherapy [61]. However, the two preclinical findings mentioned above provided a basis for developing PARPi as standalone treatments for cancers with BRCA1/2 mutations [59]. By 2005, the majority of the research on BRCA1/2 focused on their association as risk factors for hereditary breast and ovarian cancers. Consequently, individuals with germline BRCA1/2<sup>mut</sup> and cancer were the primary group targeted for clinical trials testing the synthetic lethal interaction between PARPi and BRCA<sup>mut</sup> [61, 62]. In 2018, the FDA granted approval for Lynparza (generic name olaparib, developed by AstraZeneca), and Talzenna (generic name Talazoparib, manufactured by Pfizer) to treat metastatic TNBC with germline BRCA<sup>mut</sup> (Figure 2A) [63, 64].

PARPi such as olaparib and Talazoparib are proven to exert their effects through two mechanisms of action [65]. Firstly, by inhibiting the catalytic activity of PARP, they impede the recruitment of DNA damage repair machinery, thereby disrupting the base excision repair process [59, 66]. This disruption leads to replication fork stalling during the S phase and the conversion of single-strand nicks into double-stranded breaks. Subsequently, the double-stranded breaks are typically repaired by proteins in the HR pathway. However, in the case of BRCA1/2<sup>mut</sup> cancers, which impair this pathway, the repair process is unsuccessful, ultimately triggering apoptosis (Figure 2B) [65]. The second mechanism involves the retention of PARP at the DNA damaged site, preventing its detachment from single or double-stranded breaks [67]. This retention necessitates the recruitment of HR pathway components, which, in BRCA1/2<sup>mut</sup> breast cancer tumors, are unable to perform the necessary repairs (Figure 2B) [65]. Interestingly, recent studies have suggested that

## Introduction

Talazoparib exhibits superior "trapping" capabilities compared to olaparib, despite both drugs having similar PARP inhibition activities [67]. However, further research is needed to fully elucidate these mechanisms [65, 68].

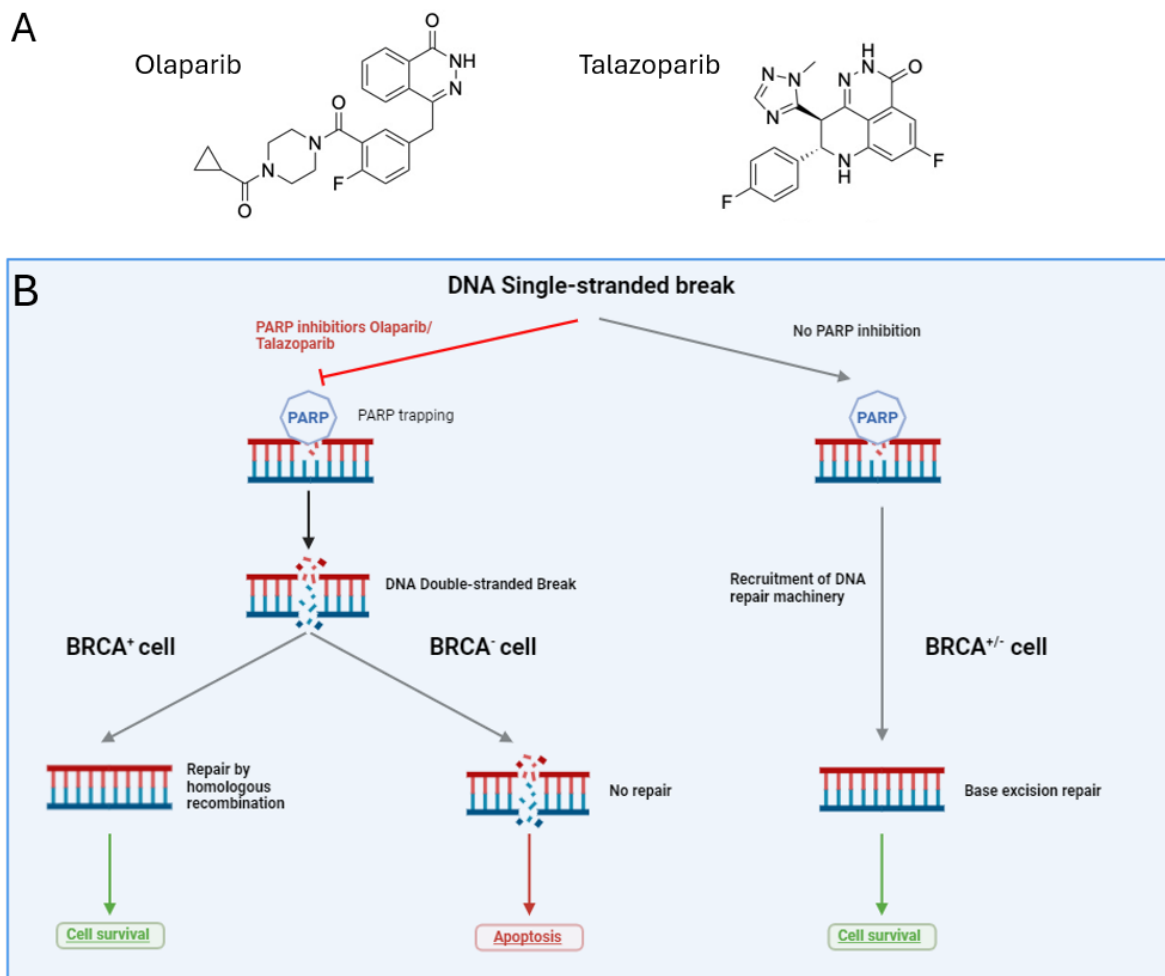


**Figure 2. PARP inhibitors in triple-negative breast cancer treatment. (A)** Chemical structures of FDA approved PARP inhibitors olaparib (left) and Talazoparib (right) for the treatment of TNBC. **(B)** The mechanism of action of PARP inhibitors involves the recognition and binding of PARP to single-stranded breaks in DNA, which then recruits the base excision repair machinery to fix the break. However, when PARP is inhibited, it becomes stuck at the site of the break, ultimately causing a double stranded break. Without the presence of BRCA1/2 and homologous repair mechanisms, this double stranded break is unable to be repaired, ultimately resulting in cell death.

### 1.2.3 Radiotheranostic PARP Inhibitors and Clinical Challenges

The discovery of PARP1 as a crucial target for the advancement of anti-cancer medications has propelled research on PARPi [69]. Given that the activity of PARP is

## Introduction

elevated as a result of the excessively active DNA damage repair pathway in different cancer cells, PARP has emerged as a novel target for cancer theranostics [60, 70].

PARP imaging agents have the potential to be valuable in various phases of cancer treatment. They can be used before treatment to predict therapy response and will allow patient stratification. Additionally, they can be utilized during and after treatment to assess tumor response to therapy. The demand for visualizing PARP1 expression throughout the body has initiated the creation and advancement of radiolabeled PARPi derivatives. These developments have enabled the non-invasive assessment of PARP1 expression using imaging techniques such as PET or SPECT.

When it comes to radiolabeling PARPi, radioactive halogen nuclides like  $^{18}\text{F}$ ,  $^{123}\text{I}$ , and  $^{131}\text{I}$  are preferred over radiometals such as  $^{68}\text{Ga}$  and  $^{99\text{m}}\text{Tc}$  due to their ease of radiolabeling without the requirement of a (chelating) ligand, as well as their favorable physical properties [71].

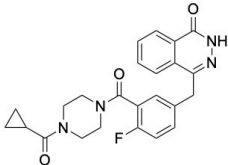
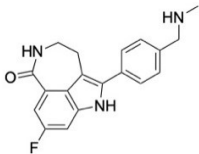
Puentes and colleagues conducted a review of the progress and assessment of ten relevant radiotracers targeting PARP-1 over the past five years [72]. These include [ $^{18}\text{F}$ ]PARPi, [ $^{18}\text{F}$ ]fluorothanatrax, and [ $^{18}\text{F}$ ]olaparib. Among these, only [ $^{18}\text{F}$ ]fluorothanatrax has been utilized in translational imaging studies across various tumor types such as breast cancer, hepatocellular carcinoma, and ovarian cancer (NCT03604315, NCT03083288, NCT03846167, NCT05226663, [73-75]).

In terms of radiotheranostics, therapeutic radionuclides, including  $\alpha$ ,  $\beta$ -, and Auger electron emitters, have been also incorporated into PARPi structures to effectively induce DNA damage in cancer cells by binding to PARP1, resulting in radioactive decay events in close proximity to the DNA. Significantly, these radionuclides also emit positrons or  $\gamma$ -rays, enabling the assessment of the tracer's behavior *in vivo* through PET/SPECT imaging. In the case of radiotheranostic PARP tracers, the therapeutic impact is not diminished by PARP inhibition; rather, the PARPi serves as a carrier for delivering the cytotoxic radiation [76], as radiopharmaceuticals are usually administered at concentrations within or below the picomolar range (mathematical derivation in chapter 0 for further details).

To date, however, no theranostic PARPi approach has made its way into clinical trials, but within the last five years, a considerable number of preclinical studies have been conducted using theranostic PARPi in various cancer types (Table 2).

## Introduction

**Table 2. Preclinical theranostic applications of radiolabeled PARP-ligands over the past five years.**

Parent	Tracer	Tumor entity	Year	Reference
<b>Olaparib</b> 	$[^{123}\text{I}]\text{I-MAPI}$	Glioblastoma	2020	[77]
	$[^{123}\text{I}]\text{I-MAPI}$	Colorectal cancer	2021	[78]
	$[^{123/125}\text{I}]\text{I-PARPi-01}$	TNBC	2022	[79, 80]
	$[^{123}\text{I}]\text{I-CC1}$	TNBC, Glioblastoma, Pancreatic cancer	2023	[81]
	$[^{77}\text{Br}]\text{Br-WC-DZ}$	Prostate cancer	2023	[82]
<b>Rucaparib</b> 	$[^{211}\text{At}]\text{At-MM4}$	Neuroblastoma	2019	[83, 84]
	$[^{123/125}\text{I}]\text{I-KX1}$	Ovarian cancer	2020	[85]
	$[^{123}\text{I}]\text{I-GD1}$	Different cancer entities	2023	[86]
	$[^{76/77}\text{Br}]\text{Br-RD1}$	Ovarian Cancer	2023	[87]

For TNBC, several attempts have been made to explore the potential of radio-labeled PARPi as a theranostic option. Two working groups in this field have focused on different olaparib analogues labeled with Auger electron emitters. Sankaranarayanan et al. [79, 80] and Chan et al. [81] utilized  $^{123}\text{I}$  labeling for their PARPi, with Chan et al. using this nuclide for both imaging and therapy, while Sankaranarayanan et al. utilized it solely for imaging purposes and exchanged the  $^{123}\text{I}$  with  $^{125}\text{I}$  for therapy applications.

Both studies highlight several limitations of PARPi radiotracers regarding their *in vivo* stability, biodistribution, and therapeutic efficacy [79, 81]. The reduced therapeutic effectiveness can be linked to deiodination processes, where the radioactive iodine atom is cleaved off from the tracer. This phenomenon is particularly evident from the significant accumulation of radioactivity in the thyroid, as reported by Sankaranarayanan et al [79]. The biodistribution of the radiotracer predominantly occurred in the liver, thyroid, and gastrointestinal tract, with minimal accumulation in the tumor (Figure 3A,B) [79, 81]. The lipophilic characteristics of the radiotracer facilitated rapid excretion via the hepatobiliary pathway, which hindered its ability to remain in circulation long enough to effectively accumulate in the tumor [79].

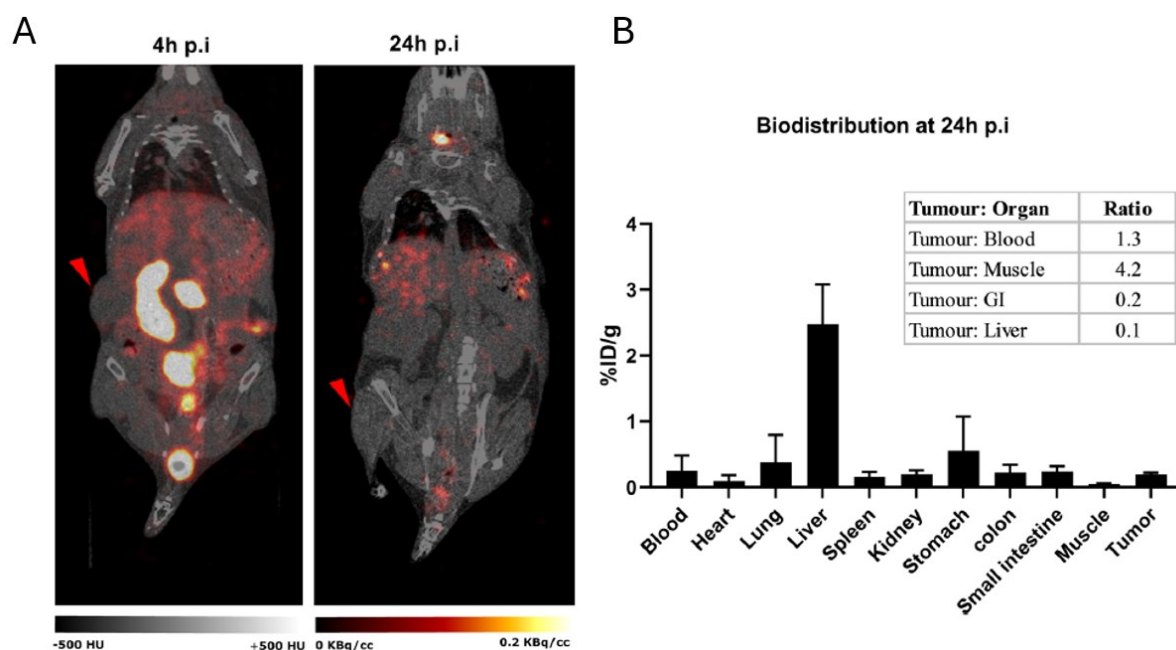


**Figure 3. Biodistribution results of  $[^{123}\text{I}]$ -PARPi-01 in NOD/SCID mice bearing- subcutaneous MDA-MB-231 xenograft. [79] (A)** Representative SPECT/CT images of *in vivo* biodistribution obtained at 4 h (left) and 24 h (right) post-injection (p.i). Red arrow shows tumor location. **(B)** *Ex vivo* biodistribution of  $[^{123}\text{I}]$ PARPi-01 at 24 h p.i.

One potential approach to address these challenges is the utilization of drug delivery systems designed to target TNBC biomarkers or altering the structure of PARPi tracers to decrease their lipophilicity, potentially reducing liver uptake. Similar to the advancements seen with laparib and talazoparib, the use of formulation strategies, including nanotechnology, holds promise to improve pharmacokinetics and pharmacological effectiveness of radiotheranostics [88, 89].

### 1.3 Radio-Nanomedicine: Nanocarriers for Radiotheranostics

Although radiotracer therapy provides various advantages over traditional radiotherapy and is generally well-tolerated, there are challenges associated with (the small size of) radiopharmaceuticals. These challenges include a short circulation time in the bloodstream, potential instability or degradation of the tracer, increased binding to plasma proteins, and the hepatobiliary clearance patterns of lipophilic tracers [79]. These factors can impede the therapeutic efficacy, particularly in instances where peptide or small molecule-based approaches such as radiolabeled PARPi are employed for therapy [90, 91].

## Introduction

Hence, several strategies have been explored over the recent years to enhance the therapeutic efficacy of radiotracers. A promising solution to tackle these challenges involves the application of nanotechnology. Nanomedicine has already shown to potentially modulate the biodistribution and improve the efficacy of therapeutics, enabling to overcome challenges associated with drug delivery. Nanoscale delivery systems (1-100(0) nm carrier materials) [92] have shown to optimize drug formulation by enhancing the water solubility of hydrophobic active pharmaceutical ingredients [93, 94] and by stabilizing compounds that are prone to degradation [95]. Nanocarriers (NCs) like polymeric nanoparticles, liposomes, mesoporous silica nanoparticles, dendrimers, and metal-based nanoparticles (Figure 4A) have been engineered to increase the dose reaching the target (cancerous) tissues while minimizing drug exposure to normal tissues [91]. At present, approximately 60 nanomedicines have received clinical approval for different indications [96]. Leveraging the nanoscale properties, drug delivery systems enable more selective and controlled delivery of radionuclides to the target (pathological) sites [91].

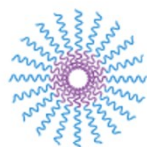
NCs can be customized in terms of different structural and physicochemical features, such as their dimensions, morphology, flexibility, and surface modification. Relevant examples include PEGylation, incorporation of the cluster of differentiation (CD) 47 proteins on their surface, or red blood cell hitchhiking [97, 98]. These strategies are designed to extend their circulation time in the bloodstream by modulating opsonization and minimizing early clearance by the spleen, liver, and bone marrow [99]. Additionally, these modifications help prevent aggregation and reduce nonspecific binding, thereby enhancing targeting to specific tissues [100].

NCs can also be functionalized with specific targeting molecules for active targeting, to facilitate specific tumor cell recognition and promote cellular uptake [97, 101, 102]. Similarly, with a wide array of commercially available bifunctional chelators (BFCs) featuring diverse functional groups, these BFCs can be attached to the surface of the nanoparticles for radiolabeling post-synthesis. In addition to the BFC method, alternative approaches for radiolabeling NCs include physically encapsulating the radioactive nuclide inside the carrier (Figure 4B) [91].

## Introduction

A

Polymeric Micelle



Liposome

Mesoporous  
Silica NP

Dendrimer



Metal NP



B

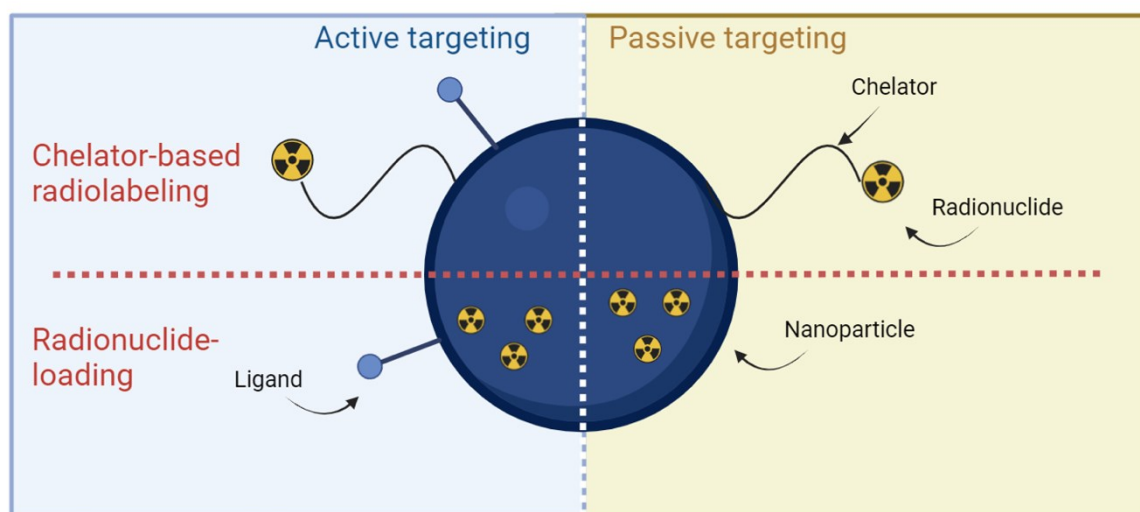


**Figure 4. Overview, functionalization and radiolabeling of different nanocarriers for radio theranostics. (A)** Examples of different classes of nanoparticles (NPs), including polymeric micelles, liposomes, mesoporous silica NPs, dendrimers and metal-based NPs (gold and silver mainly). **(B)** Radionuclides are attached to the the nanocarrier (NC) through a chelator (as shown in the upper panel), or they can be encapsulated within the NC (as illustrated in the bottom panel). Active targeting involves the attachment of specific ligands to the surface of the NC (depicted in the blue panel). In the case of passive targeting utilizing the EPR effect, no targeting ligands are attached to the surface (as indicated in the yellow panel).

Given their large surface-to-volume ratio, nanoparticles exhibit a high drug-loading capacity and can be tailored for controlled release of medications and radiation. Nanoparticles have the ability to preferentially accumulate in tumor tissues through leaky tumor blood vessels, and once they passively accumulate, they remain at the tumor site due to the abnormal, compromised lymphatic drainage of tumor tissues. This phenomenon is commonly referred to as the Enhanced Permeability and Retention (EPR) effect [101-103]. Incorporating targeting ligands onto the NCs' surface enables drug-loaded and/or radiolabeled NCs to be directed towards specific cells or subcellular locations, minimizing systemic exposure to cytotoxic drugs. However, it is important to note that the presence of targeting ligands or antibodies does not significantly alter the overall biodistribution of the nanoparticles. Instead, biodistribution primarily relies on passive targeting mechanisms, which direct NCs to tissues with leaky vasculature, such

## Introduction

as tumors. The targeting ligands primarily facilitate internalization of the NCs only after they have extravasated into the tumor microenvironment (TME) [104, 105].

The interaction between the ligands present on the surface of NCs (Figure 4B) and receptors expressed on tumor cells promote NC uptake through receptor-mediated endocytosis, enhancing their internalization within the tumor cells. [106]

The emerging field of radio-nanomedicine holds the potential to enhance the efficacy and safety of traditional endogenous radiotherapy, and it is progressively attracting attention beyond preclinical studies, also into clinical investigations.

### 1.3.1 Radioactive Nanomedicines for Cancer Theranostics

This chapter provides an overview of preclinical and clinical research studies involving radio theranostic NCs, specifically focusing on TNBC. These studies are centered on the development and assessment of different NC formulations for both imaging and therapeutic applications specifically tailored to address the challenges associated with TNBC. Most of these studies are summarized in Table 3.

This compilation of significant findings and results from various preclinical investigations, aims to highlight the promising potential of radio-labeled NCs as valuable assets in the diagnosis and treatment of TNBC. Various classes of NCs, including inorganic NCs (e.g., gold NCs [107, 108], copper NCs [109], and silica based NCs [110, 111]), and organic NCs (e.g., PLGA [112, 113], HPMA [114], and exosome mimetics [115]), have been successfully labeled with various radionuclides such as copper-64 ( $^{64}\text{Cu}$ ), gallium-68 ( $^{68}\text{Ga}$ ), lutetium-177 ( $^{177}\text{Lu}$ ), and zirconium-89 ( $^{89}\text{Zr}$ ). These innovations demonstrate significant applications for both imaging and therapeutic purposes in TNBC management.



## Introduction

Table 3. Overview of radiolabeled nanocarriers targeting triple-negative breast cancer.

Status	Nanocarrier	Radio-nuclide	Chelator	Active targeting ligand	Year	Reference
Preclinical	Gold	<sup>199</sup> Au	-	D-Ala1-peptide T-amide	2016	[107]
	Gold	<sup>64</sup> Cu	-	D-Ala1-peptide T-amide	2016	[108]
	Copper	<sup>64</sup> Cu	-	FC131	2019	[109]
	PLGA	<sup>177</sup> Lu	DOTA	Bombesin	2019	[112]
	Iron oxide	<sup>68</sup> Ga	DOTA	Bombesin	2019	[116]
	Iron oxide	<sup>68</sup> Ga	NODA-GA	Bombesin	2020	[117]
	Exosome-mimetics	<sup>131</sup> I	-	-	2022	[115]
	HPMA	<sup>89</sup> Zr	DFO	-	2022	[114]
	PLGA	<sup>131</sup> I	-	-	2023	[113]
	Silica	<sup>68</sup> Ga/ <sup>177</sup> Lu	DOTA	Folate	2023	[110]
Clinical	Silica	<sup>89</sup> Zr	bisphosphonate	-	2024	[111]
	Liposome	<sup>111</sup> In	-	-	1994	[118, 119]
	Colloid Albumin	<sup>99m</sup> Tc	-	-	2009	[120, 121]

HPMA = mPEG-b-pHPMAm, PLGA = poly(lactic-co-glycolic) acid.

While numerous radioactive NCs have advanced to preclinical stages, only a limited number have successfully progressed to the clinical or commercialization phase. Currently, clinically utilized NCs solely serve imaging purposes and fall into categories such as colloidal albumin, liposomes, and metal-based NCs (e.g., gold nanoparticles)[122]. Their applications in therapeutic contexts remain limited. Continued research and development are essential to expand the clinical utility of radio nanomedicine beyond imaging and into targeted therapeutic interventions.

Focusing on TNBC; in the 1980s and 1990s, a liposome formulation encapsulating <sup>111</sup>In known as Vescan was developed and clinically tested for detecting carcinoma and

## Introduction

metastases in prostate, lung, and breast cancer. Nevertheless, the program was discontinued due to the insufficient accuracy in detecting established tumors and the emergence of cheaper and improved alternative methods for tumor detection. One key discovery of this research was the detection of tumors persisting for a week post-administration, as evidenced by SPECT imaging in a patient with AIDS-related Kaposi's sarcoma, which evidenced the EPR effect in humans. Moreover, the extended retention period of the liposomal formulation underscored its increased stability. Based on these findings, the researchers envisaged radiolabeled liposomes as a valuable approach for forecasting therapy response and facilitating patient categorization [118, 119].

So far, however, the only NC still in clinical use is the  $^{99m}\text{Tc}$ -colloid  $^{99m}\text{Tc}$ -Nanocoll®, a nanosized colloid of albumin labelled with technetium-99m ( $^{99m}\text{Tc}$ ). This radioactive NC has received authorization for lymph node imaging in the European Union [120]. Additionally, a revised variant of the original  $^{99m}\text{Tc}$ -Nanocoll® utilizing sulfur in its colloidal form ( $^{99m}\text{Tc}$ -Technecoll®) has obtained approval in the USA for detecting nodes in melanoma, prostate, and breast cancer [121].

As previously mentioned, NCs have excellent properties for designing therapeutic nanomedicines, which can be also applied to radio theranostics: high surface-to-volume ratio, easy surface modification, EPR effect, improved bioavailability, and increased biological half-life [123].

However, it is essential to acknowledge the existing challenges in developing radioactive NCs for clinical use [124, 125]. These range from (a) establishing adequate synthetic and functionalization protocols to optimize their physicochemical properties such as size, shape, surface charge, and surface modifications with ligands, in order to significantly enhance targeting to specific tissues or organs [124, 126]; to (b) aspects related to large-scale manufacturing, such as the development of robust, up-scalable and reproducible production strategies which also enhance NC biodegradability for minimal environmental impact during body clearance [127]. Finally, the costs associated to the specific technical equipment required in hospitals for radioactive manipulation (both for therapy and diagnosis purposes) also adds complications to the clinical use of radio theranostic NCs [128].

### 1.3.2 Formulation of PARP Inhibitors in Polymeric Micelles

The selection of appropriate NCs and their core materials plays a crucial role in determining how drugs behave in the body and how effectively they can treat diseases [129]. In recent times, there has been a growing emphasis on using nanotechnology to deliver PARPi for cancer treatment. Among the notable delivery vehicles that have been investigated are liposomes [130, 131], polymeric micelles (Table 4), and hybrid nanosystems [132, 133].

Given the increasing focus on nanotechnology for the delivery of PARPi in cancer therapy, it is essential to highlight the specific types of NCs that have shown significant promise. Among these, polymeric micelles stand out as one of the most extensively explored nanoparticles for anticancer drug delivery. Numerous preclinical and a number of clinical studies have demonstrated the promise of polymeric micelle-based formulations in cancer treatment [134-136], as illustrated by the clinically approved paclitaxel micellar formulation, Genexol-PM.

Polymeric micelles consist of amphiphilic block copolymers self-assembled into nanosized structures, featuring a hydrophilic outer shell and a hydrophobic inner core, which is suitable to encapsulate poorly water-soluble compounds [94, 137]. These NCs are well-suited for delivering poorly water-soluble compounds [137], including chemotherapeutic agents like PARPi (Table 4).

Polymeric micelles can be constituted of polymers that are biocompatible, and thus safe for systemic administration in humans. Polymeric micelles have shown to encapsulate a wide range of hydrophobic drugs, enabling to extend circulation times and improve tumor accumulation of therapeutics [138-140].

In contrast to other drug delivery systems such as liposomes and lipid nanoparticles, polymeric micelles exhibit enhanced loading and retention of hydrophobic drugs, all within sizes that can be tuned, typically, in the range between 30-100 nm [94]. Additionally, they have increasingly shown promise as modular platforms for multidrug delivery, thus holding potential in drug combination therapies [141].

In the context of TNBC and PARPi, Sargazi et al provide a comprehensive overview of different formulations incorporating PARPi in NCs for different cancer applications [129]. Among nine studies involving PARPi encapsulated in polymeric micelles, two specifically

## Introduction

focused on targeting TNBC. For instance, a polymeric micelle formulation of Talazoparib (NanoTalazoparib) was to significantly increase the survival of BRCA<sup>mut</sup> mice following the iv administration, leading to a 50 % reduction in tumor volume while being well-tolerated [142].

**Table 4. Polymeric nanoformulations of PARP inhibitors.**

<b>Polymer</b>	<b>PARPi</b>	<b>Co-loading/treatment</b>	<b>Cancer entity</b>	<b>Year</b>	<b>Reference</b>
<b>PLGA</b>	Talazoparib	-	Breast Cancer	2017	[143]
<b>MPEG-PCL</b>	Olaparib	Radiotherapy	Human non-small-cell lung cancer	2018	[89]
<b>PCEC</b>	Talazoparib	-	TNBC	2018	[142]
<b>PCEC</b>	Olaparib	Radiotherapy	Cervical carcinoma	2020	[144]
<b>Pluronic F127</b>	Olaparib	Etoposide	Glioblastoma	2020	[145]
<b>poly(2-oxazoline)</b>	Niraparib	HS-173 Radiotherapy	Colorectal cancer	2020	[146]
<b>PLGA</b>	Veliparib	Methylene blue	Murine melanoma	2021	[147]
<b>PLGA</b>	Olaparib	Paclitaxel FOX M1	TNBC	2021	[148]
<b>MPEG-PCL</b>	Olaparib	-	Cervical carcinoma	2024	[149]

**PLGA** = poly(lactic-co-glycolic) acid, **PCEC** = Poly(ε-caprolactone)-poly(ethylene glycol)-poly(ε-caprolactone), **MPEG-PCL** = Methoxy Poly(ethylene glycol)-poly(ε-caprolactone).

In another example, PLGA NCs coated with chitosan and small interfering RNA targeting Forkhead Box M1 (FOX M1-siRNA) were engineered and loaded with the PARPi Olaparib for TNBC [148]. These nanoparticles were effectively internalized by TNBC cells *in vitro* and exhibited cytotoxic effects. Overall, the PARPi-loaded polymeric NCs showed promise in

## Introduction

inhibiting cancer cell proliferation. Encapsulating PARPi in NCs enables the delivery of these poorly water-soluble drugs while providing a sustained release profile that extends their circulation time in the bloodstream [129, 150]. As a result, NCs exhibit significantly improved pharmacokinetics compared to small molecule PARPi drugs. The high hydrophobicity of PARPi poses challenges for systemic administration in patients, necessitating oral delivery [151]. However, this route can result in significant degradation of the drug in the liver, which ultimately reduces its effective concentration by the time it reaches the target site [129].

Additionally, NCs promote enhanced drug accumulation in tumor tissues, often through passive targeting mechanisms such as the EPR effect [113, 140, 142], while minimizing off-target accumulation and, therefore, reducing side-effects. They also have the potential to circumvent drug resistance mechanisms by enhancing the cellular uptake of PARPi within cancer cells, offering the possibility of reversing resistance to these agents [152]. Finally, NCs can facilitate the co-delivery of different therapeutic agents, allowing for (synergistic) combination therapy approaches that enhance therapeutic outcomes [141, 153]. In this regard, synergistic effects of PARPi with other drugs, such as chemotherapy or immunotherapy agents have been already explored (Table 4 co-loading/treatment).

Overall, encapsulating PARPi in NCs represents a promising strategy to optimize their therapeutic potential, improve their pharmacokinetics and biodistribution, and enhance their overall effectiveness in cancer treatment.

### 1.3.3 $\pi$ electron-stabilized PEGylated HPMA-Based Micelles

While existing drug-loaded polymeric micelle formulations notably enhance drug solubility and reduce its toxicity, their therapeutic efficacy is often on par with the free drug. In some cases, it has been shown that PTX encapsulated in MePEG-b-PCL polymeric micelles [154] or PLGA polymeric micelles [155] exhibits analogous pharmacokinetics to the free drug, primarily due to fast micelle destabilization post-iv injection [156, 157] and premature release of the drug from the micelles [154, 155]. Several strategies have been explored over the years to increase the colloidal stability of polymeric micelle formulations, consequently enhancing the retention of their cargoes.

## Introduction

One of the most common approaches is the use of chemical cross-linking, which chemically conjugates the polymer chains, and can prevent the dissociation of polymeric micelles [158]. However, this approach may not enhance drug retention within the micelles. While chemical conjugation of drug molecules to polymers has demonstrated to improve drug retention, these approaches are often technically complex and may impact the pharmacological effects of the drugs as well as the eventual large-scale manufacturing and pharmaceutical development [127, 159].

A recent strategy to increase colloidal stability of and drug retention in polymeric micelles without employing chemical conjugation involves the use of aromatic substitutes in the core of PEGylated HPMA-based polymeric micelles. The presence of benzoyl groups in the repeating units of the block copolymer mPEG-*b*-p(HPMAm-Bz) (i.e., methoxy poly(ethylene glycol)-*b*-(*N*-(2-benzoyloxypropyl) methacrylamide)) resulted in the formation of micelles with significantly improved stability and enhanced retention of drugs like paclitaxel [140]. These beneficial characteristics are ascribed to non-covalent  $\pi$ - $\pi$  stacking and hydrophobic interactions, eliminating the previous necessity for employing chemical cross-linking and covalent drug conjugation to stabilize micelles and enhance drug retention [160].

These  $\pi$  electron-stabilized PTX-loaded polymeric micelles displayed prolonged circulation kinetics and improved tumor accumulation as compared to Taxol (clinically relevant formulation of paclitaxel), and they induced complete tumor regression in two different xenograft models without causing significant side effects [140].

In addition, these micelles have been successfully radiolabeled with  $^{89}\text{Zr}$ , paving the way for potential theranostic and image-guided therapy applications [114].

## 1.4 Motivation and Goals

Our working group previously established a targeted radiotherapeutic approach against BRCA<sup>mut</sup> TNBC, combining PARPi with  $^{125}\text{I}$  radiotherapy, and developing a  $^{123/125}\text{I}$ -PARPi-01 tracer. Preclinical evaluation of the radiolabeled tracer showed poor biodistribution and instability *in vivo*, thus limiting their therapeutic potential [79].

Radio-nanomedicine, the combination of nuclear medicine and nanotechnology, is an emerging strategy in nuclear imaging and therapy. Nanoformulations can increase the

## Introduction

stability of radiopharmaceutical agents, protect them from rapid hepatic degradation, and prolong blood circulation time, together enhancing therapeutic efficacy. Hence, in this PhD thesis work, the main aim was to develop a polymeric micelle-based theranostic formulation co-encapsulating radioactive and SPECT-imageable  $^{123/125}\text{I}$ -PARPi-01 with non-radioactive I-PARPi-01, in order to enhance tracer stability, biodistribution, and target-site accumulation for improved radio-chemotherapy combination (Figure 5).

To achieve the overall aim, I defined several objectives, which are aligned with the different chapters of this thesis:

- 1. Formulation of  $^{123/125}\text{I}$ -PARPi-01 and I-PARPi-01 co-loaded  $\pi$  electron-stabilized polymeric micelles**, and assess their stability and pharmaceutical properties while ensuring effective drug loading and retention.
- 2. Test the *in vitro* performance** of the co-loaded micelles in different TNBC cell lines, focusing on drug uptake from the micelles, protection of the radiotracer from enzymatic degradation, and assessment of cytotoxicity.
- 3. Study the *in vivo* biodistribution and therapeutic effect** of the Auger electron-emitting PARPi co-loaded micelle formulations in BRCA<sup>mut</sup> TNBC-bearing mouse models focusing on enhancing *in vivo* radiotracer blood circulation time and tumor accumulation, followed by an assessment of their therapeutic performance.
- 4. Assess *ex vivo*** the mechanisms of action and effects of the therapeutic micelle formulations.

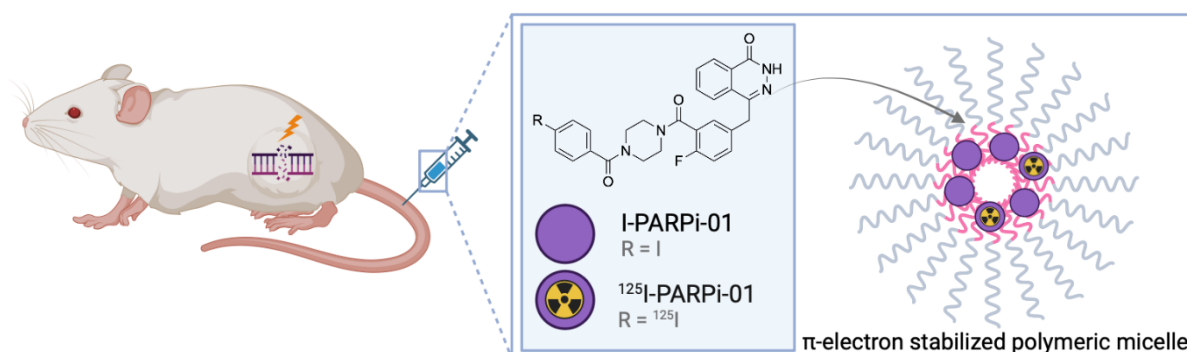


**Figure 5. Overview of this PhD thesis work: Auger electron-emitting nanotheranostics for image-guided radio-chemotherapy against triple-negative breast cancer.** Radioactive and non-radioactive PARPi within  $\pi$  electron-stabilized polymeric micelles, which are then administered to BRCA<sup>mut</sup> TNBC xenografts bearing mice, resulting in the induction of DNA double-strand breaks.

## 2 Materials and Methods

### 2.1 Equipment and Chemicals

#### 2.1.1 Chemicals, Kits and Consumables

Chemical	Company
[ <sup>123</sup> I]-Iodide in 0.1M sodium hydroxide	ROTOP
[ <sup>125</sup> I]-Iodide in 0.1M sodium hydroxide	Scantor GmbH
[ <sup>131</sup> I]-Iodide in 0.1M sodium hydroxide	GE Healthcare
5 mL glass vials	CS (Chromatographie Service GmbH)
Acetic acid	Roth
Acetone	VWR Chemicals
Acetonitrile	VWR Chemicals
Antifade Mounting Medium with DAPI	Vectashield
Any kDTM Mini-PROTEAN®TGXTM Precast Protein Gel	BIO-Rad
Argon gas	Linde
Bovine serum albumin (Fraction V)	Sigma-Aldrich
Cell culture flask, different sizes	Sarstedt
Centrifugal concentrator columns, Vivaspin 2, Membrane: 10000 MWCO, PES	Sartorius
Chloramin T	Merck-Schuchardt
Cholera toxin	Sigma-Aldrich
CO <sub>2</sub> gas	Linde
Cover slips	Marienfeld
Cremophor EL	EMD Millipore
Cy7- mPEG- <i>b</i> -p(HPMAm-Bz)	Institute for Experimental Molecular Imaging, Working Group of Prof. Twan Lammers



## Materials and Methods

CyQUANT™ XTT Cell Viability Assay	Invitrogen
Dichloromethane	Sigma-Aldrich
Dimethyl sulfoxide	Roth
Disposable polystyrene cuvettes	Sarstedt
DMEM/F12	Thermo Fisher Scientific
DMEM/F12 Cell medium	PAN-Biotech
Dulbecco's Modified Eagle's Medium (DMEM)	PAN-Biotech
Dulbecco's Phosphate Buffered Saline	PAN-Biotech
Endothelial growth factor	PAN-Biotech
Eosin	Roth
Eppendorf tubes, different sizes	Sarstedt
Ethanol	Sigma-Aldrich
Falcon Tubes, different sizes	Sarstedt
Fetal bovine serum	PAN-Biotech
Float-A-Lyzer dialysis devices (MWCO of 300 kDa)	Spectrum Labs
Formaldehyde	Carl ROTH
Glass pipettes	Brand
Hematoxylin	Roth
Horse serum	Gibco
HPLC water ultrapure	AppliChem
Hydrocortisone	Stemcell technologies
Insulin	Lonza
I-PARPi-01	Institute of Organic Chemistry, RWTH Aachen University, Working Group of Prof. Carsten Bolm
Isoflurane	Sedana medical
Matrigel	Corning
MAURA Developer	Tetenal
MAURA Fixing solution	Tetenal

## Materials and Methods

MAURA NTB solution	Kodak
Microscope slides	Knittel glass
Microscopy slides	Star Frost
Milk powder	Applichem
Milli-Q Water	Institute for Experimental Molecular Imaging, RWTH Aachen University
Mowiol®	Sigma-Aldrich
mPEG-b-p(HPMAM-Bz)	Institute for Experimental Molecular Imaging, RWTH Aachen University, Working Group of Prof. Twan Lammers
Neubauer chamber	Marienfeld
Nylon syringe filter, 0.2 µm	Whatman
PAP pen	Science Services
PARPi-01 tributyltin precursor	Institute of Organic Chemistry, RWTH Aachen University, Working Group of Prof. Carsten Bolm
Penicillin	PAN-Biotech
Pierce BCA Protein Assay Kit	Thermo Fisher Scientific
Pierce™ ECL Western Blotting Substrate	Thermo Fisher Scientific
Pipette tips 1000 µL, 200 µL, 10 µL	Sarstedt
Pipettes, 1000 µL, 200 µL, 10 µL	VWR
polyvinylidene fluoride membrane	BIO-RAD
PTFE syringe filter, 0.2 µm	Pall Corporations
Ricinus Communis Agglutinin I (RCA I, RCA120), Rhodamine (RL-1082-1)	Vector Laboratories
RIPA buffer	Sigma-Aldrich
Roswell Park Memorial Institute medium	PAN-Biotech
Roti® Mount FluorCare DAPI (DAPI)	Roth
Roti®Histofix	Roth
Sep-Pak light C18 cartridge (WAT023501)	Waters
Serological pipettes, different sizes	Sarstedt

## Materials and Methods

Sodium chloride	VWR
Sodium citrate	FLUKA Analytical
Streptomycin	PAN-Biotech
Sucrose	Roth
Syringes, different volumes	B. Braun
Tetrahydrofuran (THF)	Carl ROTH
Tissue-Tek	Sakura
Trifluoric acid	Sigma-Aldrich
TRIS	Roth
Triton X 100	Sigma-Aldrich
Trypan blue	Sigma-Aldrich
Trypsin-EDTA in PBS w/o Ca and Mg	PAN-Biotech
Tween® 20	Sigma-Aldrich
Well plates, different sizes	Starlab
Xylol	VWR

## 2.1.2 Buffers

Buffer	Components
Citrate buffer, pH 6.0	10 mM sodium citrate 0.05 % Tween® 20 in distilled water
TBST buffer, pH 7.5	0.1 % Triton X 100 150 mM sodium chloride 20 mM TRIS

## 2.1.3 Cell Lines

All cell lines (HCC1937, MCF10A, MDA-MB-231, MDA-MB-468) used in this work were purchased from ATCC (Virginia, USA).

## Materials and Methods

## 2.1.4 Antibodies

Target	Host	Company
$\gamma$ -H2A.X	Rat	Biolegend
Anti-mouse IgG HRP	Horse	Cell signalling
Anti-rabbit IgG AF488	Goat	Cell signalling
Anti-rabbit IgG HRP	Goat	Cell signalling
GAPDH	Rabbit	Cell signalling
IgG-Cy5	Goat	Dianova
Mouse F4/80	Rabbit	Abcam
PARP1	Mouse	Sigma-Aldrich

## 2.1.5 Devices

Device	Model	Company
Aktivimeter	Isomed	Isomed
Bright light Microscope	Zen Lite	Carl Zeiss AG
Cell incubator	HERACell 240i	Thermo Scientific
Centrifuge, Eppendorf tubes	Heraeus Fresco21	Thermo Fisher Scientific
Centrifuge, falcon tubes	Rotana 460R	Hettich
Fluorescence microscope for <i>in vitro</i> experiments	LEO 906E & Zen 3.0 Blue edition	Zeiss
Gamma counter	Wizard2	PerkinElmer
Gel electrophoresis cell	Mini-PROTEAN® Tetra System	BIO-RAD
High-performance liquid chromatography (HPLC)	S2100	Sykam

## Materials and Methods

High-performance liquid chromatography column	Chromolith® FastGradient RP-18 endcapped 50-3, poresize 2 µm	Chromolith
HPLC radio detector	GabiStar	Raytest Isotopengeräte
HPLC UV detector	-	Chromolith
Luminescent Analyzer	Image Quant LAS 4000	GE Healthcare
Microscope for <i>ex vivo</i> histology: AxioImager M2 microscopy system	AxioCamMRm Rev.3 camera	Carl Zeiss AG
pH meter	pH-Meter 765 Calimatic	Knick
Pipetboy	Pipetboy2	Integra
Plate reader	Infinite M Plex	Tecan
Portable radiation detector	-	Berthold
Sterile bench	Safe2020	Thermo Scientific
Stirring plate	RCT basic	IKA
Ultrasonication bath	SonoRex RK100H	Bandelin
Vacuum pump system, Cell culture	-	VHC (pro)
Vortexer	Vortex-Genie2	Scientific Industries
Western blot power supply	Power-Pac™ HC	BIO-RAD
Zetasizer dynamic light scattering	-	Malvern Panalytical

## 2.1.6 Softwares

Software	Version	Company
GraphPad Prism	10.2.2(397)	Dotmatics
GinaStar	5.9	Raytest Isotopengeräte
Zen	Blue Edition 2012	Carl Zeiss Microscopy GmbH

## Materials and Methods

ZEN 2012 SP2 x86	1.1.001	Carl Zeiss Microscopy
Microsoft Office	2016	Microsoft
Biorender	2024	Biorender
Zetasizer	7.13	Malvern Panalytical
PMOD software	4.4	PMOD technologies, Switzerland
Isomed	2010	Isomed

## 2.2 Methods

### 2.2.1 Statistical Analysis

Statistical analysis was done using GraphPad prism 10.2.2(397) software. Data are expressed as mean  $\pm$  standard deviation ( $n = 3$ ; unless stated otherwise). One-way or two-way analysis of variance (ANOVA) with multiple-group comparisons, or unpaired t-test (based on software recommendations) was applied, depending on each specific set of data. 0.05 was used as alpha threshold for determining statistical significances, which were considered for  $p$ -values  $< 0.05$  (\*),  $p < 0.01$  (\*\*),  $p < 0.001$  (\*\*\*) and  $p < 0.0001$  (\*\*\*\*).

### 2.2.2 High-Performance Liquid Chromatography (HPLC)

Analytical reversed-phase HPLC was performed using an Knauer HPLC system equipped with a quaternary pump and UV- vis- and radio detector. For all HPLC measurements, a gradient elution method (Solvent A: H<sub>2</sub>O/Trifluoroacetic acid (TFA) (99.9/0.1% v/v); and Solvent B: Acetonitrile (ACN)) at a flow rate of 1 mL/min and a HPLC affinity C18 column (50  $\times$  3 mm, particle size 2  $\mu$ m) were used. The detection wavelength was 254 nm.

### 2.2.3 Radiolabeling of PARPi-01

The radionuclide <sup>125</sup>I was purchased from Scantor GmbH (Cologne, Germany). The delivered [<sup>125</sup>I]-Iodide in 0.1M sodium hydroxide was concentrated by evaporation and redissolution

## Materials and Methods

in the needed volume but did not exceed a concentration of 0.5M sodium hydroxide. Moreover, 5  $\mu$ L of a PARPi-01 tributyltin precursor solution (15mM in dichloromethane) was evaporated in a microcentrifuge tube by Argon gas stream and redissolved in 20  $\mu$ L of acetic acid. The identity of the PARPi-01 tributyltin precursor was 4-([4-fluoro-3-((4-[4-(tributylstannyl)benzoyl]-1-piperazinyl)carbonyl)phenyl]methyl)-1(2H)-phthalazinone.

Moreover, 10  $\mu$ L of the concentrated radioiodide solution was added to the tube, and labelling was started by adding 20  $\mu$ L of a fresh chloramine-T solution (1.0 mM in ACN). The reaction was maintained for 10 min at RT (24 °C) and the crude reaction mixture was purified using by HPLC (see chapter 2.2.1).

The product fraction (5–7 min, 2 mL) was diluted with 10 mL of water and was solid phase extracted by a preconditioned Sep-Pak light C18 cartridge (WAT023501). The [ $^{125}$ I]-PARPi-01 was eluted using 1 mL of ethanol (EtOH) or THF and evaporated to dryness at 85 °C under Argon gas stream. The residue was taken up in 60  $\mu$ L of EtOH or THF.

## 2.2.4 Micelle Synthesis and Characterization

### 2.2.4.1 Micelle Synthesis and Drug Loading

Polymeric micelles were formulated using block copolymers based on poly(ethylene glycol) and benzoylated poly(methacrylamide) derivatives, i.e., mPEG-*b*-p(HPMAm-Bz), provided by the working group of Prof. Lammers (Institute for Experimental and Molecular Imaging, University Hospital RWTH Aachen) [161, 162].

For the fluorescently labeled micelles, the polymer was additionally modified with the near-infrared dye Cy7 through covalent binding [140]. Consequently, the fluorescent polymer was blended with the non-fluorescent polymer in various proportions (100%, 2%, or 1% Cy7-labeled polymer).

In summary, 10, 20, or 30 mg of the polymer, along with varying quantities of I-PARPi-01 and/or [ $^{123/125/131}$ I]-PARPi-01, were dissolved in 1 mL of tetrahydrofuran (THF). If necessary, the solution was ultrasonicated to ensure complete dissolution. This solution was then added dropwise to 1 mL of Milli-Q water while stirring at room temperature (RT). To protect the mixture from dust, it was covered with aluminum foil, which had been punctured to allow for ventilation. The mixture was allowed to sit at RT for a minimum of 24h to facilitate the evaporation of THF. The final formulation was then adjusted to a total volume of 1 mL

## Materials and Methods

with Milli-Q water, filtered through nylon membranes (pore size: 0.2  $\mu\text{m}$ ), and stored at 4°C before undergoing *in vitro* and *in vivo* assessments. A graphical representation of the synthesis process can be found in Figure 6.

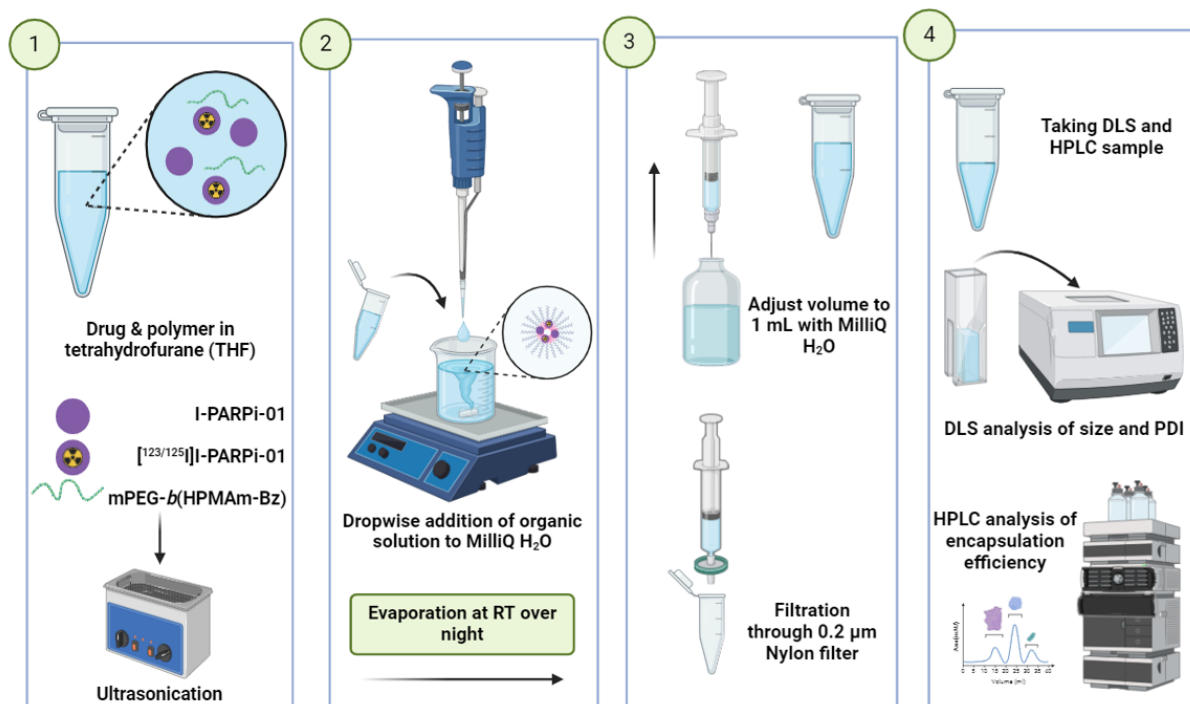


**Figure 6. Micelle synthesis procedure.** (1) Polymer and drugs were dissolved in 1 mL of tetrahydrofuran (THF) and ultrasonicated if needed. (2) *In situ* micelle formation and drug loading was performed by using the nanoprecipitation method. The THF-drug-polymer solution was therefore added dropwise to Milli-Q water. The mixture was kept at RT for at least 24h to evaporate THF. (3) The resulting formulation was adjusted to 1 mL of final volume with Milli-Q water and filtered with nylon membranes (pore size: 0.2  $\mu\text{m}$ ) and stored at 4°C. (4) Drug-loaded micelles were further analyzed by HPLC (encapsulation efficiency, loading capacity) and DLS measurements (size, PDI).

### 2.2.4.2 Determination of Size and Polydispersity Index of Polymeric Micelles

The hydrodynamic diameter (size) and polydispersity index (PDI) of the micelles were measured by dynamic light scattering (DLS) (Nano-S, Malvern Panalytical PLC), using disposable polystyrene cuvettes. The samples were diluted to 1:100 using Milli-Q water before measurement. Samples were measured at a fixed scattering angle of 173° and a temperature of 25 °C. The attenuator was automatically chosen for measurements.

### 2.2.4.3 Determination of Encapsulation Efficiency (EE) and Loading Capacity (LC) of Polymeric Micelles

Drug concentration in polymeric micelles was determined by HPLC. The EE and LC were calculated using equations (1) and (2), respectively:



$$EE [\%] = \frac{\text{Detected amount of drug}}{\text{Feed amount of drug}} \times 100 \quad (1)$$

$$LC = \frac{\text{Detected amount of drug}}{\text{Detected amount of drug} + \text{feed amount of polymer}} \times 100 \quad (2)$$

#### 2.2.4.4 Transmission Electron Microscopy (TEM) of Polymeric Micelles

For TEM analysis, micellar dispersions of different concentrations were diluted 1:100 with Milli-Q water. The samples were then analyzed by the Electron Microscopy Facility, Institute of Pathology of RWTH Aachen University Hospital. Samples were left to adsorb on glow discharged Formvar-carbon- coated nickel grids (Maxtaform, 200 mesh) for 10 min. Negative staining was performed with 0.5% uranyl acetate (Science Services GmbH). TEM images were recorded on a HT7800 TEM (Hitachi, Japan), operating at an acceleration voltage of 60 kV.

#### 2.2.4.5 Drug Release

Drug release of different drug-loaded micelles was evaluated under sink conditions in Dulbecco's Phosphate Buffered Saline (PBS) (pH 7.4) containing 45 mg/mL bovine serum albumin (BSA) [163]. In brief, Float-A-Lyzer dialysis devices (MWCO of 300 kDa) were filled with 1 mL of drug-loaded micelles and submerged in the medium at 37 °C under shaking agitation. At different time points, samples of 50 µL were withdrawn from the dialysis device, diluted 10 times in ACN, centrifuged at 5000 g for 10 min to remove the precipitated BSA, and the drug content in the supernatant was determined via HPLC. The withdrawn volumes were compensated with equal volumes of BSA in PBS solution.

## Materials and Methods

### 2.2.5 *In Vitro* Experiments

#### 2.2.5.1 *Cell Culture Conditions*

MDA-MB-231 and MDA-MB-468 were cultured in Dulbecco's Modified Eagle's Medium (DMEM) supplemented with 10% fetal bovine serum (FBS) and 1% penicillin-streptomycin. MCF-10A cells were cultured in DMEM/F12 supplemented with 5% horse serum, 20 ng/mL endothelial growth factor (EGF), 0.5 µg/mL hydrocortisone, 100 ng/mL cholera toxin, 10 µg/mL insulin, 1% penicillin-streptomycin. HCC1937 were cultured in Roswell Park Memorial Institute media (RPMI) (Pan Biotech, Germany) supplemented with 10% FBS and 1% penicillin-streptomycin. The cells were subcultured twice a week. All cells were maintained at 37 °C and 5% CO<sub>2</sub>. All cells were tested biweekly for mycoplasma contamination.

#### 2.2.5.2 *Western Blot Analysis*

Crude cell lysates were prepared from cells using 100 µL RIPA buffer. Protein concentrations were determined using the Pierce BCA Protein Assay Kit. A total of 30 µg of protein was loaded in each well on an Any KDTM Mini-PROTEAN®TGXTM Precast Protein Gel and blotted onto a polyvinylidene fluoride membrane. Unspecific signal was blocked with 5% milk powder in TBST for 1h at RT. The membranes were incubated overnight shaking at 4 °C with primary antibodies: mouse α-PARP1 (1:1000) or rabbit α-GAPDH (1:2000). After washing, the secondary antibody horse α-mouse IgG HRP (1:1000) or goat α-rabbit IgG HRP (1:1000) was applied for 1h at RT. The membrane was prepared for signal detection with Pierce™ ECL Western Blotting Substrate and subsequently analyzed with an Image Quant LAS 4000 Luminescent Analyzer.

#### 2.2.5.3 *Cell Uptake*

Cells ( $5 \times 10^5$  cells/well) were seeded in triplicates in 12-well plates 24h prior to incubation with 0.1 MBq/well naked [<sup>131</sup>I]-PARPi-01 or [<sup>131</sup>I]-PARPi-01 single-loaded micelles. Tracer-loaded micelles were prepared with 30 mg/mL polymer.

After 1h cells were washed and detached with trypsin. Cell-associated radioactivity was measured with a Wizard2 gamma counter.

## Materials and Methods

### 2.2.5.4 Radiotracer Stability

To determine the tracer stability in different media, 2 MBq of naked [ $^{131}\text{I}$ ]I-PARPi-01 or [ $^{131}\text{I}$ ]I-PARPi-01 single-loaded micelles (prepared with 30 mg/mL polymer) were mixed with (a) PBS (pH 7.4) or (b) human serum (c radiotracer/tracer-loaded micelles = 2 MBq/mL, 37°C, gentle shaking).

For the tracer stability in metabolically active environment HCC1937 cells ( $5 \times 10^5$  cells/well) were seeded in triplicates in 12-well plates 24h prior to incubation with naked [ $^{131}\text{I}$ ]I-PARPi-01 or [ $^{131}\text{I}$ ]I-PARPi-01 single-loaded micelles (c radiotracer/tracer-loaded micelles = 2 MBq/mL, 37°C, gentle shaking). To inhibit enzymatic degradation of the radiotracer by the HCC1937 cells, samples have been incubated with the cells additionally at 4 °C under gentle shaking.

Samples were taken after 0, 1, 4, 24, 48 and 72h incubation time of the mixture/supernatant and the amount of intact [ $^{131}\text{I}$ ]I-PARPi-01 was analyzed via radio-HPLC. Experiments were carried out in triplicates,  $n = 3$ .

### 2.2.5.5 Cytotoxicity of I-PARPi-01

Cells ( $5 \times 10^3$  cells/well) were seeded in triplicates ( $n=3$ ) in 96-well plates 24h prior to incubation with I-PARPi-01. To minimize evaporation effects on absorbance detection, the outer ring of the well plate was left empty. Serial dilutions of I-PARPi-01 (200  $\mu\text{M} \rightarrow 0$   $\mu\text{M}$ ) were dissolved in DMSO (final concentration of 1% DMSO/well), mixed with fresh medium and incubated with the cells. Control samples contained 0  $\mu\text{M}$  I-PARPi-01 consisting of medium including 1% DMSO. Cells were incubated under standard conditions for 72h.

After incubation time the cells were washed with PBS and incubated with 100  $\mu\text{L}$  medium and 70  $\mu\text{L}$  of XTT reagent protected from light, under standard conditions for 2h. Blank samples contained only 100  $\mu\text{L}$  medium and 70  $\mu\text{L}$  of XTT reagent without cells. The absorbance values of each well were measured at 450 nm and 660 nm in the Tecan plate reader. Based on the absorbance value, the cell viability of each well has been calculated.

## Materials and Methods

### 2.2.5.6 Cytotoxicity of I-PARPi-01 and [<sup>125</sup>I]I-PARPi-01 Co-Loaded Micelles

HCC1937 and MDA-MB-468 cells were seeded in triplicates (n=3) in 12-well plates 24h prior to incubation with either a mixture of naked I-PARPi-01 and [<sup>125</sup>I]I-PARPi-01 or micelles co-loaded with I-PARPi-01 and [<sup>125</sup>I]I-PARPi-01 (30 mg/mL polymer).

The corresponding IC<sub>50</sub> values of I-PARPi-01 (4 µM for MDA-MB-468 and 37 µM for HCC1937) and 0.1 MBq of [<sup>125</sup>I]I-PARPi-01 were either dissolved in 0.5% DMSO in cell medium for the naked combination or co-loaded in micelles (micelle content 2.5% in cell medium). Controls included 0.5% DMSO without drugs or 2.5% unloaded micelles. Cells were incubated under standard conditions for 24, 48, and 72h.

After incubation the cells were washed with PBS, followed by cell fixation with 4% PFA for 10 minutes at RT. Next, the cells were washed again 3x with PBS and permeabilized with 0,1% Triton-X in PBS for 30 minutes at RT. Triton-X was removed, and the cells were blocked with 10% goat serum for 90 minutes at RT. Cells were incubated with mouse α-PARP1 and rat α-γ-H2A.X-AF488 primary antibodies (1:500 in goat serum) at 4° overnight, protected from light. After washing, the secondary antibody goat α-mouse IgG-Cy5 (1:250) was applied for 2h at RT. Cells were washed and stained with DAPI (1:300 in methanol) and incubated for 10 min at RT, protected from light. After washing, samples were sealed with Mowiol®.

Samples were analyzed using fluorescence microscopy with a 40x zoom. Analysis was performed using “ZEN 2012” (Carl Zeiss Microscopy) software. Fluorescence intensity of 30 nuclei of each triplicate was quantified (n=3).

### 2.2.6 In Vivo Experiments

#### 2.2.6.1 Animal care conditions

All animal experiments were approved by a German competent authority (Landesamt für Natur, Umwelt und Verbraucherschutz Nordrhein-Westfalen) for compliance with the Animal Protection Act in conjunction with the regulation for the protection of animals used for experimental and other scientific purposes (Project-file number 81-

## Materials and Methods

02.04.2018.A279). Female NOD.CB17-Prkdschid/Rj mice at 5-9 weeks age were purchased from Janvier Laboratories and housed under a 12-h-light/12-h-dark cycle with free access to food and water. The RT and relative humidity were kept between 20–25°C and 45–65%, respectively.

### 2.2.6.2 Tumor Xenografts

For each mouse,  $3 \times 10^6$  HCC1937 cells were suspended in a 1:1 (volume) mixture of culture media: Matrigel matrix. Mice were inoculated with this cell suspension (max 200  $\mu$ l) subcutaneously in the right flank. Tumor growth was monitored daily using a digital calliper. Tumor volume was calculated according to formula (3) [164]:

$$\text{Tumor volume [mm}^3\text{]} = \text{Tumor length [mm]} \times \text{Tumor breadth}^2\text{[mm]} \times 0.52 \quad (3)$$

The value 0.52 is utilized in calculating the volume of elliptical shapes, as it approximates  $\pi/6$ . Upon reaching of a tumor volume of 500 mm<sup>3</sup>, animals were proceeded for experiments.

### 2.2.6.3 Free Drugs Formulation for Mouse Injection

[<sup>123/125</sup>I]-PARPi-01 in Ethanol was heated to 80°C to evaporate organic solvent. Subsequently, 0.3 mg of I-PARPi-01 was dissolved in 5  $\mu$ L of DMSO and combined with dried [<sup>123</sup>I]-PARPi-01 (15 MBq  $\pm$  3) or [<sup>125</sup>I]-PARPi-01 (30 MBq  $\pm$  5). A mixture of Cremophor and ethanol (in a 2:1 ratio) of 15  $\mu$ L was then added to the DMSO solution containing the drugs. Finally, the mixture was brought to volume with sterile 0.9% sodium chloride in water for injection.

### 2.2.6.4 Co-Loaded Micelles for Mouse Injection

Micelles were prepared at a concentration of 30 mg/mL of mPEG-b-p(HPMAm-Bz), incorporating 1% Cy7-labeled polymer. These micelles were co-loaded with either 30 MBq/mL [<sup>123</sup>I]-PARPi-01 or 70 MBq/mL [<sup>125</sup>I]-PARPi-01, along with 0.6 mg/mL I-PARPi-01, as detailed in chapter 2.2.4.1.

## Materials and Methods

Following the preparation, the micelles underwent filtration (through nylon membranes, pore size: 0.2  $\mu\text{m}$ ) and were subsequently concentrated using centrifugal concentrator columns for 45 minutes at 4000 g. To retrieve the supernatant, the centrifugal concentrator columns were inverted and centrifuged again for 10 minutes at 4000 g.

From the collected supernatant, approximately 15-18 MBq of [ $^{123}\text{I}$ ]I-PARPi-01 or 30-35 MBq [ $^{125}\text{I}$ ]I-PARPi-01 (around 50  $\mu\text{L}$ ) were obtained, which were then diluted to a final volume of 100  $\mu\text{L}$  with sterile 0.9% sodium chloride in water for injection. The final injection formulation thus contained approximately 15 mg of mPEG-*b*-p(HPMAm-Bz) with 1% Cy7-labeled polymer and 0.3 mg of I-PARPi-01.

### 2.2.6.5 Biodistribution Study - Small Animal SPECT/CT Imaging

Imaging was performed with a small animal SPECT/CT system (X-Cube and  $\gamma$ -Cube, Molecubes, Gent, Belgium). Mice bearing subcutaneous HCC1937 tumors upon reaching tumor volume of 500  $\text{mm}^3$  were intravenously administered with the free tracer [ $^{123}\text{I}$ ]I-PARPi-01 ( $17.1 \pm 2.5$  MBq), a free drugs formulation of [ $^{123}\text{I}$ ]I-PARPi-01 and I-PARPi-01 ( $19.7 \pm 0.9$  MBq and  $0.3 \pm 0.01$  mg, respectively), and [ $^{123}\text{I}$ ]I-PARPi-01 and I-PARPi-01 ( $17.1 \pm 1.8$  MBq and  $0.3 \pm 0.01$  mg, respectively) co-loaded micelles (prepared with 30 mg/mL polymer) via lateral tail-vein using a catheter under 1.5 to 2.5% isoflurane sedation in medical grade pressurized air at 0.8 L/min.

Tracer injections contained 0.9% NaCl in a total volume of 100  $\mu\text{L}$ . Administered dose was calculated by subtraction of decay-corrected syringe activity post-injection (p.i.) from pre-injection activity. Each mouse was scanned at 0.5h, 4 h and at 24 h p.i.

The CT acquisition settings were as follows: default high resolution protocol, 440 uA, 50 kVp, 32 ms exposure time, and 1080° rotation in a spiral mode with 960 exposures/360°; the duration of each CT scan was ~5 min. A SPECT scan was initiated at the end of each CT scan.

The SPECT acquisition settings were as follows: 7-headed camera equipped with a general-purpose collimator with 28 pinholes (*i.e.*, 0.75 mm apertures and a radius of rotation of 20 mm), helical scan with 82 bed positions; the total duration of each SPECT scan was 30 min. Both CT and SPECT axial fields of view were selected at 105 mm. During the

## Materials and Methods

scans, the isoflurane concentration was adapted to achieve a respiratory rate between 75 and 50 breaths per minute.

Animals were sacrificed 48h p.i.. Subsequently, organs were excised, weighed, and incorporated radioactivity was determined in a Wizard2 gamma counter. Mean tumor and organ uptake was determined from decay corrected tissue radioactivity normalized to injected dose and tissue sample weight (%ID/g tissue wet weight).

### *2.2.6.6 Small Animal SPECT/CT Reconstruction*

SPECT data were reconstructed using a 3-dimensional maximum likelihood estimation method (i.e., MLEM-3D with 50 iterations) with an energy window of  $\pm 10\%$  from a peak of 141,511 keV to an isometric voxel size of 0,25 mm in a  $141 \times 141 \times 425$  matrix.

SPECT and CT images were automatically aligned after reconstruction using the matrix generated from a capillary phantom scan.

Images were exported and post-processed on PMOD software, version 4.4 (PMOD technologies, Switzerland). For the 2D image presentation, the PFUS tool from Pmod was used. To exclude the bed and other objects from the CT image, an automatic isocontour detection around the mouse using -500 HU as a minimal threshold on the coronal view was used. The newly created images were used to show exemplary CT by capturing with a window from - 1000 to +1000 HU.

### *2.2.6.7 Therapy Study*

For therapy studies animals were randomized for control (n=10) or [ $^{125}\text{I}$ ]I-PARPi-01 administration (n=10). Randomisation was done based on equivalent distribution of tumor volumes. Humane end point is determined as reaching of either of the following conditions: 15 mm tumor diameter, 1500 mm<sup>3</sup> tumor volume, or development of ulcers/ascites.

Mice were administered iv via lateral tail vein with Saline (0.9% NaCl), [ $^{125}\text{I}$ ]PARPi-01 ( $30.4 \pm 2.9$  MBq/dose), a mixture of free [ $^{125}\text{I}$ ]PARPi-01 and I-PARPi-01 ( $31.7 \pm 0.3$  MBq and  $0.3 \pm 0.01$  mg, respectively), and [ $^{125}\text{I}$ ]PARPi-01 and I-PARPi-01 ( $31.1 \pm 2.1$  MBq and  $0.3 \pm 0.01$  mg, respectively) co-loaded micelles (prepared with 30 mg/mL polymer) in either two doses administered weekly or one dose. Rhodamine-labeled lectin (*Ricinus Communis*

## Materials and Methods

Agglutinin I) was injected i.v. to the mice ten minutes prior to sacrifice, to identify functional and perfused vessels. Organs were resected for further *ex vivo* analyses

### *2.2.6.8 Whole-Body Radioactivity*

For the first five days following the therapeutic injection, alongside the daily weight measurements the mice underwent also an assessment of their overall body radioactivity. Each mouse was positioned in a 1-liter glass beaker, and radioactivity was detected *via* a portable radiation contamination monitor from a fixed distance of 30 centimeters.

### *2.2.7 Ex Vivo Experiments*

#### *2.2.7.1 Organ Preparations for Histological Characterizations*

For *ex vivo* imaging, organs were fixed in Roti®Histofix medium for 24 hours at 4°C and then dehydrated in 30% sucrose (wt%) for an additional 24 hours at RT. Following this, the organs were embedded in optimal cutting temperature (OCT) matrix compound (Tissue-Tek) for cryosectioning and stored at –20°C. Cryosections of six micrometers in thickness were prepared for subsequent experiments.

#### *2.2.7.2 Co-Localization of Cy7-Labeled Micelles with Macrophages*

The cryoslices were washed with PBS, and samples were surrounded with PAP pen. Primary antibody rabbit anti-mouse F4/80 (1:500) in 12% BSA/PBS was incubated for 60 minutes at RT. Samples were afterwards washed with PBS. Secondary antibody goat anti-rabbit AF488 (1:1000) in 12% BSA/PBS was incubated for 45 min at RT protected from light. Samples were washed with PBS and counterstained with DAPI fluoromount medium.

Images of the fluorescently stained slides were acquired using an AxioImager M2 microscopy system with an AxioCamMRm Rev.3 camera. Representative images per tumor were taken using 400 ms exposure time settings for GFP channel and 100 ms exposure time for DAPI channel.



## Materials and Methods

### *2.2.7.3 Microautoradiography (MAURA)*

After therapy, cryosections were washed with PBS. Subsequently, the slides were coated with NTB solution, ensuring protection from light, and incubated at  $-20^{\circ}\text{C}$  in the dark for six days. Following this incubation period, the slides were equilibrated at RT for 30 minutes and then subjected to a series of treatments: incubated in developer for 5 minutes, rinsed in distilled water for 0.5 minutes, treated with fixing solution for 10 minutes, and finally washed again in distilled water for 10 minutes. The slides were then stained with hematoxylin and eosin (H&E) for visualization.

### *2.2.7.4 H&E Staining*

For Haematoxylin–Eosin staining the (6  $\mu\text{m}$ ) cryosections were washed with PBS thrice 10 min each followed by Haematoxylin (10 min) and washed with water. Subsequently tissues were incubated with Eosin (1 min) followed by wash twice in PBS for 5 min. Dehydration steps (70% Ethanol, 96% Ethanol and 100% Ethanol, 100 % Xylol) were then performed 2 min in each solvent. The tissues were then mounted and proceeded for bright light microscopy.

### *2.2.7.5 $\gamma$ -H2AX Antibody Staining on Cryosections*

Antigen retrieval: the cryoslides were washed with PBS. Cryoslides were retrieved in  $100^{\circ}\text{C}$  sodium citrate for 20 min. Cryoslides were cooled down to RT and washed with PBS. Cryosections were permeabilized in 0.5% Triton X 100 in PBS at RT for 30 min. Samples were blocked with 5% FBS in PBS at RT for 30 min. Every sample was circled with PAP pen and 100 – 200  $\mu\text{L}$  of 1  $\mu\text{g}/\text{mL}$  Alexa Fluor® 488 anti- $\gamma$ -H2AX antibody was dropped onto sample, protected from light. Samples were incubated at  $4^{\circ}\text{C}$  overnight. On the next day, samples were washed with PBS and counterstained with DAPI fluoromount medium.

Images of the fluorescently stained slides were acquired using an AxioImager M2 microscopy system with an AxioCamMRm Rev.3 camera. Three slides of each organ were stained and five representative images per slide were quantified using 400 ms exposure time settings for GFP channel and 100 ms exposure time for DAPI channel.

## 3 Results and Discussion

### 3.1 Formulation of Auger Electron-Emitting PARP inhibitors in Polymeric Micelles

#### 3.1.1 Preparation of PARP inhibitor Single-Loaded $\pi$ electron-stabilized HPMA-based micelles

The block copolymer used to prepare the  $\pi$  electron-stabilized polymeric micelles, i.e., mPEG-*b*-p(HPMAm-Bz), was synthesized by free radical polymerization via a macroinitiator route by the working group of Prof. Lammers (Institute for Experimental Molecular Imaging, University Hospital RWTH Aachen) [161, 162]. The PARPi I-PARP-01-loaded micelles were formulated using a standard nanoprecipitation method. Specifically, a THF solution of mPEG-*b*-p(HPMAm-Bz) polymers and I-PARPi-01 was dropwise added into MilliQ water under stirring, followed by evaporation of THF for at least 24 h.

Non-radioactive I-PARPi-01 single-loaded polymeric micelles (Figure 7A) were first prepared, exploring the impact of different amounts of polymer on the physicochemical properties of the final formulations. 10 mg/mL, 20 mg/mL or 30 mg/mL polymer concentration were used, and the micelles were analyzed in terms of their size and polydispersity index (PDI) (Figure 7B). In all cases, the I-PARP-01 feed amount was kept constant at 0,5 mg/mL. After evaporation, the Z-average particle size of the polymeric micelles as measured by DLS was 72 nm ( $\pm$  8.0) for 10 mg/mL, 76 nm ( $\pm$  0.7) for 20 mg/mL and 73 nm ( $\pm$  4.9) for 30 mg/mL of polymer (with PDI of 0.09 ( $\pm$  0.01), 0.15 ( $\pm$  0.01) and 0.10 ( $\pm$  0.02), respectively, thus indicating a narrow size distribution). Therefore, no significant differences were observed in the physicochemical properties of the particles based on the amount of polymer used in the formulation of the micelles. In general, it has been reported that nanoparticles ranging from 30 to 100 nm in size can effectively accumulate in permeable tumors [165]. In contrast, highly fibrotic, poorly permeable tumors are primarily penetrated by micelles measuring around 30 nm or below [166], together

## Results and Discussion

highlighting the critical role that size plays in the biodistribution and tumor accumulation of micelles.

Regarding I-PARP-01 loading, all the formulations showed a high encapsulation efficiency (EE) ( $> 80\%$  for 10 mg/mL and 20 mg/mL polymer, and  $> 90\%$  for 30 mg/mL polymer), all at a I-PARPi-01 feed concentration of 0.5 mg/mL. The corresponding loading capacities (LC) were 3.7 wt% ( $\pm 0.8$ ), 1.6 wt% ( $\pm 0.2$ ) and 1.5 wt% ( $\pm 0.1$ ), respectively (Figure 7C), which is similar to those achieved with other micellar nanomedicine formulations loaded with PARPi like olaparib [149].

The study of micelle morphology is essential for predicting their behavior *in vivo*, as the shape of these NCs significantly influences circulation time, biodistribution, and cellular uptake [167]. Transmission electron microscopy (TEM) confirmed that all the micelle formulations were homogeneously constituted by spherical particles (Figure 7D) and confirmed the size of around 70 nm observed in DLS.

Most studies focus on spherical NCs due to their easier manufacturing, whereas rod-like or worm-like micelles show significantly longer blood circulation times [168, 169]. Despite the circulation advantages of non-spherical NCs, spherical structures are favored for their superior cellular uptake [170, 171], attributed to their optimal interaction with cell membranes, which is essential for therapeutic efficacy [167].

All the micelle formulations were able to effectively retain I-PARP-01. Yet, different polymer concentrations showed a slight impact on the retention efficiency of the I-PARPi-01, releasing 66% ( $\pm 5.8$ ), 50% ( $\pm 3.6$ ) and 50% ( $\pm 8.0$ ) of the drug (for 10 mg/mL, 20 mg/mL and 30 mg/mL polymer, respectively) after 48 h in a BSA solution at 37 °C (Figure 7E). Release studies under similar conditions have recently been shown to adequately predict *in vivo* blood circulation of drugs formulated in such polymeric micelles [172]. These findings suggest that higher concentrations of polymers in micelle formulations lead to enhanced drug retention efficiency and prolonged drug release kinetics, with very similar performance between 20 mg/mL and 30 mg/mL. Research has concentrated on developing NC formulations under 100 nm in diameter that can exploit the EPR effect [165] for selective tumor accumulation while ensuring prolonged drug encapsulation with a release half-time of several hours or more [173].

## Results and Discussion

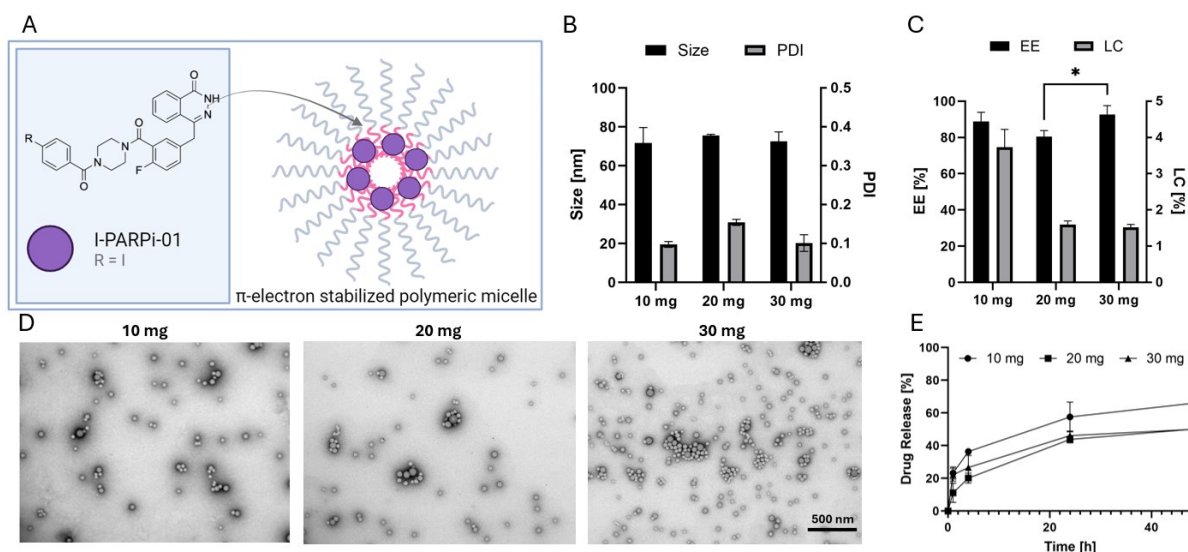


**Figure 7. Formulation and characterization of PARPi-loaded [mPEG-*b*-p(HPMA-Bz)]-based micelles.** 0.5 mg/mL I-PARPi-01 single-loaded nano formulations were prepared using varying concentrations of polymer (10, 20, 30 mg/mL). Values represent average  $\pm$  SD. **(A)** Schematic overview of I-PARPi-01 single-loaded polymeric micelle. **(B)** Size and PDI measured by DLS ( $n \geq 3$ , two-way ANOVA and Tukey's multiple comparisons test, ns). **(C)** Encapsulation efficiencies (EE) and loading capacities (LC) ( $n = 3$ , two-way ANOVA and Tukey's multiple comparisons test, \*  $p < 0.05$ ). **(D)** Representative TEM images. Scale bar = 500 nm. **(E)** Drug release profile of micelles under sink conditions at 37 °C (in PBS, pH 7.4, containing 45 mg/mL of BSA). All the micelle formulations were prepared using 0.5 mg/mL feed amount of I-PARPi-01 ( $n = 3$ ).

Our first goal was to create a stable PARPi micellar formulation that effectively encapsulates and retains non-radioactive I-PARPi-01, as well as eventually radioactive [ $^{125}$ I]I-PARPi-01 *in vivo*.

Given the favorable characteristics of size, PDI, EE, and optimal drug release profiles, a polymer dosage of 30 mg/mL was chosen for the co-encapsulation of I-PARPi-01 and [ $^{125}$ I]I-PARPi-01. Furthermore, multiple studies utilizing 30 mg/mL ( $\pm 3$ ) of this specific polymer have demonstrated promising performance along with high safety and tolerability [127, 140, 174].

### 3.1.2 Co-Loading non-radioactive and radioactive PARP inhibitor in Polymeric Micelles

Upon validating the efficient encapsulation and retention of the non-radioactive I-PARPi-01 within mPEG-*b*-p(HPMAm-Bz)-based polymeric micelles, the co-encapsulation with the radiolabeled [ $^{125}$ I]I-PARPi-01 was investigated. This involved at first the radiosynthesis

## Results and Discussion

of [ $^{125}\text{I}$ ]I-PARPi-01, followed by the encapsulation of [ $^{125}\text{I}$ ]I-PARPi-01 within the same polymeric micelle platform and assessing its pharmaceutical properties in both, single- and co-loaded configurations alongside the non-radioactive I-PARPi-01 for the purpose of combination radio-chemotherapy.

### 3.1.2.1 Radiotracer Synthesis

PARPi-01 labelled with  $^{125}\text{I}$  (i.e., [ $^{125}\text{I}$ ]I-PARPi-01) was prepared through a direct  $^{125}\text{I}$ -iododestannylation process involving the tributylstannyl-benzoylated derivative of olaparib and chloramine T as the oxidizing agent (Figure 8A), following previously reported procedures in our group [79, 80]. The radiochemical purity of the synthesis exceeded 98%, as observed by radio-HPLC (Figure 8B) with a yield of 82 % ( $\pm 10$ ). Long-term storage at  $-20^\circ\text{C}$  in ethanol or THF for more than three months did not result in any deiodination. The molar activity of [ $^{125}\text{I}$ ]I-PARPi-01 was 30.52 GBq/ $\mu\text{mol}$  ( $\pm 6.4$ ), based on previously reported values [80].

Similar synthetic methods have been reported in the literature for other Auger-emitting theranostics. For instance, Wilson et al. described a similar straightforward protocol for the structurally similar Auger-emitting theranostic [ $^{123}\text{I}$ ]I-MAPi, albeit with a lower yield of 45% ( $\pm 2$ ) and a reduced molar activity of 11.8 GBq/ $\mu\text{mol}$  ( $\pm 4.8$ ) [175].

Importantly, the synthesis protocols for radiolabeled I-PARPi-01 using  $^{123}\text{I}$ ,  $^{131}\text{I}$ , and  $^{125}\text{I}$  follow the same procedure. Changing the radioactive iodine isotope does not impact the chemical properties of the final I-PARPi-01 tracer.

## Results and Discussion

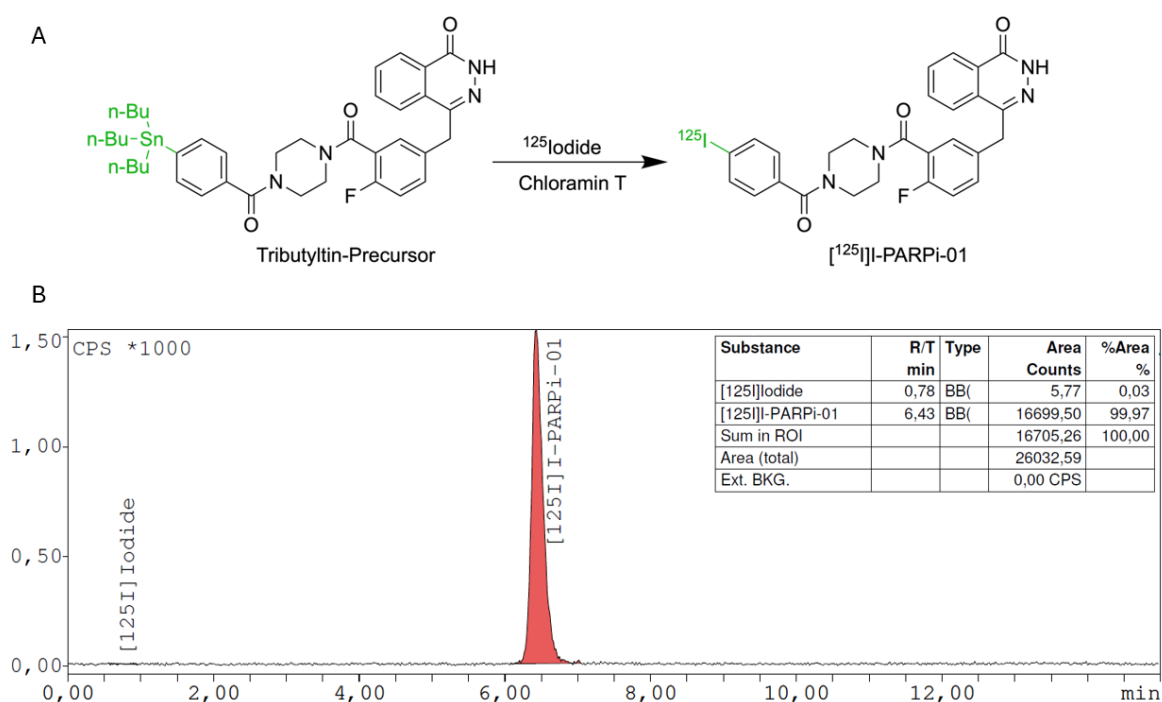


**Figure 8. Radiolabeling of  $[^{125}\text{I}]\text{I-PARPi-01}$ .** (A) Reaction scheme for radiolabeling with  $^{125}\text{I}$  in the presence of the oxidant chloramin T to a tributyltin-precursor (olaparib derivative) for obtaining  $[^{125}\text{I}]\text{I-PARPi-01}$ . (B) Radio HPLC chromatogram of purified  $[^{125}\text{I}]\text{I-PARPi-01}$  (gradient elution method (Solvent A:  $\text{H}_2\text{O}/\text{Trifluoroacetic acid}$  (99.9/0.1% v/v); and Solvent B: Acetonitrile) at a flow rate of 1 mL/min and a HPLC affinity C18 column were used).

### 3.1.2.2 Pharmaceutical evaluation of co-loaded Non-Radioactive and Radioactive PARP inhibitors in Polymeric Micelles

Following the successful synthesis of  $[^{125}\text{I}]\text{I-PARPi-01}$ , the objective was to develop a stable formulation of co-loaded non-radioactive and radioactive PARP inhibitors ( $[^{125}\text{I}]\text{I-PARPi-01}/\text{I-PARPi-01}$ ) encapsulated within polymeric micelles (Figure 9A).

It is important to note that the choice of iodine radioisotope does not alter the chemical properties of the final tracer,  $[^{125}\text{I}]\text{I-PARPi-01}$ . However, for cost considerations and ease of procurement,  $^{131}\text{I}$  was selected instead of  $^{125}\text{I}$ .

To achieve this, the same nanoprecipitation method utilized for the single-loaded I-PARPi-01 within mPEG-*b*-p(HPMAM-Bz) polymeric micelles was employed. Specifically, I-PARPi-01 and  $[^{131}\text{I}]\text{I-PARPi-01}$  were prepared at feed concentrations of 0.5 mg/mL and 5 MBq/mL, respectively, in a THF solution containing 30 mg/mL of polymer. This solution was added dropwise to MilliQ water while maintaining constant stirring for 1 minute. The resulting mixture was allowed to stand undisturbed at RT for approximately 20-24h to

## Results and Discussion

facilitate the evaporation of THF. Subsequently, the solution was filtered through a 0.2  $\mu\text{m}$  nylon membrane filter to eliminate any free, non-encapsulated PARPi and aggregates.

The results confirm that radioactive and non-radioactive PARPi were effectively co-loaded in the  $\pi$  electron-stabilized polymeric micelles. The polymeric micelles demonstrated high EE for both drugs, with EE values over 80%, and, with the non-radioactive I-PARPi-01 exhibiting slightly higher EE (> 90%) compared to [ $^{131}\text{I}$ ]I-PARPi-01 (> 80%) (Figure 9B). Given the chemical identity of both drugs, further investigations would be required to elucidate the observed differences in EE values between the two compounds.

The corresponding LC were 1.5 wt% for I-PARPi-01 and close to 0 wt% (i.e.,  $1.37 \times 10^{-9}$  wt%) for [ $^{131}\text{I}$ ]I-PARPi-01. The low LC of [ $^{131}\text{I}$ ]I-PARPi-01 can be explained based on that less than 1 femtomole (i.e.,  $<10^{-15}$  moles) of tracers are present when dealing with radioactive samples. The molar activity of  $^{131}\text{I}$  is defined as  $5.99 \times 10^{23}$  Bq/mol [176].

Calculation of the molar amount of  $^{131}\text{I}$  within this micelle formulation, with a feed amount of 5 MBq, was done following equation (4):

$$\frac{5.0 \times 10^6 \text{ Bq}}{5.99 \times 10^{23} \text{ Bq/mol}} = 8.347 \times 10^{-18} \text{ mol} \triangleq 8,347 \times 10^{-3} \text{ Fmol} \quad (4)$$

With a purity of > 99% (see Figure 8B), it is ideally estimated that no free  $^{131}\text{I}$  is inside the solution. Together with the molar mass of [ $^{131}\text{I}$ ]I-PARPi-01 (594.40 g/mol), the actual mass of 5 MBq can be calculated with the following equation:

$$\text{Mass [g]} = \text{Molar mass} \left[ \frac{\text{g}}{\text{mol}} \right] \times n \quad (5)$$

$$\rightarrow 594.40 \frac{\text{g}}{\text{mol}} \times (8.347 \times 10^{-18}) = 4,96 \times 10^{-14} \text{ g} \triangleq 4.96 \times 10^{-11} \text{ mg}$$

Using the above mass of [ $^{131}\text{I}$ ]I-PARPi-01 compound (with an EE of 83 % in the micelles) into formula (2) to determine the LC:

$$LC = \frac{\text{detected amount of drug}}{\text{Detected amount of drug} + \text{feed amount of polymer}} \times 100 \quad (2)$$

$$\rightarrow \frac{0.83 \times 4.96 \times 10^{-11} \text{ mg}}{(0.83 \times 4.96 \times 10^{-11} \text{ mg}) + 30 \text{ mg}} \times 100 = 1.37 \times 10^{-9} \%$$

With the denominator in the fraction being disproportionately larger than the numerator, the resulting LC approaches nearly zero.

TEM images confirmed that the co-loaded micelles preserved the spherical shape, with sizes of around 70 nm (Figure 9C), i.e., similar to the single-loaded PARPi micelles and empty micelles [140].

Furthermore, the drug release profiles of various formulations of I-PARPi-01 and [<sup>131</sup>I]-PARPi-01 co-loaded/co-administered micelles were systematically compared for 48h in a BSA-containing PBS solution (pH 7.4) at 37 °C (Figure 9D). The objective was to determine whether there are differences in the drug retention between the different formulations, which include co-loaded micelles, mixed single-loaded micelles, and single-loaded separately released micelles; ultimately aiming to identify the most optimal formulation (i.e., with the better drug retention) for further biological evaluation.

Data indicate a rapid release of the radioactive as well as the non-radioactive PARPi during the first hours. This phenomenon can be attributed to the initial burst release, which occurs due to drug molecules that are attached to the surface of the micelles rather than stably loaded inside their cores [177]. For the single-loaded micelles (single-release), the drug release profile shows that approximately 53% of the drug is released from non-radioactive loaded micelles (Figure 9D), while around 62% of radioactive compound was released from the micelles after 48 hours.



## Results and Discussion

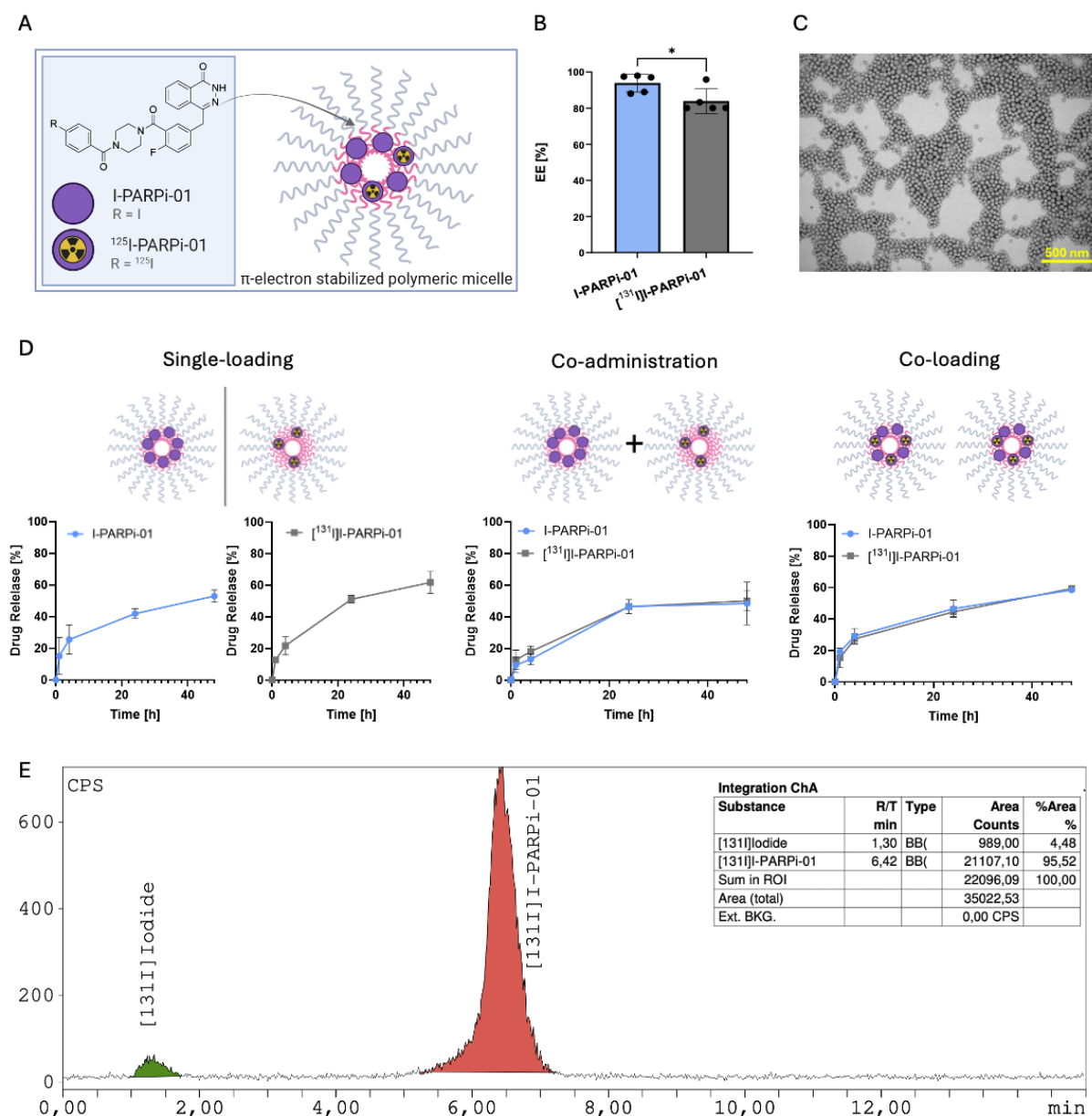


**Figure 9. Co-loading of non-radioactive and radioactive PARPi in mPEG-*b*-p(HPMAm-Bz) polymeric micelles.** Values represent average  $\pm$  SD. **(A)** Schematic overview of I-PARPi-01 and  $[^{131}\text{I}]$ -PARPi-01 co-loaded in polymeric micelle. **(B)** Encapsulation efficiencies of co-loaded I-PARPi-01 and  $[^{131}\text{I}]$ -PARPi-01 in polymeric micelles ( $n = 5$ , Data were statistically analyzed by unpaired t-test. \*  $p < 0.05$ ). **(C)** Representative TEM image of co-loaded micelles with 0.5 mg I-PARPi-01 and 5 MBq of  $[^{131}\text{I}]$ -PARPi-01. Scale bar = 500 nm. **(D)** Comparison of individual drug release profiles under sink conditions at 37 °C (in PBS, pH 7.4, containing 45 mg/mL of BSA). All the micelle formulations were prepared using 0.5 mg/mL feed amount of I-PARPi-01 and / or 5 MBq  $[^{131}\text{I}]$ -PARPi-01, and 30 mg/mL mPEG-*b*-p(HPMAm-Bz) polymer ( $n = 3$ ). Drug release profiles of single-loaded micelles in single-release, or a mixture of micelles single-loaded, or co-loaded micelles. Drug release was detected via (radio) HPLC. **(E)** Representative radio HPLC chromatogram of  $[^{131}\text{I}]$ -PARPi-01 drug release from polymeric micelles after 48h at 37°C in PBS (pH 7.4), containing 45 g/L BSA for all release conditions. Gradient elution method (Solvent A:  $\text{H}_2\text{O}$ /Trifluoroacetic acid (99.9/0.1% v/v); and Solvent B: Acetonitrile) at a flow rate of 1 mL/min and a HPLC affinity C18 column were used.

In the case of the co-administered formulation (Figure 9D), both drugs exhibit similar release rates, converging at approximately 55% for the non-radioactive PARPi release and 52% for the radioactive drug release. For the co-loaded micelles (Figure 9D), the results

## Results and Discussion

indicate that both drugs have been co-delivered, with about 61% of release of both drugs after 48 hours. Furthermore, the HPLC chromatograms of [<sup>131</sup>I]I-PARPi-01 exhibited no additional peaks in all drug release conditions, indicating that there were no side products formed as a result of interactions with the polymer of the micelles or any degradation of the radiotracer upon its release from the micelles (Figure 9E). In conclusion, there is no significant difference in the drug release profiles among different loading and release conditions. Given that the co-loaded micelles exhibited the most balanced drug release profile between the two drugs, this approach was selected for subsequent experiments. Furthermore, the improved efficiency of the micelle formulation by simultaneous drug co-loading was also considered in the decision-making process. The objective is to maximize the co-localization of the drugs at the target site, which necessitates the co-loading of micelles for concurrent drug delivery. This strategy is particularly crucial in cases where synergistic effects may be present, as exemplified by the Vyxeos liposomal formulation that co-loads and co-delivers daunorubicin and cytarabine [178].

Several other reported studies have also loaded PARPi (and more specifically olaparib) into different polymeric NCs. For instance, Misra and colleagues loaded the PARPi olaparib into PLGA polymeric micelles, resulting in approximately 45% of olaparib release after 48 h [148]. While it apparently seems that our  $\pi$  electron-stabilized polymeric micelle formulation shows poorer retention of I-PARPi-01 and [<sup>131</sup>I]I-PARPi-01, it is also important to note that the study of Misra et al. evaluated the drug release kinetics in PBS without the addition of BSA. The inclusion of BSA in the release medium enhances the drug release rate of lipophilic drugs, due to the relatively high affinity of lipophilic drugs to the hydrophobic pockets of albumin [172, 179]. In two other cases, formulations of PCEC [144] and mPEG-PCL [89] polymers were used to encapsulate olaparib, showing a slightly improved retention (70 % retention) after 48 h in both cases under sink conditions in PBS containing Tween-80 (0.5 %, w/w).

### 3.1.3 Concentrated Fluorescent Micelles for *In Vivo* Applications

To obtain a formulation that could be used for *in vivo* applications, I explored the possibility of fluorescently labeling the polymers and concentrating the formulation, to achieve a dose of 15 mg/kg bodyweight of I-PARPi-01. The dosing regimen for olaparib in

## Results and Discussion

patients ranges from 2 mg/kg to 15 mg/kg body weight [180]. Additionally, various animal studies have employed iv dosages of up to 50 mg/kg body weight [144]. Consequently, I opted to utilize the maximum dosage observed in patient treatments for our formulation. According to GV-SOLAS guidelines, a maximum of 5 mL/kg body weight is allowed for iv injections in mice.

Polymers labelled with cyanine dye (Cy7) were obtained from the working group of Prof. Lammers (Institute for Experimental Molecular Imaging, University Hospital RWTH Aachen) [174]. The synthesis of micelles was conducted using the same procedure as previously described (see chapter 3.1.1), but with variations in the composition, incorporating different amounts of Cy7-labeled polymer blended with unlabeled polymer. Following the synthesis, the concentration of the formulations was assessed using centrifugal concentrator columns to achieve the desired formulation characteristics. In all experiments, we aimed to evaluate the comparability of the Cy7-labeled micelle formulation with the non-radioactive I-PARPi-01, which was utilized for loading into the hydrophobic core of the micelles. Previous studies indicated that there is no significant difference in drug release profiles between micelles that were single-loaded and those that were co-loaded (Figure 9D). Therefore, to prioritize radiation safety, I decided to perform these experiments exclusively with 0.5 mg/mL non-radioactive I-PARPi-01 single-loaded micelles.

Non-radioactive I-PARPi-01 single-loaded polymeric micelles were prepared containing 100 %, 2 % or 1 % of Cy7-conjugated mPEG-*b*-p(HPMAm-Bz) polymer and analyzed regarding their size and PDI (Figure 10A). After evaporation and filtration (and centrifugal concentration for the 1% concentrated (conc.) batch, as a proof-of-concept) the Z-average of the polymeric micelles, as measured by DLS, was found to be 51 nm for 100 % Cy7-polymer, and 84 nm for formulations containing 2 %, 1 %, and 1 % (conc.) of Cy7-conjugated polymers. The PDI values were 0.17, 0.13, 0.14, and 0.14, respectively. Although there were no significant differences in PDI across the various formulations, the micelle size formulated with 100% Cy7-conjugated polymer was significantly smaller when compared to all other groups.

## Results and Discussion

As observed from the data, increasing the percentage of the amine derivative of Cy7 into the micelle formulation composition resulted in a decrease in particle size, although the degree of polymerization remained unchanged for the Cy7-labeled polymer. Interestingly, the smaller size of micelles when formulated using 100% of Cy7-conjugated polymers indicates that the concentration and ratio of the dye-conjugated polymer in the final micelle composition plays a significant role in some physicochemical properties such as size, a feature that would be interesting to further explore in the future for optimal micelle formulation.

Furthermore, it can be observed that concentrating the micelle formulations from 30 mg/mL to 300 mg/mL did not influence size or PDI, thus suggesting that no aggregates were formed during the concentration process, and that the nanoparticles were homogeneous.

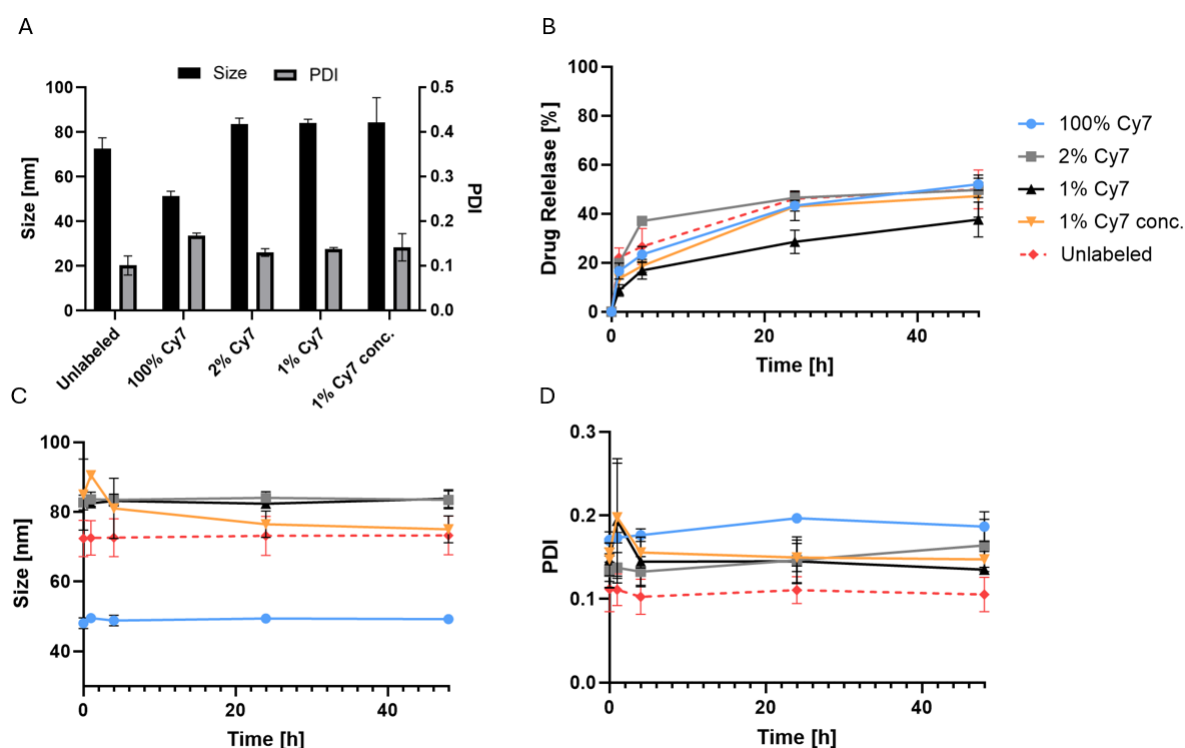


**Figure 10. Pharmaceutical evaluation of I-PARPi-01 single-loaded Cy7-labelled polymeric micelles.** The micelles were formulated with 30 mg/mL of polymer and varying concentrations of Cy7-labeled polymer (unconcentrated and concentrated (conc.)), and loaded with 0.5 mg/mL of I-PARPi-01. Values represent average  $\pm$  SD ( $n=3$ ). **(A)** Size and PDI measured by DLS (two-way ANOVA and Tukey's multiple comparisons test, \*\*\*  $p < 0.001$ ). **(B)** Comparison of individual drug release profiles under sink conditions (in PBS, pH 7.4 containing 45 mg/mL of BSA). **(C)** Size and **(D)** PDI development during drug release.

The I-PARPi-01 release profile was evaluated for the different Cy7-functionalized micelle formulations using a dialysis setup under sink conditions, in a 45 mg/mL BSA-containing

## Results and Discussion

PBS solution (pH 7.4) (Figure 10B). I-PARPi-01 release from 1 % Cy7-conjugated micelles was slower than that of the rest, with around 38 % of drug release after 48h, as compared to the 50-52 % of I-PARPi-01 released within the same timeframe. Considering that the lower the percentage of Cy7-polymers in the formulation, the higher the size, it is logical to think that will also allow for better retention of the drug inside the micelle.

Previous studies have demonstrated that larger mPEG-*b*-p(HPMAM-Bz)-based polymeric micelles (80-90 nm) tend to retain hydrophobic drugs more effectively than smaller micelles (40-50 nm) [181]. This observation may explain why the larger-sized micelles containing 1% Cy7-labeled polymer exhibited stronger drug retention compared to the smaller-sized micelles that were composed of 100 % Cy7-labeled polymer.

However, it is noteworthy that the formulations with similar percentages of Cy7 (specifically, the 1 % concentrated and 2 % formulations) and similar sizes displayed lower drug retention capabilities compared to the 1 % Cy7-unconcentrated formulation. This suggests that, while the release profiles across all formulations showed similarities, there were small differences in drug retention. These variances are likely influenced by the presence of Cy7 and the concentration of the micelles. Consequently, this aspect warrants further investigation to fully elucidate the underlying mechanisms that affect drug release and retention within these formulations.

Besides, serum proteins such as BSA have been shown to influence micelle stability, potentially leading to their disruption or aggregation [182, 183]. However, during the drug release experiments DLS measurements revealed no significant changes in size or PDI (Figure 10C, D). This observation implies that the micelles remain stable and do not aggregate in the presence of serum proteins like albumin while circulating in the bloodstream. Such stability is crucial for ensuring that the therapeutic agents remain for a certain time effectively encapsulated and available for targeted delivery *in vivo*.

In summary, we successfully synthesized fluorescently labeled polymeric micelles capable of stably loading I-PARPi-01, facilitating both visualization and quantification of the nanoparticles in tissue. We also concentrated the micelle formulations to achieve an appropriate volume while maintaining an I-PARPi-01 dosage of 15 mg/kg body weight for *in vivo* applications. Importantly, this concentration process did not compromise the

## Results and Discussion

pharmaceutical properties of the micelles, including size, PDI, and drug retention capabilities. The observed stability of these formulations underscores their suitability for further biological studies and potential therapeutic applications.

### 3.2 *In Vitro* Evaluation of Drug-Loaded Micelles in TNBC

For the *in vitro* performance assessment of the PARPi and PARPi-loaded polymeric micelles, experiments were conducted using three established human breast cancer cell lines—HCC1937, MDA-MB-468, and MDA-MB-231—along with the non-tumorigenic breast cell line MCF10A. This selection provides a diverse portfolio, as these cell lines differ in their characteristics, including disease subtype, BRCA<sup>mut</sup> status, and HR activity (see Table 5).

**Table 5. Characteristics of cell lines used in this study.** The cell lines represent various TNBC disease stages, subtypes, BRCA<sup>mut</sup> status, and homologous recombination (HR) activity. [184]

Cell line	Disease	Subtype	BRCA <sup>mut</sup>	HR activity
HCC1937	primary ductal carcinoma	TNBC basal-like-A	Yes	Defect [184]
MDA-MB-468	Adenocarcinoma	TNBC basal-like-A	No	High [37]
MDA-MB-231	Adenocarcinoma	TNBC Mesenchymal-like	No	Low [37, 185]
MCF10A	Non-tumorigenic	Epithelial	No	Low [185]

#### 3.2.1 PARP Status in TNBC and Comparative Uptake of Free and Encapsulated Forms

As previously mentioned, PARP1 is a key enzyme involved in the DNA damage repair process, particularly in the repair of SSBs through the base excision repair pathway [59]. Understanding its expression levels can help identify which TNBC patients might benefit

## Results and Discussion

from PARPi, as these therapies are designed to exploit the deficiencies in DNA repair mechanisms [60].

To investigate the potential of PARP-targeting in TNBC, first the expression of PARP1 protein level was analyzed in the above-described cell panel (Table 5). Furthermore, exploring the PARP1 expression pattern across different cell lines raises important questions about its potential impact on the cellular uptake of PARPi. Consequently, investigations have been conducted to determine whether PARP1 expression correlates with the cellular uptake of PARPi.

PARP1 expression might potentially serve as a biomarker for predicting response to PARPi therapy. With special regards to breast cancer, high cytoplasmic PARP expression was significantly correlated with undifferentiated tumor pattern, non-lobular cancers and TNBC, whereas no such correlations were found regarding nuclear PARP staining [186]. High levels of PARP1 may indicate that the cells are reliant on its activity for survival, making them more susceptible to PARP inhibition. Conversely, low expression might suggest alternative repair pathways are utilized, indicating a potential lack of response to PARPi [187, 188].

While PARP1 expression has been proven in various breast tumors [189, 190] and TNBC cell lines [36, 37, 80, 191], a quantitative comparison determining the relative expression levels among untreated breast cell lines has not been previously conducted. The expression of PARP1 in both the TNBC cell lines and the healthy breast cell line was assessed using western blot analysis, with relative PARP1 expression quantified across three independent experiments (Figure 11A). PARP1 levels were calculated in relation to the loading control GAPDH and normalized to the non-tumorigenic breast cell line MCF10A, which was assigned a value of 1. All four cell lines were positive for PARP1. The western blot analysis revealed one band at ~116 kDa, corresponding to the full-length PARP1 [190]. Interestingly, compared to MCF10A, the TNBC cell lines exhibited significantly lower levels of PARP1 expression: HCC1937 showed a relative expression of 0.38 ( $\pm 0.09$ ), MDA-MB-468 had 0.34 ( $\pm 0.14$ ), and MDA-MB-231 displayed 0.58 ( $\pm 0.15$ ).

## Results and Discussion

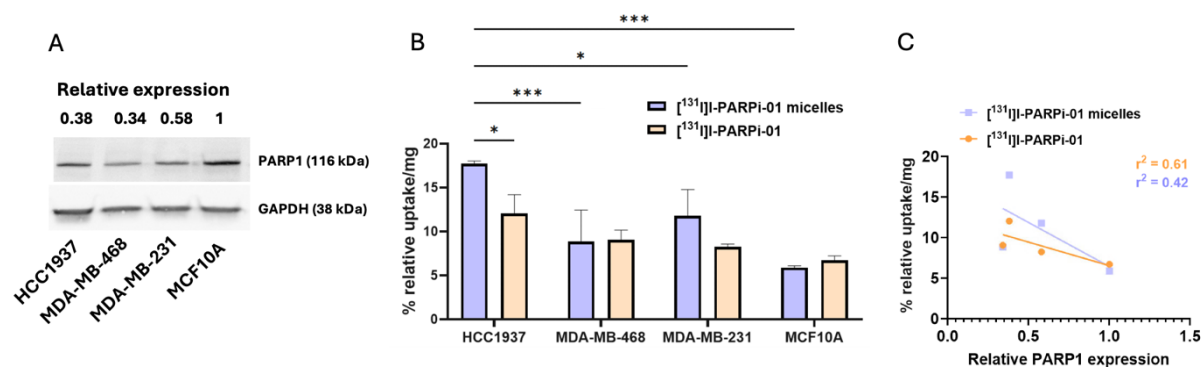


**Figure 11. PARP1 expression and tracer uptake in TNBC.** (A) Representative western analysis of PARP1 expression in untreated whole cell lysates growing in log phase with TNBC cell lines (MDA-MB-231, MDA-MB-468, HCC1937) and benign breast cell line (MCF10A). Equal protein amount was separated by SDS-PAGE, transferred to PVDF, and stained using anti-PARP1 antibody. GAPDH protein levels were used as a loading control. Relative expression represent average for  $n = 3$ . (B) Evaluated cellular uptake of  $[^{131}\text{I}]$ -PARPi-01 (free tracer vs. tracer encapsulated after incubation for 1h at 37°C in different TNBC cell lines (MDA-MB-231, MDA-MB-468, HCC1937) and in healthy breast cell line (MCF10A). Values represent average  $\pm$  SD ( $n=3$ , in triplicates). Data were statistically analyzed by two-way ANOVA multiple comparisons test (\*  $p < 0.5$ , \*\*\*  $p < 0.001$ ). (C) Correlation of relative PARP1 expression with relative tracer uptake.

The cellular uptake of free and micelle-encapsulated  $[^{131}\text{I}]$ -PARPi-01 tracer was evaluated in TNBC cell lines following a 1-hour incubation period at 37 °C with either 0.1 MBq of the free  $[^{131}\text{I}]$ -PARPi-01 or 0.1 MBq of  $[^{131}\text{I}]$ -PARPi-01 encapsulated in micelles (Figure 11B). After incubation with the radioactive tracer, the cells were harvested and the internalized  $^{131}\text{I}$  radioactivity was detected via Gamma counter measurements. This experimental design aimed to assess the impact of encapsulating the tracer in micelles on cellular uptake.

Overall, TNBC cell lines displayed higher uptake levels than the healthy breast cell line, as expected due to the higher metabolism of cancer cells [192]. The highest cellular uptake was observed in the HCC1937 cell line, which demonstrated a statistically significant increase in uptake of 17.7 % ( $\pm 0.3$  %) for the micelle-encapsulated  $[^{131}\text{I}]$ -PARPi-01, compared to 12.0 % ( $\pm 2.1$  %) for the free  $[^{131}\text{I}]$ -PARPi-01 ( $p < 0.05$ ). In contrast, the healthy breast cell line MCF10A exhibited the lowest uptake, with 5.8 % ( $\pm 0.2$  %) for the micelle-encapsulated tracer and 6.7 % ( $\pm 0.5$  %) for the free tracer. Encapsulation of the tracer in micelles significantly increased  $[^{131}\text{I}]$ -PARPi-01 uptake in the HCC1937 and MDA-MB-231 cell lines.

When comparing PARP1 expression with the relative uptake of the PARPi radiotracer, a decent inverse correlation was observed with an  $r^2$  value of 0.61 for the free  $[^{131}\text{I}]$ -PARPi-01 (Figure 11C). The observed correlation between the increasing PARP1



## Results and Discussion

expression and the corresponding decreasing uptake of [ $^{131}$ I]-PARPi-01 raises important questions about the biological implications of PARP1 levels in breast cancer, particularly in TNBC. The overall landscape of PARP1 expression in TNBC remains complex and somewhat contradictory. While some studies show no significant differences among malignant cell lines compared to benign cells [80, 193], others indicate increased PARP1 expression in BRCA<sup>mut</sup> TNBC lines compared to BRCA<sup>wt</sup> cell lines [36]. This highlights the complexity of PARP1 regulation and its potential impact on treatment outcomes, emphasizing the need for further research to clarify the relationship between PARP1 expression, PARPi uptake, and therapeutic sensitivity.

In contrast, the correlation for the micelle-encapsulated [ $^{131}$ I]-PARPi-01 was notably lower, with an  $r^2$  value of only 0.42 (Figure 11C). This diminished correlation suggests that the encapsulation strategy influences the uptake dynamics, as nanoparticles are predominantly internalized by macrophages rather than cancer cells, unlike the unencapsulated PARPi radiotracer [194, 195].

Notably, the malignant cell lines HCC1937 and MDA-MB-231 exhibited an enhanced uptake of the radiotracer when the tracer was encapsulated in micelles. This increased uptake may be attributed to the protective effect of micelles, which shield the tracer from enzymatic degradation processes. This phenomenon has been observed in other studies, where the encapsulation of unstable curcumin within nanoparticles improves its stability and, consequently, its cellular uptake [196].

Sankaranarayanan et al. reported that [ $^{123}$ I]-PARPi-01 exhibited unstable behavior during *in vivo* biodistribution studies, specifically noting that radioactive iodine can be cleaved off and incorporated into the thyroid [79]. This protective effect is crucial, as only the intact tracer—and not free iodine—will be taken up by the cells [79]. By encapsulating the tracer within micelles, its stability may be enhanced, thereby reducing the likelihood of degradation before it is internalized by the target cells. This mechanism not only contributes to the increased cellular uptake observed with micelle-encapsulated tracers but also emphasizes the potential of micellar systems in improving radiotracer stability, which could lead to enhanced therapeutic efficacy while minimizing unintended side reactions.

### 3.2.2 Protection of the Radiotracer from Enzymatic Degradation Using Polymeric Micelles

To investigate whether the micelles can prevent the degradation of the tracer, *in vitro* stability experiments were conducted under various conditions. These experiments assessed the tracer's stability encapsulated in micelles compared to the free  $^{131}\text{I}$ -PARP-01 tracer. Different media, and exposure to enzymatic degradation were systematically varied to evaluate the protective effect of the micelles. The intact tracer in the corresponding medium was monitored via radio-HPLC measurements (Figure 12A). When the tracer was incubated in PBS (pH 7.4) at 37 °C for 72 h, negligible degradation of the tracer was observed (Figure 12B). Both the free  $^{131}\text{I}$ -PARPi-01 tracer and the tracer encapsulated in micelles demonstrated high stability, with > 90 % intact tracer after the 72 h period for both free and micelle-encapsulated formulations. These results indicate that the tracer is stable in aqueous solutions, and that the ions and salts present in PBS do not significantly compromise its stability, likely due to the absence of metabolically active components such as enzymes.

Thus, stability experiments were also conducted in human serum at 37 °C for 72 h (Figure 12C), used to mimic human biological blood fluids. The results demonstrated that more than 88 % of the free tracer remained intact after the 72 h incubation and, > 99 % of the tracer was preserved in the micelle formulations, highlighting the enhanced protective effect of the nanocarriers on the tracer. The obtained results for the free  $^{131}\text{I}$ -PARPi-01 in human serum are in line with the data reported in the literature for similar cases. For instance, Zmuda and colleagues also investigated the stability of  $^{123}\text{I}$ -5 (with analog chemical structure as  $^{131}\text{I}$ -PARPi-01) and found that 98 % remained intact after incubation in mouse plasma for 20 h at 37 °C [197]. Similarly, Salinas and colleagues evaluated the stability of a chemically identical compound and reported no decrease in stability in mouse whole blood after 120 minutes of incubation at 37 °C [198].

Our data show that more than 96 % of the free tracer remained intact after 4 h and more than 91 % after 24 h. The consistency between the different studies indicates an apparent good stability of  $^{131}\text{I}$ -PARPi-01. Yet, the already observed instability within the *in vivo* studies of Sankaranarayanan and colleagues [79] for the same compound outlines the limitations of such *in vitro* tests to accurately evaluate the *in vivo* stability of radiotracers.

## Results and Discussion

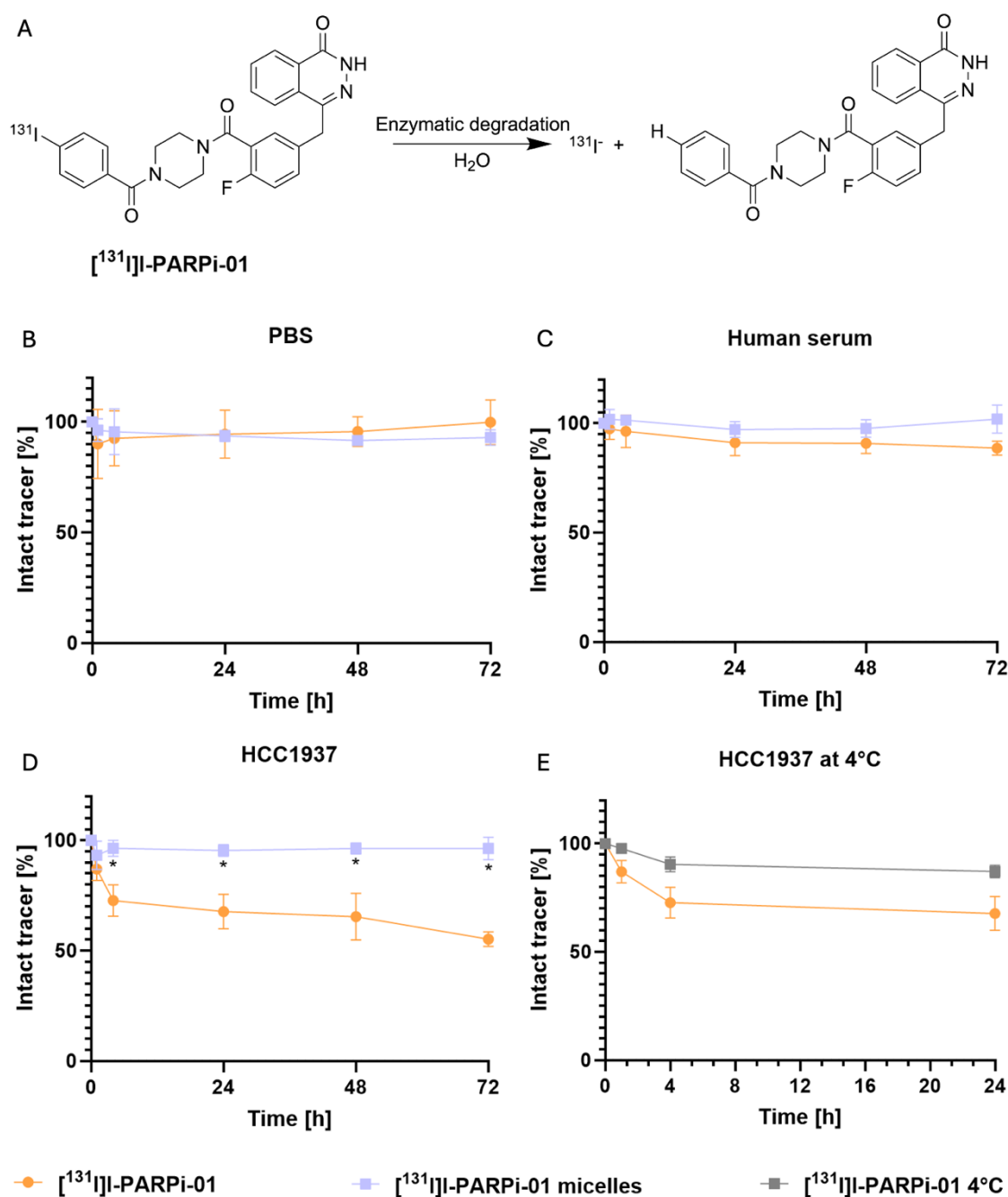


**Figure 12. Enzymatic degradation of radiotracer.** (A) Scheme of the chemical deiodination reaction during the enzymatic cleavage of  $^{131}\text{I}$ iodide from  $[^{131}\text{I}]\text{-PARPi-01}$ . (B-E) Detection of intact  $[^{131}\text{I}]\text{-PARPi-01}$  (2 MBq free  $[^{131}\text{I}]\text{-PARPi-01}$  vs. 2 MBq  $[^{131}\text{I}]\text{-PARPi-01}$  encapsulated in single-loaded polymeric micelles) via radio-HPLC incubated with (B) PBS at 37°C (pH 7.4), (C) human serum at 37°C (pH 7.4), (D) TNBC cell line HCC1937 at 37°C, (E) TNBC cell line HCC1937 at 37°C and 4°C. Values represent average  $\pm$  SD (n=3). Multiple unpaired t tests, \* < 0.01.

To further investigate this phenomenon, we conducted studies to evaluate the stability of the tracer when incubated in presence with the BRCA<sup>mut</sup> TNBC cell line HCC1937 at 37 °C

## Results and Discussion

(Figure 12D). Notably, after just 4 h of incubation, significant differences were observed between the free tracer and the tracer encapsulated in micelles, with 72 % of the free tracer remaining intact compared to 96 % of the encapsulated tracer. After 72 h of incubation, only 55 % ( $\pm 3.3$  %) of the free tracer remained intact, whereas over 96 % of the encapsulated tracer retained its integrity, indicating an 11-fold increase in tracer stability.

Considering the stability results of the tracer in relation to their uptake (Figure 11B), it is evident that a difference of approximately 6 % in tracer stability—comparing the 93 % intact tracer encapsulated in micelles to the 87 % intact free tracer after one hour of incubation with HCC1937 cells—correlates closely with the 6 % increase in uptake when the tracer is encapsulated in micelles for 1h in the same cell line.

Incubating the free tracer for 24 h at 4 °C with HCC1937 cells (Figure 12E) further confirmed the hypothesis that the degradation process is driven by metabolic activity. By decreasing the temperature, the metabolic activity of enzymes decreases. This reduction in temperature can lead to slower reaction rates, as enzyme kinetics are influenced by temperature; lower temperatures typically result in decreased molecular motion and, consequently, reduced enzyme-substrate interactions [199]. After 24 h at 4 °C, more than 87 % of the free tracer remained intact, in contrast to only 67 % of the tracer that remained intact after 24 h at 37 °C (Figure 12E). This difference highlights that the degradation of the tracer is closely linked to the metabolic activity of the cells. In conclusion, the encapsulation of the tracer within polymeric micelles provides a protective barrier against enzymatic degradation, a phenomenon that has been also shown in other studies [200].

### 3.2.3 Synergistic Cytotoxicity of I-PARPi-01 and [<sup>125</sup>I]I-PARPi-01 *in vitro*

#### 3.2.3.1 Cytotoxic Assessment of I-PARPi-01

To evaluate the sensitivity of the cell lines described in Table 5 to the non-radioactive compound I-PARPi-01, 2D *in vitro* studies were performed. Cells were incubated for 72 h with varying concentrations of I-PARPi-01, ranging from 0  $\mu$ M to 200  $\mu$ M. The metabolic viability of the cells was subsequently analyzed using the XTT assay (Figure 13). The half-

## Results and Discussion

maximal inhibitory concentration ( $IC_{50}$ ) of I-PARPi-01 was determined, which reflects the concentration of a drug or compound needed to inhibit a specific biological or biochemical process by 50 % [201].

The results indicated that the BRCA<sup>mut</sup> TNBC cell line exhibited the highest  $IC_{50}$  value of 37  $\mu$ M (Figure 13), suggesting a lowered sensitivity to I-PARPi-01. This was followed by the BRCA<sup>wt</sup> TNBC cell line MDA-MB-231, which had an  $IC_{50}$  of 23.5  $\mu$ M (Figure 13). In contrast, the non-tumorigenic breast cell line MCF10A showed an  $IC_{50}$  of 7  $\mu$ M (Figure 13), indicating higher sensitivity to the compound. Lastly, the BRCA<sup>wt</sup> TNBC cell line MDA-MB-468 registered the lowest  $IC_{50}$  of 3.7  $\mu$ M (Figure 13), demonstrating the highest sensitivity to I-PARPi-01 among the tested cell lines.

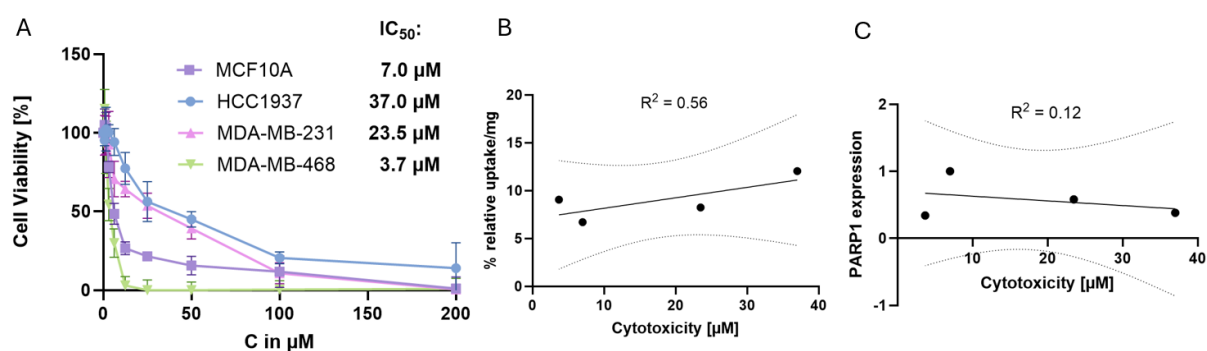


**Figure 13. Cell viability assessment of I-PARPi-01 treated breast cancer and non-tumorigenic cell lines. (A)** Cell viability assessment in I-PARPi-01 treated HCC1937, MDA-MB-468, MDA-MB-231, and MCF10A cell lines. Exponentially growing cells were seeded at a density of  $5 \times 10^3$  cells per well, and after a 72-hour incubation at 37°C, metabolic activity was evaluated using the XTT assay through absorbance measurements. Data are presented as mean  $\pm$  SD (n=3). Correlation of cytotoxicity ( $IC_{50}$  values) with **(B)** relative  $[^{131}I]$ I-PARPi-01 uptake and **(C)** relative PARP1 expression. Dotted lines indicating 95% confidence intervals.

These findings suggest a differential response to I-PARPi-01 compared to the genetic background and HR proficiency of the cell lines (Table 5), which may have implications for therapeutic strategies targeting PARP in breast cancer.

The HR status of the different cell lines cannot be directly correlated with the cytotoxic effect of I-PARPi-01. Interestingly, sensitivity to I-PARPi-01 appears to increase with higher HR rates, which contrasts with current literature [58, 59]. Moreover, recent studies claim that resistance to PARPi can arise, among other reasons, due to the restoration of HR mechanisms [202]. For instance, MDA-MB-468 cells, which exhibit the highest HR rate (as shown in Table 5), also demonstrate the highest sensitivity to I-PARPi-01, indicated by the lowest  $IC_{50}$  value within this panel. Conversely, HCC1937 cells, which are deficient in HR, show the highest  $IC_{50}$  value, suggesting a decreased sensitivity to this PARPi. Additionally,

## Results and Discussion

in the literature the parent compound olaparib demonstrates an  $IC_{50}$  value of approximately 78  $\mu$ M in the HCC1937 cell line after a 72h incubation period suggesting that this cell line is resistant to olaparib inhibition [203, 204].

Supporting our findings, Keung and colleagues have reported that the response of breast cancer cells to PARPi is not solely dependent on BRCA status [204]. These findings challenge the assumption that high HR activity is a contributing factor to PARP resistance [202].

Interestingly, when comparing the cell uptake of the free [ $^{131}$ I]I-PARPi-01 (Figure 11B) with the cytotoxicity of I-PARPi-01, a decent correlation can be established with an  $R^2$  value of 0.56 (Figure 13B). The HCC1937 cell line, which exhibits the highest uptake of the tracer, demonstrates the lowest sensitivity to I-PARPi-01. In contrast, MDA-MB-468 cells, which show the highest sensitivity to the compound, have the second highest uptake. It is also noteworthy that the tracer uptake among the different cell lines did not reveal statistically significant differences. This decent correlation between tracer uptake and cytotoxic response further complicates our understanding of the mechanisms driving sensitivity to I-PARPi-01 and suggests that factors beyond mere uptake may influence the therapeutic efficacy of this compound.

Furthermore, the sensitivity to I-PARPi-01 does not exhibit a correlation ( $R^2 = 0.12$ ) with PARP1 expression levels in the examined cell lines (Figure 13C). Notably, MCF10A cells, which display the highest PARP1 expression, demonstrate significant sensitivity to I-PARPi-01. Conversely, MDA-MB-468 cells, characterized by the lowest PARP1 expression, show the greatest sensitivity to this compound. These findings reinforce our earlier assertion in chapter 3.2.1 that, contrary to existing literature [186-188], PARP1 expression levels do not serve as a reliable predictive marker for therapeutic response to PARPi.

The findings contrast with previous studies, such as those by Makvandi and colleagues, which suggest that sensitivity to other PARPis like Talazoparib and Olaparib is positively correlated with PARP1 expression [191]. It is noteworthy that resistant cell lines, such as HCC1937, were not included in analysis and are outlined.

## Results and Discussion

In conclusion, the findings highlight a complex relationship between HR rates and sensitivity to the novel PARPi I-PARPi-01. Contrary to current literature that link high HR activity to resistance against PARPi [58, 59], our results demonstrate that MDA-MB-468 cells, characterized by elevated HR rates, exhibit the highest sensitivity to I-PARPi-01. In contrast, the HCC1937 cell line, characterized by a deficiency in functional HR, displays increased resistance, as evidenced by its elevated IC<sub>50</sub> value.

Additionally, sensitivity to I-PARPi-01 cannot be correlated with PARP1 expression levels and only fairly correlated to the uptake of [<sup>125</sup>I]I-PARPi-01 in the examined cell lines. These observations challenge established paradigms and suggest that sensitivity to I-PARPi-01 may not solely depend on HR status, PARP1 expression, or tracer uptake.

### *3.2.3.2 Enhancing DNA Damage Effects of Combined I-PARPi-01 and [<sup>125</sup>I]I-PARPi-01 through Polymeric Micelles in Triple-Negative Breast Cancer*

During investigations of therapeutic strategies for TNBC, we specifically examined the efficacy of sublethal concentrations of I-PARPi-01 (37 µM according to its IC<sub>50</sub> value, see chapter 3.2.3.1) and its radio-labeled counterpart, [<sup>125</sup>I]I-PARPi-01 (100 kBq), utilizing two distinct delivery methods: a free drug formulation and a micelle-co-loaded formulation. The aim was to assess how these formulations influence the induction of DNA damage and the subsequent repair mechanisms in the HCC1937 TNBC cell line.

The central focus of this investigation is the assessment of DNA DSBs induced by these treatment modalities, as well as the inhibition of DNA repair pathways mediated by PARP1. Utilizing γ-H2AX antibody staining as a biomarker for DNA DSBs, the mean fluorescence intensity (MFI) in response to varying treatment durations (24, 48, and 72 h) has been measured quantitatively. The results are presented relative to control conditions. Additionally, the impact of micellar formulations on the delivery and efficacy of the therapeutic agents has been evaluated, providing insights into the potential advantages of this delivery system over traditional methods.

By elucidating the interplay between DNA damage and repair in TNBC cells treated with I-PARPi-01 and [<sup>125</sup>I]I-PARPi-01, this chapter aims to contribute to the understanding of how combinatorial approaches can harness the vulnerabilities of cancer cells, ultimately paving the way for more effective treatment strategies in this challenging subtype of

## Results and Discussion

breast cancer. The results presented in Figure 14 provide a comprehensive overview of our findings, highlighting the significance of these compounds in the context of enhancing therapeutic outcomes for patients with TNBC.

**Free drug formulation (Figure 14A):** In the first experimental approach, cells were treated with a free combination of I-PARPi-01 (37  $\mu$ M) and [ $^{125}$ I]I-PARPi-01 (100 kBq). The results indicated an increase in MFI of  $\gamma$ -H2AX staining across all evaluated time points (24, 48, and 72 h). Notably, the MFI values at 24 h and 48 h remained relatively low and similar (122 a.u.  $\pm$  63 and 144 a.u.  $\pm$  50, respectively), while a significant increase was observed at 72 h, reaching a peak of 446 a.u.  $\pm$  161.

This indicates that the free formulation effectively induces DNA damage in TNBC cells over time, a crucial step for initiating apoptotic pathways and inhibiting cancer cell proliferation. The relatively stable MFI values at 24 h and 48 h, followed by a significant spike at 72 h, may suggest a delayed response mechanism. This could indicate that the cells initially attempt to repair the damage, but as time progresses, the accumulation of unrepaired damage leads to a more pronounced DNA damage response, culminating in potential apoptosis.

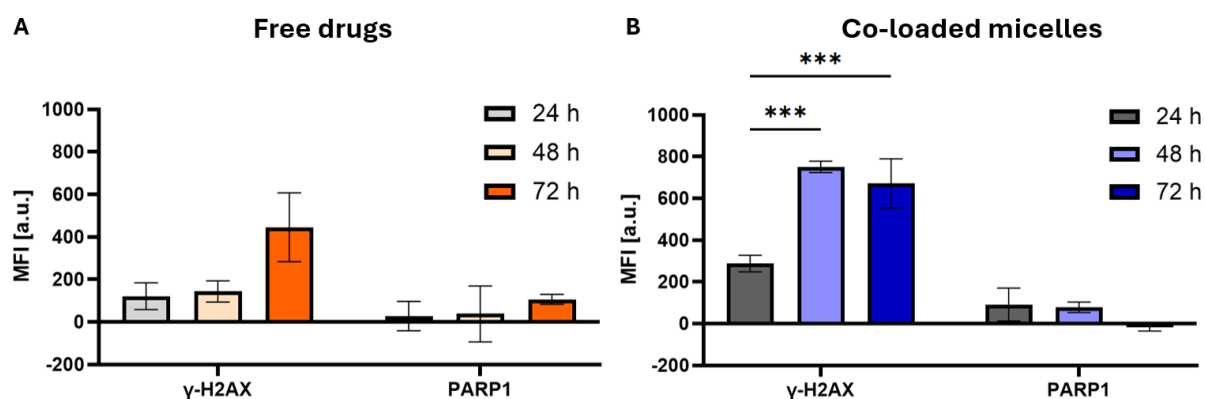


**Figure 14. Assessment of DNA damage in the HCC1937 TNBC cell line following treatment with combinations of I-PARPi-01 and [ $^{125}$ I]I-PARPi-01.** The analysis includes the measurement of mean fluorescence intensity (MFI) for DNA DSBs using  $\gamma$ -H2AX antibody staining, as well as evaluation of DNA repair through PARP1 antibody staining. Cells were incubated for 24, 48, and 72 hours with (A) a combination of I-PARPi-01 (37  $\mu$ M) and [ $^{125}$ I]I-PARPi-01 (100 kBq) in a free formulation, and (B) I-PARPi-01 (37  $\mu$ M) and [ $^{125}$ I]I-PARPi-01 (100 kBq) co-loaded in micelles (30 mg/mL). Results are presented as mean  $\pm$  SD (n=3) relative to control conditions, which were (A) 0.5% DMSO and (B) 2.5% unloaded micelles (30 mg/mL).

In terms of PARP1 expression, levels were generally low but showed a steady increase over the three time points, culminating in a maximum value of 107 a.u.  $\pm$  23 at 72 h.



## Results and Discussion

In general, the inhibition of PARP1 preserves energy, and keeps PARP1 at relatively normal levels, subsequently causing the generation of apoptosis in cancer cells which can be cleared by macrophages [205, 206].

PARP1 is also able to stimulate extracellular signal-regulated kinases, inducing survival of malignant cells [207]. The gradual increase in PARP1 levels, although low overall, suggests that the cells are engaging their repair mechanisms in response to DNA damage. Moreover, upregulation of PARP1 could be a contributing factor to treatment resistance and tumor recurrence [208].

Micelle-Co-Loaded Formulation (Figure 14B): In contrast, the second approach employed a micelle-co-encapsulated formulation of I-PARPi-01 and [<sup>125</sup>I]I-PARPi-01 (30 mg/mL). The micellar delivery system is designed to enhance the solubility and bioavailability of hydrophobic compounds, potentially improving their therapeutic efficacy. The analysis revealed that the micelle-co-loaded combination also led to an increase in  $\gamma$ -H2AX MFI, but the magnitude of DNA damage observed was notably higher than that of the free drug formulation at all time points assessed.

Already after 24 h, the  $\gamma$ -H2AX MFI in the micelle-co-loaded group was more than two times higher than that of the free formulation, measuring 288 a.u.  $\pm$  40 compared to 122 a.u.  $\pm$  63 for the free drug. This trend continued, with the maximum  $\gamma$ -H2AX MFI reaching 751 a.u.  $\pm$  27 after 48 h, indicating a significant induction of DNA damage. When comparing the 48 h MFI values, the micelle-co-loaded formulation (751 a.u.) exhibited a more than fivefold enhancement in cytotoxic effect compared to the free formulation group (144 a.u.).

Interestingly, there was a marginal, insignificant decrease to 672 a.u.  $\pm$  118 at 72 h. Regarding the dose-response-relationship the peak at 48 h (751 a.u.  $\pm$  27) followed by a slight decrease at 72 h may represent a threshold effect, suggesting that the cells may reach a saturation point in terms of DNA damage response.

The general enhancement in DNA damage could be attributed to more effective cellular uptake of the micelle-encapsulated drugs (Figure 11B), allowing for a more sustained release and prolonged interaction with target cells. This enhanced DNA damage suggests that the micellar delivery system enhances the bioavailability and efficacy of the drugs, leading to a more pronounced induction of DNA damage.

## Results and Discussion

In current literature, it is often highlighted that various drugs encapsulated in NCs exhibit enhanced cytotoxic effects compared to their free forms [140, 143, 148]. This could be attributed to the corresponding higher cellular uptake of drugs when encapsulated in NCs.

In terms of PARP1 expression, the levels observed in the micelle-co-loaded formulation exhibited a contrasting behavior compared to the free drug formulation. While the free formulation demonstrated a steady increase in PARP1 levels over the three time points, the micelle-co-loaded formulation showed a steady decrease. This trend culminated in a minimal value of  $-17 \text{ a.u.} \pm 19$  relative to the control at 72 h.

This decline could indicate that the extensive DNA damage induced by the micellar system overwhelms the repair capacity of the cells, leading to a downregulation of PARP1 as the cells enter apoptosis. The negative value ( $-17 \text{ a.u.} \pm 19$ ) at 72 h suggests a potential loss of PARP1 function or expression, which could further hinder the repair mechanisms. PARP1 modulates the cancer cellular life cycle via regulating cellular mitosis and cell death pathways, including apoptosis, necrosis, and necroptosis [209]. Since PARP1 expression decreases less extracellular signal-regulated kinases are stimulated, which are responsible for the survival of malignant cells [207]. Moreover, the inhibition of PARP1 disrupts the C-jun N-terminal kinase (JNK)–PARP1–JNK feedback loop. This disruption promotes apoptosis in cancer cells [207]. Generally, downregulating PARP1 can influence various factors involved in the cell cycle and apoptosis, thereby suppressing the proliferation of carcinomas. This has been demonstrated in studies using PARP $-/-$  mouse models as well as in human breast cancer cell lines, among others [210, 211].

In this study, we focused on the development and evaluation of a co-loaded NC system designed to enhance the delivery and efficacy of [ $^{125}\text{I}$ ]I-PARPi-01 and I-PARPi-01 formulation in treating TNBC. In conclusion, the micelle-co-loaded formulation demonstrated a significant improvement in drug delivery compared to the free formulation, as evidenced by the more than two-fold increase in MFI of  $\gamma\text{-H2AX}$  at 24 h post-treatment, and a remarkable fivefold enhancement at 48 h.

The sustained release profile of the micelle-co-loaded formulation (Figure 9D) as well as the improved tracer stability (Figure 12D) might contribute to the increased intracellular accumulation of the drug, leading to a more significant induction of DNA damage, as

## Results and Discussion

indicated by the elevated levels of  $\gamma$ -H2AX. This enhanced DNA damage response is crucial for overcoming the inherent resistance mechanisms seen in TNBC [212].

### 3.3 *In Vivo* Evaluation of PARP inhibitor-Loaded Micelles in TNBC Xenografts

#### 3.3.1 Biodistribution and Tumor Accumulation of [ $^{123}$ I]I-PARPi-01 in Polymeric Micelles

As detailed in chapter 1.2.3, Sankaranarayanan and colleagues previously examined the *in vivo* biodistribution of the free radiotracer [ $^{123}$ I]I-PARPi-01 [79]. Following iv administration of the radiotracer in nude mice bearing MDA-MB-231 cell-derived xenografts, SPECT/CT imaging was performed at 4 h and 24 h p.i. The imaging results at the 4h mark revealed significant radiotracer accumulation in the liver, gastrointestinal tract (including the small intestine, colon, and stomach), and thyroid (Figure 3A). In contrast, at the 24h time point, radiotracer uptake was predominantly observed in the liver and thyroid (Figure 3A), yielding tumor-to-blood and tumor-to-muscle ratios of 1.3 and 4.2, respectively (Figure 3B). [79]

The study conducted by Sankaranarayanan and colleagues highlights several limitations associated with the use of small molecule radiotracers [79]. Notably, the unfavorable biodistribution of the tracer within target organs poses a significant challenge. Additionally, the lipophilic characteristics of the molecule contribute to its binding to plasma proteins, particularly lipoproteins, which results in a less favorable tumor-to-blood ratio. Furthermore, the phenomenon of deiodination, wherein the radioactive iodine atom is cleaved from the tracer, is evidenced by the substantial accumulation of radioactivity in the thyroid gland, as reported in the findings of Sankaranarayanan et al. [79]. Collectively, these factors lead to a compromised therapeutic efficacy of the radiotracer.

In contrast, the accumulation of nanomedicine in tumors is primarily attributed to the EPR effect, a phenomenon first identified by Maeda and colleagues in solid murine tumors [103, 213]. Over the past 22 years, NCs designed to exploit the EPR effect have been utilized in clinical settings [214]. These NCs preferentially accumulate in tumor

## Results and Discussion

tissues due to the characteristics of tumor vasculature, which is typically leaky, combined with impaired lymphatic drainage. This unique combination—resulting from the chaotic architecture of blood vessels formed by rapidly growing tumors and the dysfunction of lymphatic systems—facilitates the passive accumulation of nanomedicine within the TME. [215]

This chapter explores the role of polymeric micelles as NCs in improving *in vivo* biodistribution, thereby enhancing their potential for radionuclide therapy. The micelles, co-loaded with the radiotracer and the non-radioactive analogue I-PARPi-01 were assessed for their *in vivo* performance against the free formulation of the mixed drugs (carrier-free) and the free radiotracer (free tracer). An overview of the formulations for the different groups is presented in Figure 15A. To evaluate the impact of tracer encapsulation in micelles on blood circulation time, tracer uptake, and tracer stability, co-loaded micelles were injected iv in HCC1937 BRCA<sup>mut</sup> xenograft-bearing immunocompromised mice. *In vivo* biodistribution was visualized using small animal SPECT/CT imaging, while *ex vivo* biodistribution was quantified through gamma counter measurements.

### 3.3.1.1 Enhancing Circulation Half-Life of [<sup>123</sup>I]I-PARPi-01 Using Polymeric Micelles

The different tracer formulations were synthesized as discussed in chapter 2.2.6.3 and 2.2.6.4 of this thesis. For the biodistribution studies, PARP-01 was radiolabeled with <sup>123</sup>I, enabling SPECT imaging. The physical half-life of approximately 13.2h for <sup>123</sup>I [216] facilitates the performance of multiple SPECT/CT scans in the same mouse following a single injection. Under isoflurane anesthesia, 12 NOD.SCID mice received an injection of 5 mL/kg body weight of the tracer via the lateral tail vein, adhering to GV-SOLAS guidelines. Each injection contained 15 ± 3 MBq of [<sup>123</sup>I]I-PARPi-01, which equals 750 MBq/kg body weight (n = 4). The injections for both the free drugs group and the micelle group additionally included 15 mg/kg body weight non-radioactive I-PARPi-01 (Figure 15A). SPECT/CT imaging was performed at 0.5h, 4h, and 24h p.i. The animals were euthanized 48h after the injection, and their organs were collected for radioactivity measurement using a gamma counter (Figure 15B).

## Results and Discussion

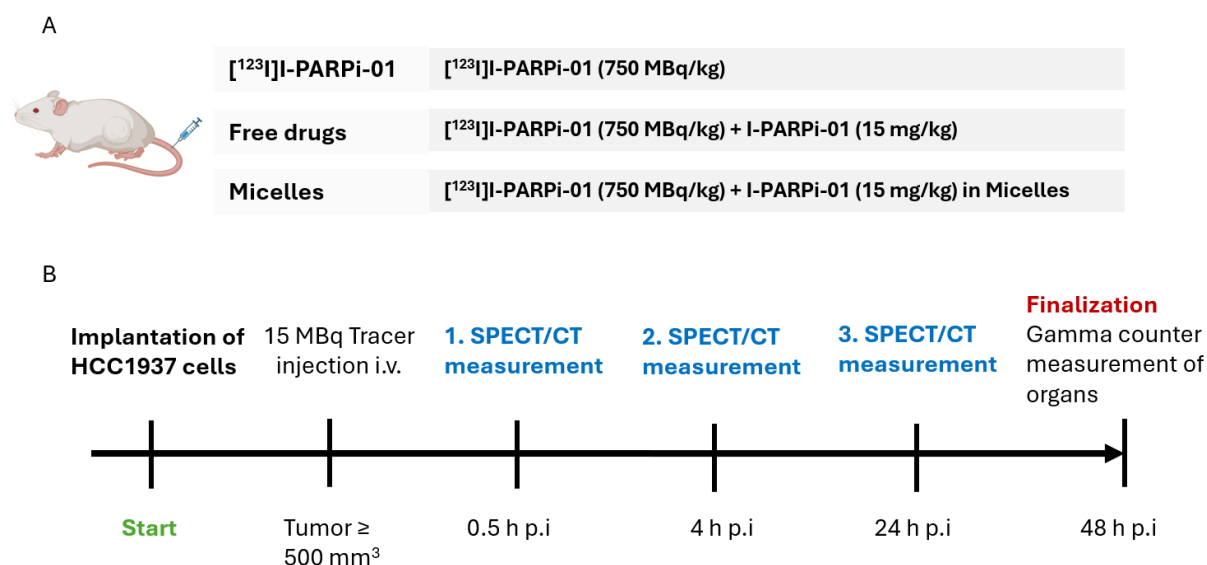


**Figure 15. In vivo biodistribution study setup.** The study was designed to assess the impact of various  $[^{123}\text{I}]\text{I-PARPi-01}$  formulations on blood circulation time and tumor accumulation. **(A)** A summary of the formulations used across the three different experimental groups. **(B)** A timeline outlining the study design: When the HCC1937 xenograft tumors reached a volume of  $500 \text{ mm}^3$ , a single intravenous (i.v.) dose of 750 MBq/kg body weight was administered to the mice while under anesthesia. SPECT/CT imaging was conducted at 0.5, 4, and 24 hours post-injection (p.i). Following the imaging sessions, the mice were euthanized, and organ samples were collected 48 hours after the injection and measured for radioactivity in the gamma counter.

Figure 16 presents representative SPECT maximum intensity projection (MIP) images obtained from a single mouse at three distinct time points: 0.5, 4, and 24 h p.i. The MIP images from both the free tracer group and the carrier-free group at the 0.5 h time point reveal significant tracer accumulation in the liver and gastrointestinal tract (including the small intestine, colon, and stomach). After 4 h the same groups show elevated tracer accumulation in the thyroid and gall bladder (Figure 16). By the 24 h p.i. mark, residual tracer retention was predominantly confined to the liver and thyroid in all treatment groups.

In contrast, the co-loaded micelles group showed enhanced blood circulation, as evidenced by the persistent radioactivity throughout the body at all assessed time points. Key organs with rich blood supply, such as the liver, lungs, and kidneys, exhibited increased tracer uptake after 0.5 h p.i. Notably, enhanced retention was particularly pronounced in the jugular veins and heart, confirming the prolonged circulation, with initial accumulation also observed in the spleen at the 4 h time point (Figure 16). Additionally, as for the other two groups, the micelle formulation also showed accumulation of radioactivity in the thyroid and gallbladder after 4 h, albeit less

## Results and Discussion

prominent. After 24 h, a significant amount of radioactivity remained detectable in the heart, indicating the sustained presence of the tracer in the blood pool, as well as common off-target organs for nanoparticles, such as liver and spleen [217, 218]. A prolonged circulation time significantly increases the likelihood of the NC accumulating at the tumor site through the EPR effect. In this context, the NC acts as a reservoir for the drug delivery system, maintaining drug availability until it reaches the targeted site. This principle is applicable to both non-targeted NCs and actively targeted NCs, as both types exploit the leaky endothelial vessels characteristic of tumors to extravasate into the tumor tissue [219]. Therefore, alongside the EPR effect, the stability and circulation half-life of the NC are equally essential for effective drug delivery [220].

Due to the high radioactivity present in the excretion organs, primarily stemming from radioactive feces within the gastrointestinal tract it becomes more challenging to detect the tumor signal in the MIP projections across all treatment groups (Figure 16). This elevated background signal can obscure the visualization of the tumor, complicating the interpretation of the imaging results and emphasizing the challenges associated with assessing tumor accumulation in the presence of significant tracer excretion in SPECT. An important point to address is the accumulation in the thyroid for the three groups. This can be attributed to the enzymatic deiodination of the tracer, as beforehand mentioned, and despite all three formulations suffer from some chemical degradation, the MIP images show the decreased intensity of the signal in the thyroid for the micelles as compared to the free drugs and NaCl control groups. The parent compound, Olaparib, is predominantly metabolized (approximately 84%) in the liver by cytochrome P450 (CYP450) enzymes, which are also known to deiodinate iodine-conjugated hydrocarbons. This oxidative metabolism is expected to be a key factor in the observed heavy deiodination of [<sup>123</sup>I] PARPi-01, resulting in a significant portion of the tracer being processed and cleared through these pathways [79, 221].

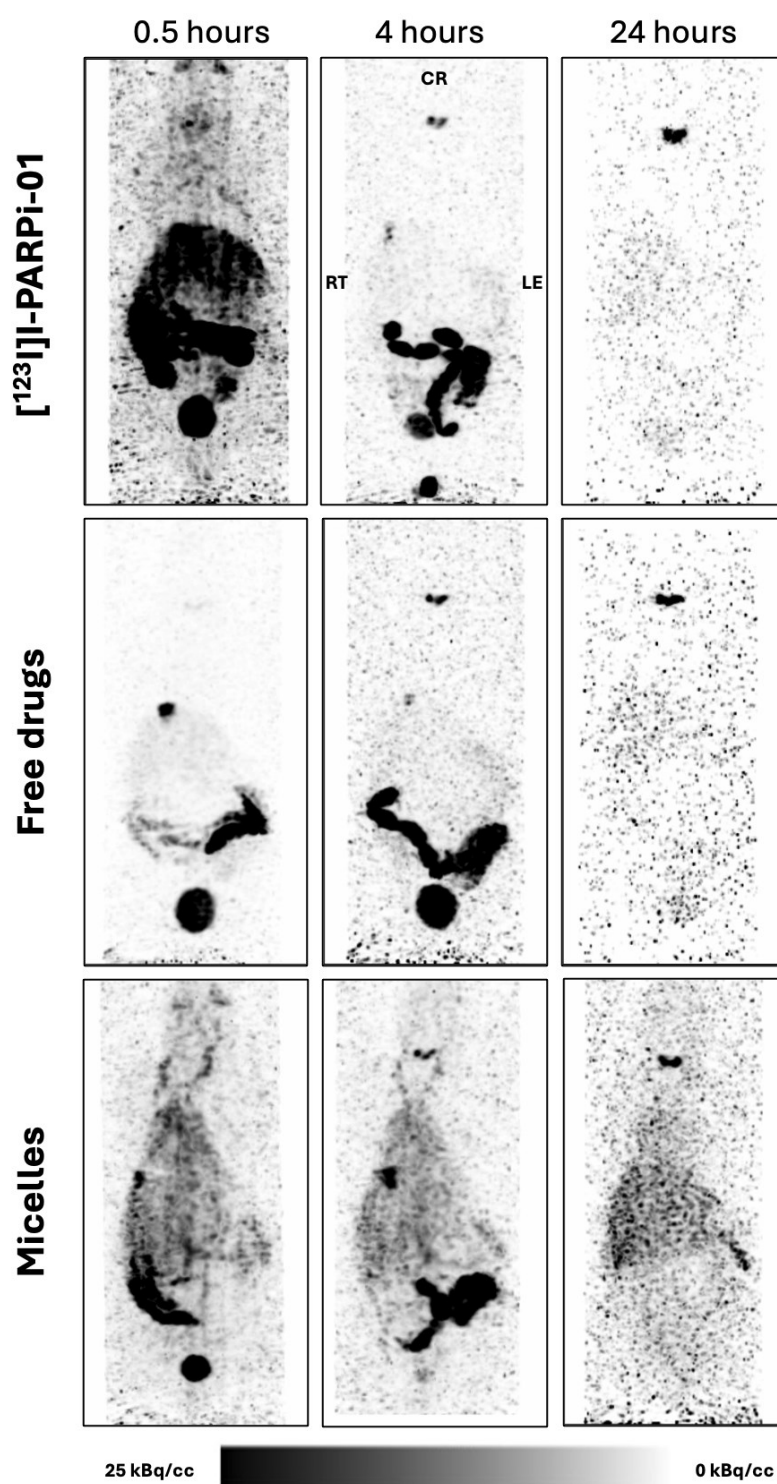


**Figure 16.** *In vivo* biodistribution of  $[^{123}\text{I}]\text{-PARPi-01}$  formulations. Representative Maximum intensity projection (MIP) images of *in vivo* SPECT/CT scans illustrate the biodistribution of different  $[^{123}\text{I}]\text{-PARPi-01}$  formulations administered intravenous in TNBC HCC1937 xenograft bearing mice at 0.5, 4, and 24 hours post-injection. The three tested formulations are: radioactive I-PARPi-01 (naked tracer group), radioactive and non-radioactive I-PARPi-01 co-administration (free drugs group) and I-PARPi-01 co-loaded micelles (micelles group). Enhanced circulation of  $[^{123}\text{I}]\text{-PARPi-01}$  and I-PARPi-01 co-loaded polymeric micelles is observed. RT: right, CR: cranial, LE: left.

## Results and Discussion

Additionally, the presence of free iodine in the thyroid at the therapeutic doses used is not expected to pose safety risks regarding DNA double-strand breaks. This is because the amounts of free iodine are anticipated to localize within the cytoplasm of thyroid cells after cellular uptake [222], not entering the nucleus. The distance between the Auger electron emitter and the DNA is too great to induce DNA double-strand breaks; however, there is a risk of generating free radicals, which could lead to irritations or damage [23]. Furthermore, the uptake of free radioactive iodine in human patients could be effectively blocked by administering a single dose of 130 mg of potassium iodide, providing protection for the thyroid for up to 24 h [223]. This approach could mitigate potential adverse effects associated with radioactive iodine exposure in therapeutic contexts.

Analyzing radiotracer accumulation in excretion organs, the SPECT MIP images reveal hepatic clearance as the main excretion pathway in all three treatment groups. The preferential hepatobiliary excretion of PARP-targeting radiotracers was already described in earlier studies [79, 198, 224]. Due to the lack of PARP1 overexpression in normal cells like hepatocytes in comparison to malignant cells, tracer retention in the liver is mainly due to its hepatobiliary excretion and not due to PARP1 specific binding [79]. The increased radioactivity observed in the gall bladder at 0.5 and 4 h p.i across all treatment groups suggests a delayed hepatic excretion of free  $^{123}\text{I}$  [225, 226]. The elevated activity in the urinary bladder at 0.5 h p.i, and particularly for the free radiotracer and the combination of the free drugs at 4 h p.i, emphasizes the distinct pharmacokinetics and clearance mechanisms between both free formulations of the radiotracer and the micellar encapsulated formulation. Residual [ $^{123}\text{I}$ ]I-PARPi-01 is being eliminated from the body through renal pathways. This renal excretion implies that these free radiotracer formulations are unstable *in vivo* and can be cleared via the kidneys, in contrast to the co-loaded micelles, which demonstrate reduced renal uptake.

The clearance of nanoparticles typically occurs through three primary mechanisms, namely renal excretion, hepatobiliary excretion, and uptake by the mononuclear phagocyte system (MPS), which strongly depend on the particle size [217, 218].

The co-loaded polymeric micelles, with a size of approximately 70 nm (Figure 7B), exceed the renal clearance threshold (i.e., 5-10 nm), thus preventing excretion through the kidneys [217]. Larger, non-degradable nanoparticles are more likely to be captured and



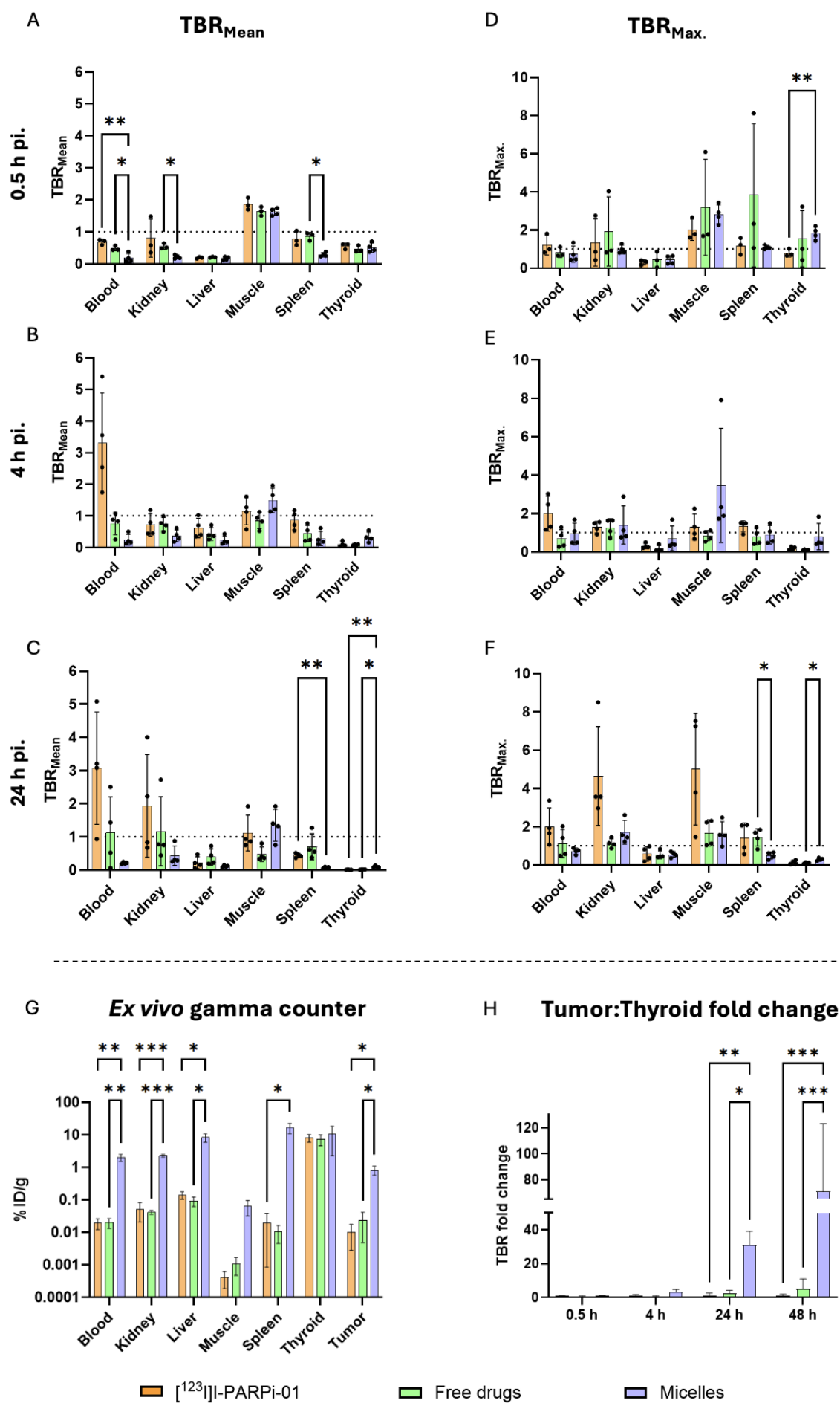
## Results and Discussion

retained in organs that contain phagocytic cells [218]. As NCs move from the peripheral circulation to the liver, their velocity decreases significantly, facilitating interactions with various liver cells and leading to their gradual clearance from the bloodstream [218, 227]. The concentration gradient along the sinusoid results in more NCs entering through the portal triad than exiting via the central vein, with macrophages in the liver exhibiting high uptakes due to their increased endocytic and phagocytic activity, while hepatocytes do not uptake nanomaterials due to their separation by fenestrated endothelial cells [227]. Fragments containing residual [ $^{123}\text{I}$ ]I-PARPi-01 may be excreted through both renal and hepatobiliary pathways.

To further understand the differences of the three formulations in a more quantitative manner, we calculated and plotted target-to-background ratios (TBR), illustrated in Figure 17. These provide quantitative evidence of the biodistribution, and clearance capabilities of the co-loaded micelles compared to the naked tracer and free drugs' groups. To determine  $\text{TBR}_{\text{Mean}}$  and  $\text{TBR}_{\text{Max}}$ , the tumor was defined as the target, while the corresponding organ served as the background reference.  $\text{TBR}_{\text{Mean}}$  assesses the average uptake across the entire target region (volume of interest), while  $\text{TBR}_{\text{Max}}$  highlights the maximum uptake observed within that region. Ratios exceeding 1, as denoted by the dotted line, indicate a greater accumulation of the radiotracer in the tumor relative to the background organ.

Throughout the study, the  $\text{TBR}_{\text{Mean}}$  for tumor-to-blood ratios demonstrated an increasing trend over time across all treatment groups (Figure 17A-C). Notably, the micelle formulation consistently exhibited  $\text{TBR}_{\text{Mean}}$  values below 0.5 at all time points, indicating a notable amount of circulating tracer in the blood pool compared to accumulated tracer in the tumor. In contrast, the free tracer [ $^{123}\text{I}$ ]I-PARPi-01 achieved the highest  $\text{TBR}_{\text{Mean}}$  values for the blood pool, exceeding a value of 3 at both the 4h and 24h p.i intervals (Figure 17C).

## Results and Discussion



## Results and Discussion

**Figure 17. Target-to-background ratios of different [ $^{123}\text{I}$ ]I-PARPi-01 formulations.** Mean (A-C) and maximum (D-F) TBR ( $\text{TBR}_{\text{Mean}}$  and  $\text{TBR}_{\text{Max}}$ ) evaluated in SPECT scans in HCC1937 xenograft-bearing mice, assessed at 0.5, 4, and 24 hours post-injection of free [ $^{123}\text{I}$ ]I-PARPi-01, free drugs (radioactive and non-radioactive I-PARPi-01 co-administration) and co-loaded micelles ( $n=4$ ). In this analysis, the tumor was designated as the target while the corresponding organ served as the background. Ratios greater than 1, as indicated by the dotted line, signify greater radiotracer accumulation in the tumor compared to the background organ. (G) *Ex vivo* gamma counter analysis of different organs conducted 48 hours p.i, expressed as percentage of injected dose per gram of tissue (% ID/g). (H) TBR fold change of tumor to thyroid over time. 0.5 – 24 h was calculated from  $\text{TBR}_{\text{Mean}}$  of the SPECT analysis; 48 h was calculated from gamma counter analysis. The free tracer group [ $^{123}\text{I}$ ]I-PARPi-01 was set as 1 for each time point. Data are presented as mean  $\pm$  SD ( $n \geq 3$ ). Statistical significance was determined using a two-way ANOVA with multiple comparisons (\*  $p < 0.05$ , \*\*  $p < 0.01$ , \*\*\*  $p < 0.001$ ).

The mean tumor-to-muscle ratio for the micelle formulation was  $1.35 (\pm 0.48)$ , compared to  $1.12 (\pm 0.54)$  for [ $^{123}\text{I}$ ]I-PARPi-01 and  $0.47 (\pm 0.22)$  for the free drugs formulation at the 24 h p.i mark (Figure 17C). These findings indicate that the micelle formulation facilitates effective PARP1-mediated uptake in the tumor, similar to the naked tracer formulation. The observed decrease in the  $\text{TBR}_{\text{Mean}}$  for the free drug group may be attributed to PARP blocking caused by the non-radioactive I-PARPi-01, which could hinder the binding and uptake of the radiolabeled tracer in the tumor tissue.

In comparison to the mean tumor-to-muscle ratio, the maximum tumor-to-muscle ratio observed at 24h p.i was achieved in the naked tracer group ( $5.00 \pm 2.91$ ). In contrast, both the carrier-free group and the micelle formulation exhibited similar tumor-to-muscle ratios ( $1.67 \pm 0.69$  and  $1.64 \pm 0.63$ , respectively). These findings further underscore the heterogeneous nature of the tumor.

Moreover, the  $\text{TBR}_{\text{Mean}}$  of the liver remains below 1 for all groups at every time point (Figure 17A-C). This indicates that the radiotracer quickly accumulates in the liver and persists there throughout the observation period, suggesting hepatic clearance of the tracer across all groups. This observation underlines the results obtained from the SPECT MIP imaging analysis (Figure 16).

Furthermore, the  $\text{TBR}_{\text{Mean}}$  of the thyroid demonstrates a decreasing trend over time across all treatment groups (Figure 17A-C). However, the micelle group shows a significantly higher  $\text{TBR}_{\text{Mean}}$  compared to both [ $^{123}\text{I}$ ]I-PARPi-01 ( $p < 0.01$ ) and the free drugs group ( $p < 0.05$ ) after 24 h, with an increase of 31-fold relative to [ $^{123}\text{I}$ ]I-PARPi-01 and an increase of 11-fold relative to the free drugs group (Figure 17H). This observation implies a reduced deiodination of the tracer and a higher uptake of the tracer in the tumor when encapsulated in the micelles, thereby highlighting the potential advantages of the formulation in enhancing tracer stability and target site retention.

## Results and Discussion

The observation that  $TBR_{Max}$  differs from  $TBR_{Mean}$  across most organs (tumor-to-background) can be attributed to several factors related to the nature of the measurements and the distribution of the radiotracer (Figure 17D-F).  $TBR_{Max}$  focuses on the peak accumulation of the tracer within the target area, providing insight into the highest level of tracer uptake. This measure can be particularly useful in identifying regions of intense activity within the target that may be indicative of higher biological activity (e.g., tumor metabolism). A  $TBR_{Max}$  value greater than 1 signifies that the highest concentration of the tracer in the target surpasses the highest concentration found in the background.

These hotspots could arise from varying biological activity within the tumor or organ, such as increased metabolism, receptor expression, blood flow, vascular permeability [228], or intra-tumoral distribution of tumor associated macrophages [229] leading to higher uptake in specific areas compared to the average across the entire region. The efficiency of nanomedicine in reaching the TME is not solely dependent on the EPR effect; it also hinges on several other critical factors, including the drug release mechanisms, and the circulation half-life of the formulation [230].

At 48 h p.i, the animals were sacrificed, the organs were harvested and the radioactivity analyzed using gamma counter analysis (Figure 17G). The results, corrected for the physical decay of the isotope, indicated that in both the free tracer group and the combination of the free drugs, the majority of the detected activity was accumulated in the thyroid ( $8.06 \pm 0.6$  %ID/g and  $7.25 \pm 2.7$  %ID/g, respectively), followed by significant less accumulation in other organs such as the liver ( $0.14 \pm 0.04$  %ID/g and  $0.09 \pm 0.03$  %ID/g, respectively) and kidneys ( $0.05 \pm 0.03$  %ID/g and  $0.04 \pm 0.001$  %ID/g, respectively). This preferential accumulation in the thyroid supports the findings from the TBR measurements (Figure 17A-F) and can be attributed to the instability of the tracer *in vivo* due to enzymatic deiodination. However, the micelle group shows after 48 h significantly higher TBR compared to both [ $^{123}$ I]-PARPi-01 ( $p < 0.001$ ) and the free drugs group ( $p < 0.001$ ), with an increase of 71-fold relative to [ $^{123}$ I]-PARPi-01 and an increase of 14-fold relative to the combination of the free drugs (Figure 17H). By analyzing the development of the TBR fold change from 4 h to 48 h, a constant increase can be observed.

## Results and Discussion

This trend suggests that the micelles significantly enhance tumor accumulation of the radiotracer as compared to the free drugs groups, without resulting in an increase in the levels of radiotracers in the thyroid, thereby improving the ratio between on-target (tumor) vs. off-target (thyroid) drug accumulation and showing promise for improved therapeutic outcomes.

Regarding off-target organs in the micelle group, the gamma counter data revealed that the majority of the detected radioactivity was localized in the spleen ( $16.66 \pm 5.88$  %ID/g), a well-known off-target organ for nanoparticle systems [217], followed by the thyroid ( $10.39 \pm 8.1$  %ID/g) and liver ( $8.29 \pm 2.4$  %ID/g), with very low accumulation in kidneys ( $2.28 \pm 0.2$  %ID/g). These high values in spleen and liver are consistent with the expected distribution patterns for nanoparticles [217, 218], as already discussed for the MIP images. The MPS, which includes the spleen and liver, plays a crucial role in filtering and clearing nanoparticles and other foreign substances from the bloodstream [217, 218].

Overall, the biodistribution studies of the different formulations of [ $^{123}$ I]I-PARPi-01 have yielded significant insights into the pharmacokinetics and clearance mechanisms of the radiotracer, highlighting the influence of formulation variations. The SPECT imaging revealed that while the free radiotracer and the combination of the free drugs exhibited significant initial accumulation in the liver and gastrointestinal tract, the co-loaded micelles demonstrated enhanced systemic circulation and reduced tracer instability. These differences in tracer accumulation and clearance underscore the critical role of formulation design in enhancing therapeutic strategies.

### *3.3.1.2 Enhancing Tumor Accumulation of [ $^{123}$ I]I-PARPi-01 Using Polymeric Micelles*

This chapter focuses on assessing the effect of polymeric micelles on tracer accumulation within the tumor. Analysis of the previously obtained SPECT/CT images taken at 0.5 h, 4 h, and 24 h p.i. for [ $^{123}$ I]I-PARPi-01, free drug formulation, and micelle formulation (n=4) (Figure 18A), revealed that there was no observable accumulation of the tracer in the tumor region across all treatment groups. By 24 h p.i., both the free tracer and free drug groups exhibited only minimal residual tracer activity overall. This indicates

## Results and Discussion

that these formulations were not retained effectively and were likely eliminated from the body without significant accumulation in the tumor area.

Importantly, the micelle formulation demonstrated enhanced tracer accumulation in the tumor area at the 24 h mark (Figure 18A), indicating that the polymeric micelles improve tumor accumulation of the  $[^{123}\text{I}]\text{-PARPi-01}$ , in line with the increased circulation time observed from the MIP images. The improved tumor accumulation can be attributed to the EPR effect, where the wider endothelial junctions and the leaky vasculature in tumors, combined with an impaired lymphatic drainage, allows for greater accumulation and retention of larger particles, such as our mPEG-b-p(HPMAm-Bz) micelles, as compared to free small molecules [103, 213].

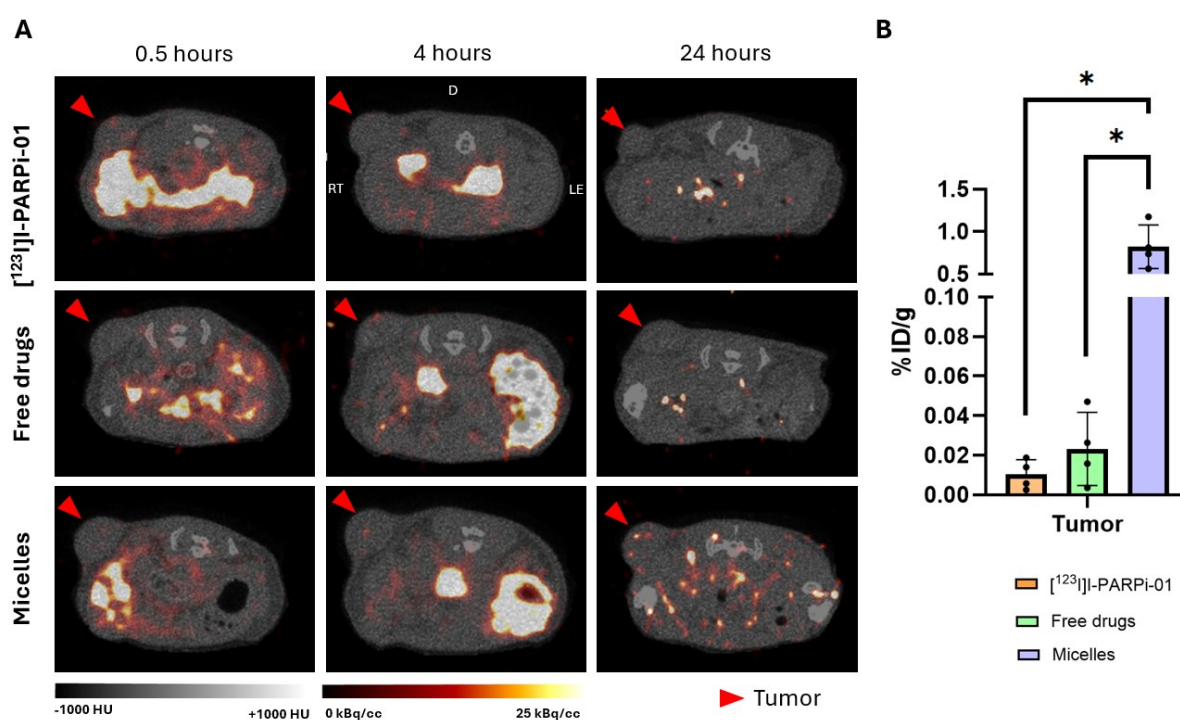


**Figure 18. Impact of different formulations of  $[^{123}\text{I}]\text{-PARPi-01}$  radiotracer on tumor accumulation. (A)** *In vivo* SPECT/CT imaging of various  $[^{123}\text{I}]\text{-PARPi-01}$  formulations administered intravenously to TNBC HCC1937 xenograft-bearing mice at 0.5, 4, and 24 hours post-injection (p.i). The tumor region is indicated by red arrow. Orientation is denoted as RT: right, D: dorsal, LE: left. **(B)** *Ex vivo* gamma counter analysis of tumor conducted 48 hours p.i, expressed as percentage of injected dose per gram of tissue (% ID/g). Data are presented as mean  $\pm$  SD ( $n \geq 3$ ). Statistical significance was assessed using a two-way ANOVA with multiple comparisons, with significance levels indicated as \* ( $p < 0.05$ ), \*\* ( $p < 0.01$ ), and \*\*\* ( $p < 0.001$ ).

In terms of tumor accumulation, the free tracer exhibited a radioactivity level of  $0.01 \pm 0.007$  %ID/g, while the free drugs combination showed an accumulation of  $0.02 \pm 0.01$  %ID/g (Figure 18B). These findings suggest that despite the high uptake in the thyroid and other organs, the overall accumulation of the radiotracer in the tumor remains

## Results and Discussion

relatively low. These results are consistent with the findings of Sankaranarayanan and colleagues, who reported a tumor accumulation of  $0.20 \pm 0.02$  %ID/g after 24h p.i. [79]. In contrast, the micelle formulation showed a significantly enhanced tracer accumulation of  $0.82 \pm 0.26$  %ID/g, representing an 80-fold increase compared to [ $^{123}\text{I}$ ]I-PARPi-01 and a 40-fold increase compared to the free drugs combination. This substantial improvement in tumor accumulation confirms the effectiveness of the micelles in promoting drug targeting to tumors, highlighting the potential for optimizing therapeutic efficacy through NC formulation. Supporting our findings, previous studies have shown that NCs effectively enhance the uptake of radiotracers across various tumor types [231, 232].

### 3.3.2 *In vivo* therapy study of [ $^{125}\text{I}$ ]I-PARPi-01 in Polymeric Micelles

Recent advances in radioligand therapy, particularly the use of radiolabeled PARPi like [ $^{125}\text{I}$ ]I-PARPi-01, have shown promise in targeting the unique vulnerabilities of BRCA<sup>mut</sup> TNBC. However, the efficacy of these therapies can be hindered by limitations such as poor solubility, rapid systemic clearance, and off-target effects [79].

Taking the previous findings together, the encapsulation of the Auger-emitting [ $^{125}\text{I}$ ]I-PARPi-01 together with the non-radioactive I-PARPi-01 in mPEG-*b*-p(HPMAm-Bz) polymeric micelles has shown promise for the treatment of BRCA<sup>mut</sup> TNBC. This chapter investigates the therapeutic performance of a [ $^{125}\text{I}$ ]I-PARPi-01 and I-PARPi-01 co-loaded polymeric micelle formulation in a xenograft mouse model of BRCA<sup>mut</sup> TNBC.

The *in vivo* efficacy of the various treatment strategies was assessed using immunocompromised mice bearing HCC1937 BRCA<sup>mut</sup> xenografts. The different tracer formulations were prepared as described in chapter 2.2.6 of this thesis. For the therapeutic study, PARP-01 was radiolabeled with the Auger electron-emitting  $^{125}\text{I}$  isotope (instead of the SPECT-isotope  $^{123}\text{I}$  used for the biodistribution) to facilitate the induction of DNA DSBs when positioned inside the nucleus (see chapter 1.1.1).

In our experimental design, we administered the co-loaded polymeric micelles and evaluated their efficacy against both the unencapsulated, free tracer [ $^{125}\text{I}$ ]I-PARPi-01 and a mixture of [ $^{125}\text{I}$ ]I-PARPi-01 and I-PARPi-01, which served as the free drugs formulation. Additionally, a control group received sodium chloride (Figure 19A). The treatment

## Results and Discussion

regimen consisted of three equal doses administered weekly of 1.5 GBq/kg body weight [ $^{125}\text{I}$ ]-PARPi-01 and 15 mg/kg body weight I-PARPi-01. Under isoflurane anesthesia, 4 NOD.SCID mice per treatment group received an injection of 5 mL/kg body weight of the tracer via the lateral tail vein, adhering to GV-SOLAS guidelines. Two weeks after the initial injection, the mice were euthanized, and fluorescently labeled lectins were injected iv while the mice were under anesthesia to mark the functional blood vessels (Figure 19B). The *in vivo* efficacy of the various treatment strategies was assessed using immunocompromised mice bearing HCC1937 BRCA<sup>mut</sup> xenografts.

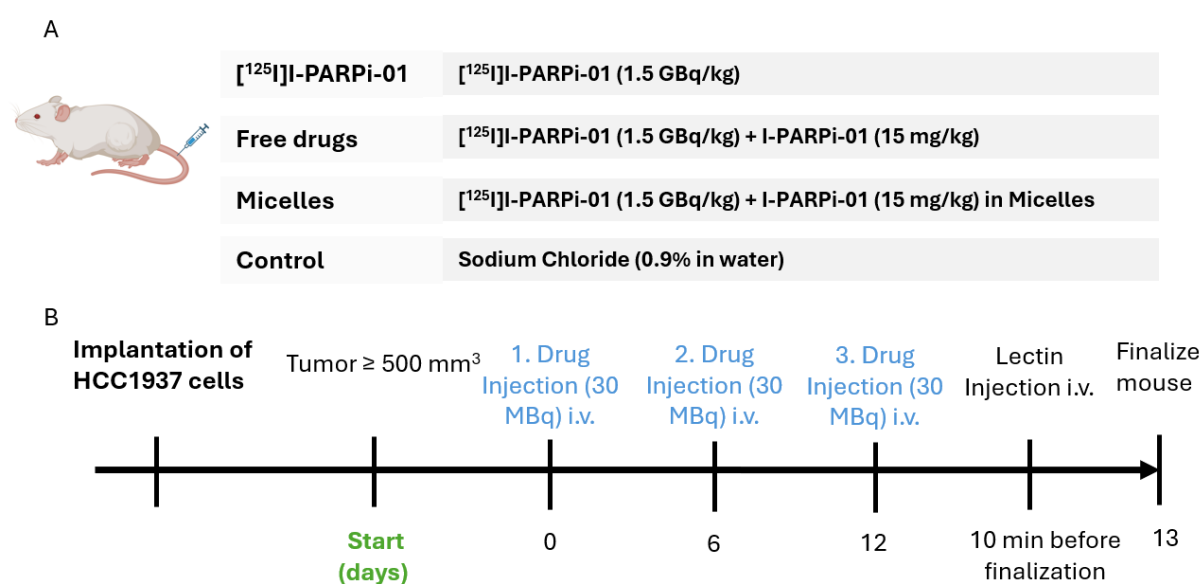


**Figure 19. Comprehensive overview of the *in vivo* therapy study conducted to evaluate the effects of various formulations of [ $^{125}\text{I}$ ]-PARPi-01.** Panel (A) provides a summary of the formulations utilized across the four distinct experimental groups. The timeline (B) illustrates the study design: Once the human HCC1937 subcutaneous implanted xenograft tumors reached a volume of  $500 \text{ mm}^3$ , mice received three intravenous (iv) injections of either 15 mg/kg body weight I-PARPi-01 and/or 1.5 GBq/kg bodyweight of the treatment or a control, administered weekly while under anesthesia. Following the treatment phase, the mice were injected iv fluorescently labeled lectins 10 minutes prior to euthanasia to label functional blood vessels. Subsequently, the mice were euthanized, and organ samples were harvested for analysis.

### 3.3.2.1 Co-Loaded Polymeric Micelles Induce Tumor Regression in Human TNBC Xenograft Model

The analysis of tumor volume across different treatment groups following the initiation of therapy indicated that both the free tracer and the free drugs formulation did not show significant differences in tumor growth compared to the saline control group ( $p > 0.05$ ) (Figure 20A-C,I). In contrast, the mice treated with the co-loaded micelles exhibited a marked decrease in tumor size starting just four days after drug administration (Figure



## Results and Discussion

20D,I). By eight days post-treatment, significant differences in tumor size were observed in the co-loaded micelles group compared to the control group, as well as to the free tracer and the carrier-free formulation ( $p < 0.05$ ). Thirteen days after the start of the therapy, tumors in the co-loaded micelles group had reduced their initial sizes to 50% ( $\pm 17$ ).

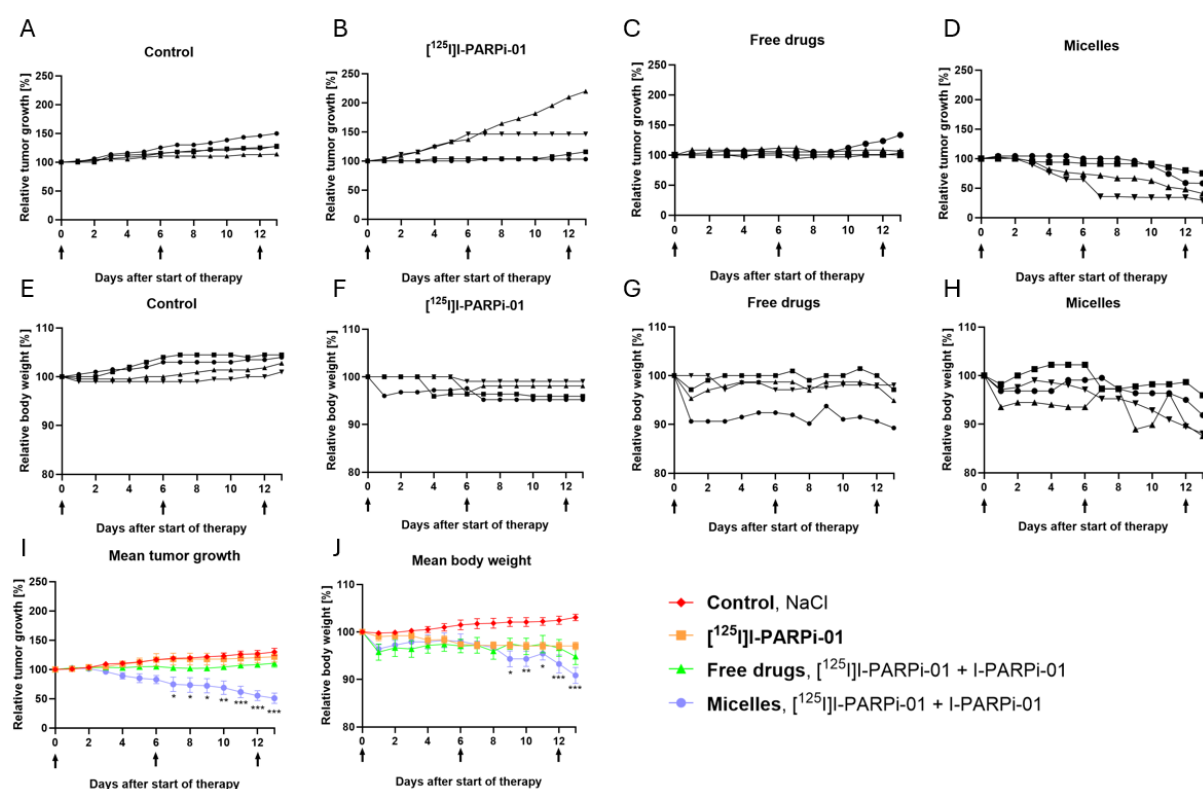


**Figure 20. Therapeutic efficacy of three injections with co-loaded micelles in HCC1937 BRCA<sup>mut</sup> xenograft models.** Treatment consisted of intravenous (iv) injections of NaCl, [<sup>125</sup>I]I-PARPi-01, free drugs consisting of [<sup>125</sup>I]I-PARPi-01 and I-PARPi-01, and micelles, co-loaded with [<sup>125</sup>I]I-PARPi-01 and I-PARPi-01. Arrows represent iv injections. (A-D) Relative tumor growth of each individual mouse. (E-H) Relative body weight of each individual mouse. (I) Mean relative tumor growth of all treatment groups. (J) Mean relative body weight of all treatment groups. Data are presented as mean  $\pm$  SD ( $n = 4$ ). Data were statistically analyzed by two-way ANOVA with Tukey's multiple comparisons test with significance levels indicated as \* ( $p < 0.05$ ), \*\* ( $p < 0.01$ ), and \*\*\* ( $p < 0.001$ ).

The analysis indicates that [<sup>125</sup>I]I-PARPi-01 and the free drugs formulation were ineffective in reducing tumor size and decelerating tumor growth compared to the control group. However, the co-loaded micelle formulation proved effective, showing a significant reduction in tumor volume within a relatively short timeframe. Previous studies by Shi and colleagues demonstrated that empty polymeric micelles composed of the same polymer exhibited no therapeutic effect on tumor cells, both *in vitro* and *in vivo* [140]. This underscores that the cytotoxic effect is derived from the therapeutic agents encapsulated within the micelles.

## Results and Discussion

In contrast, other therapeutic attempts utilizing radiolabeled PARPi have shown only a delay in tumor growth across various cancer types, but none have successfully achieved a decrease in tumor size to the degree we observed in this study [79, 81, 82].

A similar approach was undertaken by Zhang et al., who developed a polymeric nanoformulation of Talazoparib to evaluate its efficacy in treating TNBC. NanoTalazoparib was administered intravenously to BRCA<sup>mut</sup> mice and compared with free Talazoparib. The results showed a significant increase in the lifespan of the mice following the iv administration of NanoTalazoparib, leading to a 50% reduction in tumor volume compared to the original size. [142] Most research groups targeting other cancer types with PARP-encapsulated NCs have also explored combination therapies (see Table 4) and reported beneficial outcomes both *in vitro* [148, 149] and *in vivo* [144, 145].

In conclusion, the results of this study demonstrate the superior efficacy of [<sup>125</sup>I]-PARPi-01 and I-PARPi-01 co-encapsulated in polymeric micelles as compared to the co-administration in free form, which is in line also with the prolonged blood circulation and higher tumor accumulation observed for the co-loaded micelle formulation. Moreover, drug combination therapy remains a cornerstone of clinical oncology [233, 234], leveraging the simultaneous use of multiple drugs to achieve synergistic therapeutic effects [142, 148].

Monitoring mice body weight changes during treatment provides important insights into the adverse effect of the formulation and serve as a good measure for the and tolerability of the treatments, together with the visual assessment of the overall animal conditions and behavior.

The naked tracer largely maintained their initial weight throughout the therapy (Figure 20F,J). Conversely, the combination of the free drugs cohort experienced a slight weight loss over time (Figure 20G,J), although this change was not statistically significant when compared to the other groups ( $p > 0.05$ ). In contrast, the group treated with the co-loaded micelles demonstrated a significant decline in body weight, reaching a reduction of up to 10% ( $\pm 3.8$ ,  $p < 0.001$ ) thirteen days following the initiation of therapy (Figure 20H,J). Notably, in comparison to the group that received the combination of the free drugs, the co-loaded micelles group weighed approximately 4% ( $\pm 3.4$ ) less after thirteen days.

## Results and Discussion

The consistent increase in body weight in the saline control group suggests that the injection solution did not induce any adverse effects, supporting its role as a safe control. The maintenance of body weight indicates that the free tracer formulation did not cause significant side effects. This suggests that it might be well-tolerated by the subjects. This finding aligns with previous studies conducted by various research groups examining the therapeutic effects and tolerability of PARPi radiotracers [79, 81, 82].

Overall, while the slight weight loss in the free drugs group was not statistically significant, it may still suggest a potential level of toxicity or adverse effects associated with the treatment. This could be attributed to the non-radioactive I-PARPi-01, since the naked tracer group did not show any decrease in body weight, and/or the presence of Cremophor EL as solubilizing agent for the co-administration of the free drugs. It is important to note that Cremophor EL is not an inert vehicle; it can exert a variety of biological effects, some of which may have critical clinical implications leading to potential weight loss of the mice. Its use has been associated with severe anaphylactoid hypersensitivity reactions, hyperlipidemia, abnormal lipoprotein patterns, erythrocyte aggregation, and peripheral neuropathy [235]. As with any therapeutic approach, it is essential to consider the potential toxicities of PARPi, whether used alone or in combination with other agents. Common adverse effects of PARPi, such as nausea, vomiting, immunosuppression, and myelosuppression can pose serious challenges that need to be carefully managed [236].

Importantly, the notable decline in body weight (up to 10% after three injections) in the micelle group raises concerns regarding the tolerability of the formulation and suggests that while the co-loaded micelles have shown high efficacy in reducing tumor size, they could also eventually pose risks to the patients' overall health and well-being.

One potential explanation for the observed effects may be attributed to the prolonged circulation time of the micelles and the high retention of both radioactive and non-radioactive PARPi within them. This prolonged retention could lead to extended exposure of the body to radiation, potentially resulting in off-target organ damage.

Therefore, alongside the therapeutic study, the mice underwent whole-body radioactivity measurements following their initial therapeutic injection of either the free tracer [ $^{125}\text{I}$ ]-PARPi-01, the combination of the free drugs [ $^{125}\text{I}$ ]-PARPi-01 and I-PARPi-01, or the co-

## Results and Discussion

loaded micelles (Figure 21A). These measurements enabled the monitoring of the rate at which the different formulations are excreted and metabolized after administration. Understanding these clearance patterns is crucial for evaluating the effectiveness of the drugs in reaching the tumor site, their safety profiles, and the optimal frequency of administration.

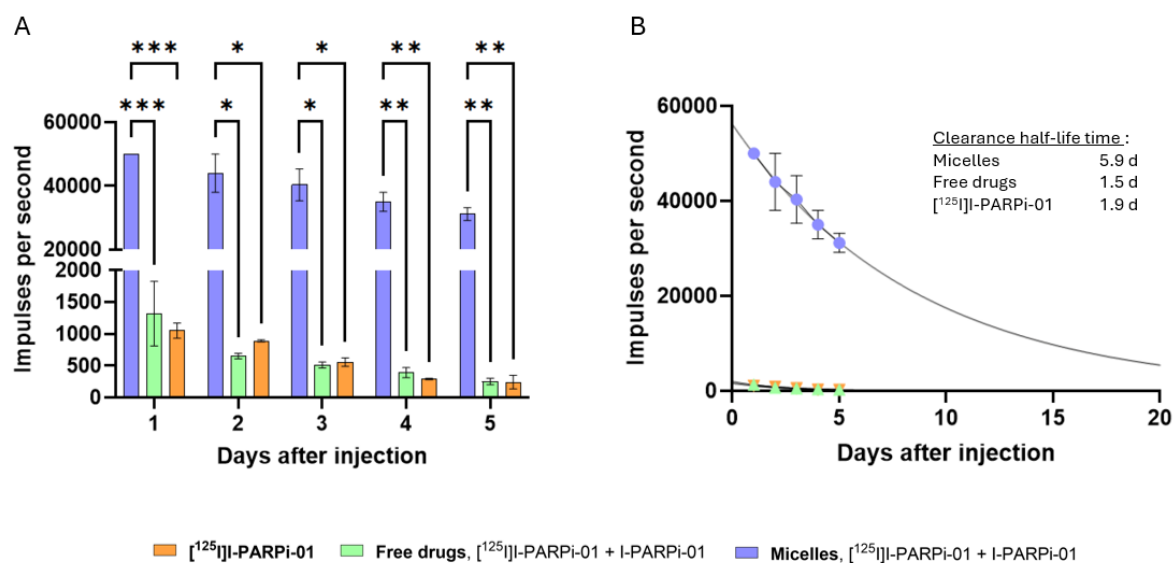


**Figure 21. Drug clearance *in vivo*.** (A) Half-lifetime corrected whole body radioactivity of mice determined with portable radiation detector after first intravenous injection in HCC1937 BRCA<sup>mut</sup> xenograft bearing mice. Detection limit: 50000 Impulses per second. Data are presented as mean  $\pm$  SD (n = 4). Data were statistically analyzed by two-way ANOVA with Tukey's multiple comparisons test with significance levels indicated as \* (p < 0.05), \*\* (p < 0.01), and \*\*\* (p < 0.001). (B) Nonlinear exponential one-phase regression curve to determine clearance half-life time of [<sup>125</sup>I]-PARPi-01 and I-PARPi-01.

The results demonstrated that over the five-day observation period, the retained radioactivity in the micelle group was significantly higher than in both the combination of the free drugs and free tracer groups. On the first day p.i, the whole-body radioactivity for the micelle group could not be accurately quantified, as the radiation detector was limited to measuring up to 50,000 impulses per second (ips). Any measurement exceeding this threshold was recorded as an overflow.

By day five p.i, the micelle group exhibited an approximate radioactivity of 31,000 ips ( $\pm$  2020), whereas the carrier-free group registered only 250 ips ( $\pm$  50), and the free tracer group showed 241 ips ( $\pm$  107). This indicates that the radioactivity in the micelle group was roughly 124 times greater than that of both the combination of the free drugs and the free tracer groups five days after administration. These findings underscore the effectiveness

## Results and Discussion

of the co-loaded micelles in enhancing the retention and circulation of the radiotracer, which may contribute to improved therapeutic outcomes.

Based on the data obtained from the whole-body radioactivity measurements, the radioactivity clearance pattern for each formulation was calculated (Figure 21B). The half-life of radioactivity clearance is a crucial pharmacokinetic parameter, as it reflects the duration required for the body to excrete half of the administered radioactivity.

In this study, the micelles demonstrated a significantly longer clearance half-life (5.9 days) compared to both the combination of the free drugs (1.5 days) and the free tracer (1.9 days). This prolonged retention time suggests that the micelles are more efficient at maintaining the presence of the radiotracer in the body. However, it remains unclear whether the observed radioactivity is due to the presence of intact encapsulated tracer or its metabolites. In contrast, the free tracer group demonstrated rapid metabolism and excretion of the free tracer.

These findings are consistent with previously generated biodistribution results, which also showed an enhanced blood circulation profile for the micelles and improved retention within the body (see chapter 3.3.1.1). This correlation reinforces the notion that encapsulating [ $^{125}$ I]-PARPi-01 within polymeric micelles not only improves the pharmacokinetics of the drug but also increases its potential therapeutic impact. The enhanced retention and circulation of the micelles can lead to better tumor targeting ultimately contributing to improved treatment outcomes for conditions like TNBC.

Conversely, this prolonged retention may also result in increased off-target effects. While the enhanced circulation time can improve therapeutic efficacy, it is crucial to carefully monitor and manage potential side effects associated with prolonged exposure to the drug and radioactivity, ensuring that the benefits of the treatment outweigh any adverse impacts on healthy tissues.

Taken together, the overall amount of radioactivity—and therefore also the non-radioactive PARPi—is significantly higher in the micelle group. This leads to extended exposure to both the radioactivity and the non-radioactive drug (-metabolites), which might cause unwanted side effects. One potential reason for this could be that the drug is retained too efficiently within the micelle, resulting in insufficient release. Additionally, interactions between the PARP molecule and the polymer of the micelle may induce

## Results and Discussion

chemical changes of the PARP molecule, altering excretion kinetics and leading to prolonged exposure to the radioactive iodine moiety within the body. Despite the *in vitro* drug release experiments showing no detectable metabolites in the radio HPLC analysis (Figure 9E), it is possible that chemical reactions occurring *in vivo* could lead to changes in the molecular structure.

### 3.3.2.2 Improving Off-Target Effects with Fewer Therapeutic Injections While Maintaining Therapeutic Efficacy

In the evolving landscape of oncology, the quest for more effective and patient-friendly treatment regimens is paramount. Traditional therapeutic approaches often require frequent injections, which can lead to patient discomfort, increased healthcare costs, and potential non-compliance due to the burdensome nature of treatment. As such, there is a growing interest in strategies that not only enhance the efficacy of cancer therapies but also minimize the frequency of administration.

By encapsulating [<sup>125</sup>I]-PARPi-01 and I-PARPi-01 within polymeric micelles, we have already demonstrated the potential to achieve significant tumor reduction *in vivo* (Figure 20I). This chapter will explore the impact of reduced injection frequency on treatment efficacy and off target effects. The balance between achieving therapeutic effectiveness and minimizing side effects will be analyzed.

Therefore, a second animal experiment has been performed, using the same tumor model (i.e., immunocompromised mice bearing HCC1937 BRCA<sup>mut</sup> xenografts), in which animals only received a single injection of the co-loaded micelles, in contrast to the three administrations they received in the previous experiment. The efficacy of the [<sup>125</sup>I]-PARPi-01 and I-PARPi-01 co-loaded micelle formulation was head-to-head compared with the co-administration of the free drugs. As for the previous therapy study, two weeks after treatment, the mice were euthanized, and fluorescently labeled lectins were injected iv while the mice were under anesthesia to mark the functional blood vessels.

The assessment of the relative tumor volume growth (Figure 22A-C), clearly demonstrates that the micelle group reduces tumor volume to 56% of its initial size after a single

## Results and Discussion

injection, achieving an efficacy comparable to that observed with three treatment injections in the previous study, which resulted in a reduction to 50% of its initial size. Notably, two out of four mice exhibited a strong response to the treatment, showing significant tumor regression (Figure 22B). One mouse displayed a slower but steady decrease in tumor volume, indicating a consistent therapeutic effect over time. However, it is important to note that one mouse experienced a rapid increase in tumor volume 11 days p.i, attributed to the development of a rapidly growing cyst.

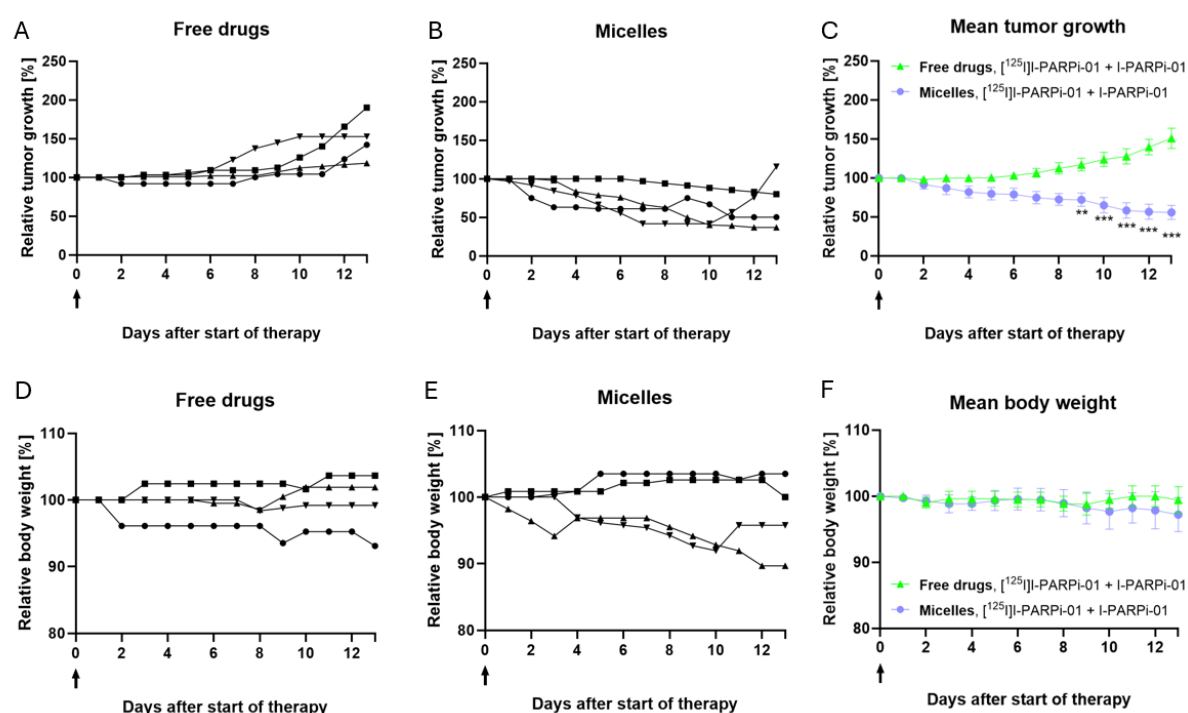


**Figure 22. Therapeutic efficacy of one injection with co-loaded micelles in HCC1937 BRCA<sup>mut</sup> xenograft models.** Treatment consisted of intravenous (iv) injections of a mixture of [<sup>125</sup>I]I-PARPi-01 and I-PARPi-01 as carrier free formulation, and micelles, co-loaded with [<sup>125</sup>I]I-PARPi-01 and I-PARPi-01. Arrow represents iv injection. **(A-B)** Relative tumor growth of each individual mouse. **(C)** Mean relative tumor growth of all treatment groups. **(D-E)** Relative body weight of each individual mouse. **(F)** Mean relative body weight of all treatment groups. Data are presented as mean  $\pm$  SD (n = 4). Statistical significance was assessed using a two-way ANOVA with multiple comparisons, with significance levels indicated as \*\* (p < 0.01), and \*\*\* (p < 0.001).

In contrast, all four animals receiving the free drugs exhibited continuous tumor growth throughout the treatment period (Figure 22A). In comparison to the three-injection regimen, the single injection demonstrated reduced efficacy within the combination of the free drugs treatment group. At the end of the initiation of therapy, the tumors in the combination of the free drugs cohort were approximately 110% of their initial size, as compared to the 150% growth compared to their size at treatment start. Notably, the

## Results and Discussion

differences in efficacy between the micelle group and the free drugs group began to reach statistical significance 9 days post-treatment ( $p < 0.01$ ).

This direct comparison of the free drugs with the drugs encapsulated in micelles underscores the advantages of drug encapsulation in nanoparticles. The prolonged circulation time (Figure 16) and retention of the drugs (Figure 21) within the micelles enable sustained therapeutic effects, allowing for high efficacy levels even after a single injection, akin to that of three injections with free drugs. This finding suggests that, in principle, lowering the dose for the micelle formulation would not hinder its efficacy. Furthermore, the findings align with existing literature that examines the administration of drug-loaded polymeric micelles, revealing a trend where multiple doses are often necessary for achieving significant therapeutic effects [127, 140, 174]. By reducing the frequency of injections without compromising efficacy, the micelle formulation could mitigate the adverse effects associated with frequent dosing, particularly weight changes, thereby improving the overall safety profile of the treatment.

Preclinical evaluation of breast cancer therapies have been shown to be strongly influenced by the initial tumor size [237]. Regarding the size, larger tumors often exhibit different biological behaviors compared to smaller tumors, which can affect how they respond to various treatment modalities. Specifically, larger tumors may have a more complex microenvironment, including increased hypoxia, necrosis, and a greater degree of heterogeneity in terms of cellular composition [238]. In numerous preclinical studies, including those investigating the efficacy of PARPi, treatment is typically initiated in tumors ranging from 100-200 mm<sup>3</sup> [77, 81, 144]. This size selection poses challenges for clinical correlation, as most patients present with advanced-stage or metastatic disease. In this study, the tumor size was set at 500 mm<sup>3</sup>, which is significantly larger than the conventional 100 mm<sup>3</sup> tumors used in other studies, including those focusing on PTX- and docetaxel-loaded polymeric micelles [127, 140, 174].

Despite the larger tumors, the outcomes for the co-loaded micelles were highly promising, as they achieved a reduction in tumor size, even with a more challenging starting point. These results indicate that effective therapeutic strategies can still yield positive outcomes, even in the face of significant challenges.



## Results and Discussion

In the assessment of body weight changes during the treatment period, no significant differences in body weight were observed between both treatment groups ( $p > 0.05$ ). Both groups largely maintained their initial weight throughout the therapy. For the micelle treatment, the body weight was preserved over the whole treatment course, while only experiencing a modest decrease in therapeutic efficacy of 6 %.

In comparison to the previous regimen that involved three injections of co-loaded micelles, a successful reduction in weight loss associated with treatment from 10 % to less than 3 % was achieved with a single therapeutic injection. This finding underscores the potential of optimizing treatment regimens to enhance patient safety and comfort without significantly compromising therapeutic outcomes.

In conclusion, this study highlights the potential of radioactive and non-radioactive I-PARPi-01 co-loaded polymeric micelles as a promising radio-chemotherapy combination strategy for treating BRCA<sup>mut</sup> TNBC. Upon a single injection, the co-loaded micelles demonstrated a significant reduction in tumor volume for at least two weeks, while maintaining acceptable safety profiles, as evidenced by the constant body weight. Taken together, the optimization of the treatment frequency (from three to one iv-injections) and formulation (from free drugs dissolved in cremophor to micelle co-loaded) not only enhances therapeutic efficacy but also contributes to future improvements in patient comfort and safety.

### 3.4 *Ex Vivo* Evaluation

The final chapter focuses on evaluating the mechanisms that contribute to the enhanced therapeutic efficacy of the nanoparticle formulations. This will be achieved through the analysis of ex vivo samples using various techniques, including histological staining (H&E), immunofluorescence staining, and micro autoradiography. Specifically, the micelles will be assessed regarding their accumulation and clearance behavior, as well as their cytotoxic potential in inducing DNA double-strand breaks within the tumor while minimizing effects on off-target organs. This comprehensive examination will provide crucial insights into the performance and safety profile of the targeted delivery system, offering a deeper understanding of its therapeutic advantages and potential limitations.

### 3.4.1 Micelle Therapy Induces Enhanced Cytotoxic Effects in TNBC

The therapeutic mechanism of action of PARPi and Auger electron emitters involves the induction of DNA double-strand breaks, which are critical for their cytotoxic effects on tumor cells [15, 65, 67]. To further validate our *in vivo* findings, we utilized tumor cryosections and conducted immunofluorescence staining for DNA double-strand breaks, specifically targeting  $\gamma$ -H2AX, a well-established marker for this type of damage [239].

Both therapeutic approaches—namely, the free formulation of the drugs and the co-loaded micelles—effectively induced DNA double-strand breaks in the tumor when compared to the control group ( $p < 0.001$  for both) (Figure 23A,B). Importantly, both treatments exhibited no cytotoxicity induction in the kidneys and liver (Figure 23A,B). However, the spleen exhibited enhanced DNA damage when treated with the co-loaded micelles, indicating a differential response in off-target organs (Figure 23A,B).

Interestingly, while both treatment groups elicited similar levels of DNA damage in the tumor, the free drug formulations did not affect tumor growth *in vivo* (Figure 22A,C). In contrast, the micelle-treated group exhibited a marked regression of the tumor (Figure 22B,C). One possible explanation for this discrepancy could be the restoration of homologous recombination repair mechanisms in tumor cells treated with free drugs, leading to resistance against the treatment [240]. This adaptive response may mitigate the therapeutic efficacy of the free formulations despite the initial DNA damage induced. Conversely, the targeted delivery provided by the micelles may enhance drug retention within the TME, resulting in sustained cytotoxic effects and improved overall treatment outcomes [152]. These findings are further supported by *in vitro* results presented in Chapter 3.2.3.2, which demonstrate that both formulations induce DNA double-strand breaks; however, only the micelle formulation effectively decreases the repair capacity, as evidenced by reduced PARP expression (Figure 14). This suggests that the micelles not only deliver the therapeutic agents more effectively but also impair the tumor's ability to repair the damage, ultimately leading to enhanced therapeutic efficacy.

## Results and Discussion

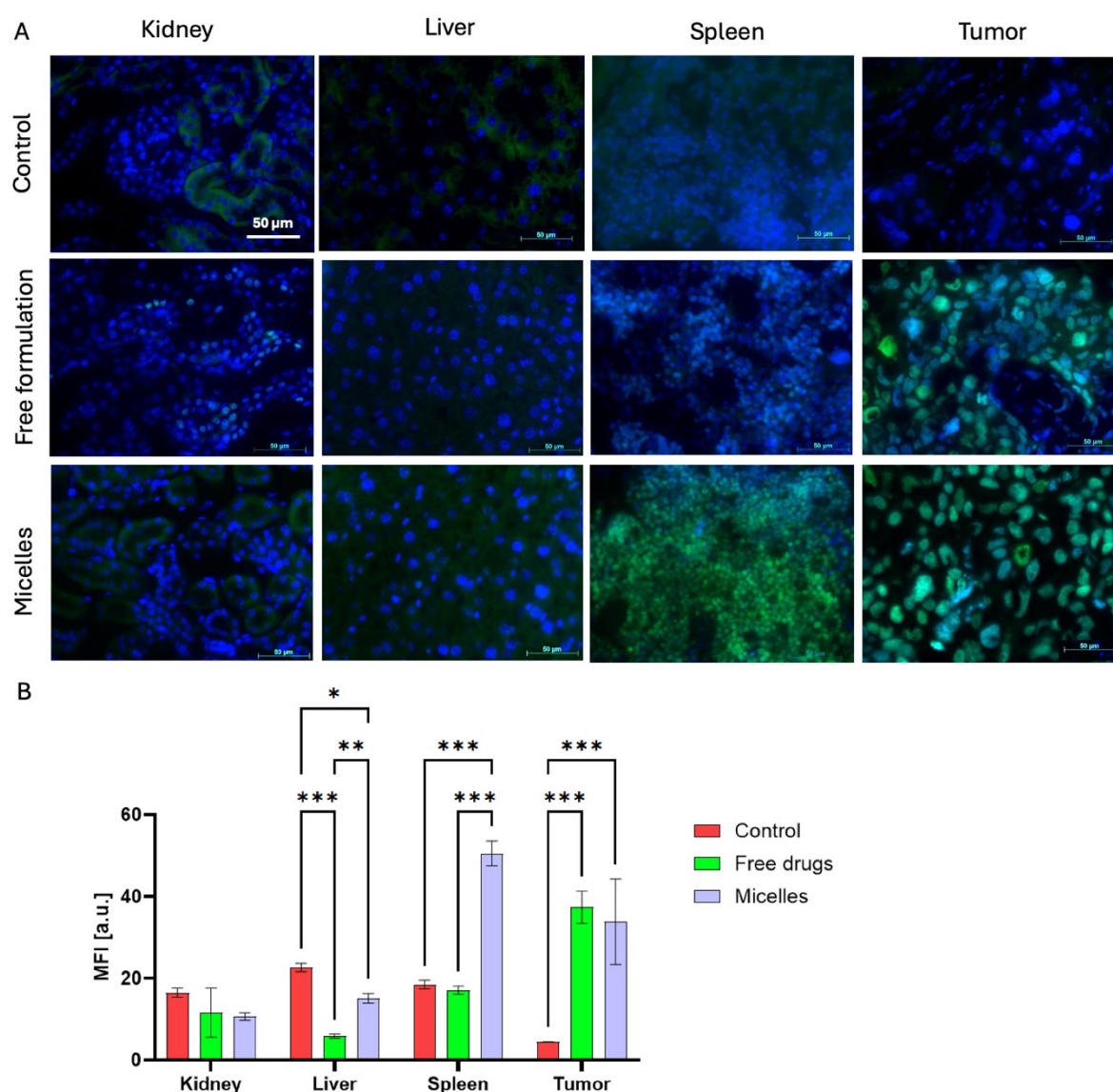


**Figure 23. Therapy-induced DNA damage evaluation of tumor and off-target organs. (A)** Representative fluorescence microscopy overlay images visualizing DNA damage in the control group and therapy groups receiving one therapeutic injection of the free formulation or co-loaded micelles. Nuclei were stained with dapi (blue), and DNA double-strand breaks were stained using  $\gamma$ -H2AX antibody (green). **(B)** Quantification of (A). Data were statistically analyzed by two-way ANOVA with Tukey's multiple comparisons test with significance levels indicated as \* ( $p < 0.05$ ), \*\* ( $p < 0.01$ ), and \*\*\* ( $p < 0.001$ ),  $n = 4$ .

The enhanced DNA damage in the spleen correlates with the pronounced accumulation of micelles in the spleen (Figure 16 and Figure 17) and can be explained by the nature of nanoparticles, which are taken up by macrophages in the spleen, facilitating their clearance [241, 242]. This finding implies that, although the PARPi predominantly targets tumor cells, interactions with immune cells in the spleen may induce localized cytotoxic effects. Consequently, further investigation in immunocompetent mouse models is warranted to comprehensively assess the implications of these interactions on the

## Results and Discussion

immune system. Overall, these findings highlight the potential for nanoparticle-based therapies to maximize tumor-specific effects while minimizing collateral damage to healthy tissues.

### 3.4.2 Interactions of Co-Loaded Micelles with the Tumor Microenvironment

A detailed visualization of the TME components that play a crucial role in the drug delivery process, specifically focusing on functional blood vessels, macrophages, and extracellular matrix helped to understand the mechanism behind the intratumorally micelle accumulation and retention.

Extravasation represents the initial step for NCs in circulation to access target tissues [243, 244]. Afterwards, nanoparticles exhibit generally varying distribution patterns across different organs, with the liver and spleen typically showing the greatest accumulation [242, 245]. However, pathological conditions, such as the altered vasculature found in tumors, can modify this distribution by allowing larger intercellular gaps that facilitate the exit of larger NCs from the blood vessels (EPR effect) [246]. Rhodamine-conjugated Ricinus communis agglutinin I (RCA I) is a specific marker that does not bind uniformly to the luminal surface of the endothelium, but instead binds preferentially to leaky sites in the endothelium of inflamed venules [247]. Moreover, RCA I demonstrates a preferential interaction with tumor-associated blood vessels [248], and with sinusoidal endothelial cells in the liver and bone marrow [249]. RCA I was injected iv 10 minutes before the mice were euthanized at the end of the therapy studies. This technique allows for the visualization of nascent vascular structures that exhibit increased permeability, which is often associated with tumor angiogenesis and other pathological conditions [103, 213, 220].

Within the TME, RCA I (red) exhibited more pronounced dot-like fluorescence, resulting in a yellow appearance when co-localized with the Cy7-fluorescently labeled polymer of the micelles (green) (Figure 24A). In contrast, the off-target organs exhibit reduced binding of RCA I, as expected, with the kidney displaying stronger background signals attributed to autofluorescence (Figure 24B). Consequently, there is no co-localization of micelles with areas of leaky blood vessels.

## Results and Discussion

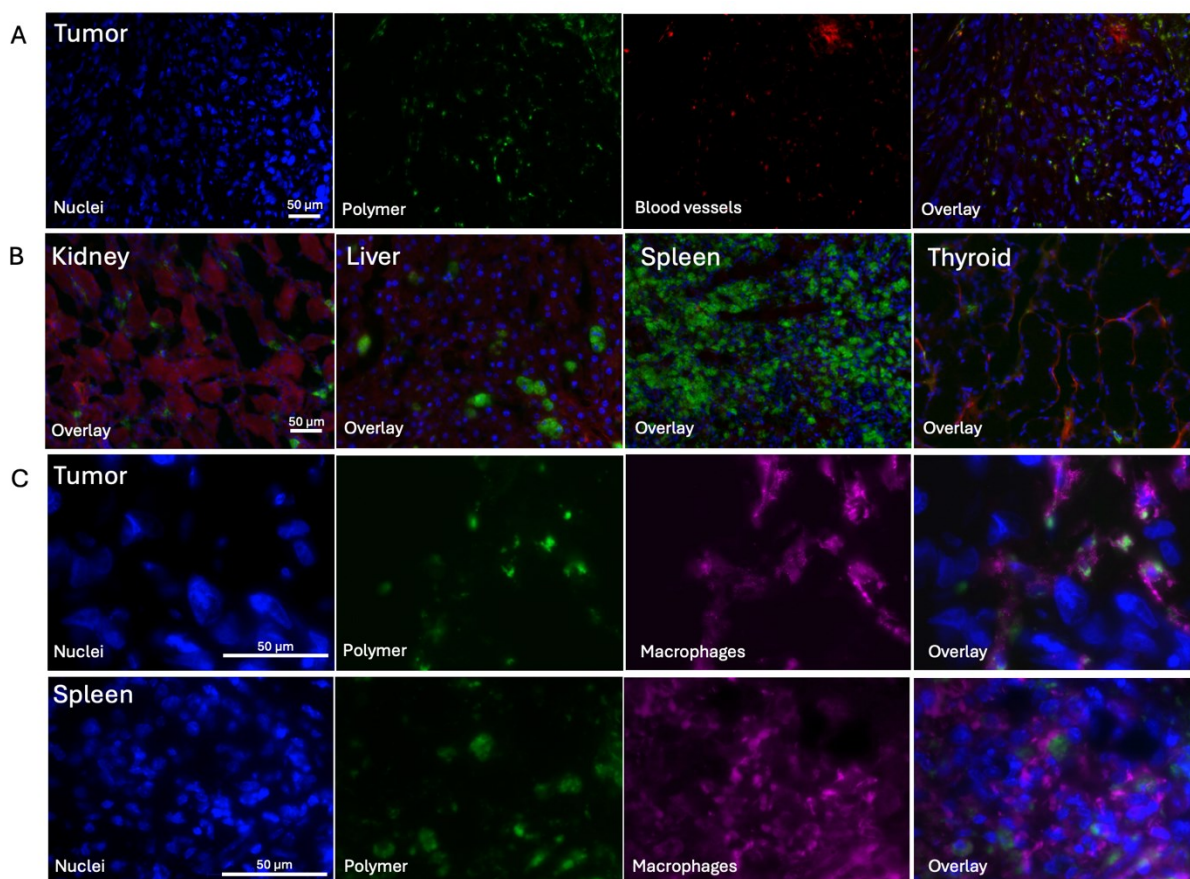


**Figure 24** *Ex vivo* co-localization of Cy7-labeled micelles with leaky blood vessels and macrophages. Representative fluorescence microscopy images of various organs following *in vivo* treatment with co-loaded polymeric micelles (green). Nuclei were counterstained using Dapi (blue) (scale bar = 50  $\mu$ m). **(A)** HCC1937 TNBC xenograft, and **(B)** off-target organs demonstrate co-localization with functional blood vessels visualized using fluorescently labeled lectins (red). **(C)** Tumor and Spleen demonstrate co-localization of micelles with macrophages stained using F4/80 antibody (magenta).

Regarding micelle accumulation, the kidneys demonstrate only minimal uptake of the micelles, aligning with the findings from the biodistribution studies where only negligible levels of radioactivity were detected in this organ (see chapter 3.3.1.1). This can be attributed to the size of the micelles, which is 70 nm — larger than the typical threshold for renal clearance [217]. As a result, it is likely that the minimal signals detected in the kidneys are not from intact micelles but rather from smaller polymer fragments that have degraded from the original micelles.

While the thyroid gland shows a notable increase in radioactivity uptake within the biodistribution analysis (Figure 16), the histological examination reveals very few detectable micelles in this organ (Figure 24B). This observation reinforces the established understanding that the free radioactive iodine, which is cleaved from the radiotracer, is



## Results and Discussion

responsible for the radioactivity signal in the thyroid, rather than the co-encapsulated micelles.

Additionally, the polymer components of the micelles are primarily found to accumulate in the spleen, followed by the liver (Figure 24B), which can be explained by the nature of nanoparticles, which are taken up by macrophages in the spleen and liver, facilitating their clearance [241, 242], aligning with the results obtained in previous biodistribution experiments.

Therefore, immunofluorescence microscopy confirmed the uptake of micelles by macrophages (F4/80-positive cells) in the typical clearance organs for nanoparticles, specifically the liver and spleen, as well as within the tumor (Figure 24C). Macrophages are among the primary cells responsible for nanoparticle uptake [194, 195, 229], indicating that these immune cells play a critical role in mediating the therapeutic effects of the nanoparticle formulations in the tumor microenvironment. Furthermore, macrophages inside the tumor tissue have been recognized as reservoirs for nanoparticles that enhance the accumulation of NCs within solid tumors [250-252].

An imaging study was conducted to visualize the distribution of the radioactive [ $^{125}$ I]-PARPi-01 within tumor tissue (Figure 25). The autoradiogram serves as a specialized image that highlights the presence of radioactivity, utilizing a co-staining technique with H&E to offer insights into the tissue structure. The presence of black silver grains on the autoradiogram indicates regions of accumulated radioactivity.

In representative autoradiograms of the HCC1937 xenografts, following three injections of [ $^{125}$ I]-PARPi-01 and I-PARPi-01 co-encapsulated micelles, it was observed that the radioactivity was predominantly retained in the extracellular matrix (depicted in light pink) of the tumor (Figure 25). It is assumed that the silver grains represent the encapsulated radiotracer, as other studies have demonstrated similar accumulation patterns in the extracellular matrix of nanoparticles [253]. Furthermore, particles with diameters larger than the network space of the extracellular matrix are typically rejected, while smaller particles can effectively traverse the matrix barrier [254]. The spacing of 20-40 nm between collagen fibrils acts as a physical barrier, obstructing the migration of larger particles and facilitating the retention of appropriately sized micelles within the tumor

## Results and Discussion

microenvironment [255]. Therefore it is assumed that the visualized radioactivity is still encapsulated in the nanocarrier and not in its free form.

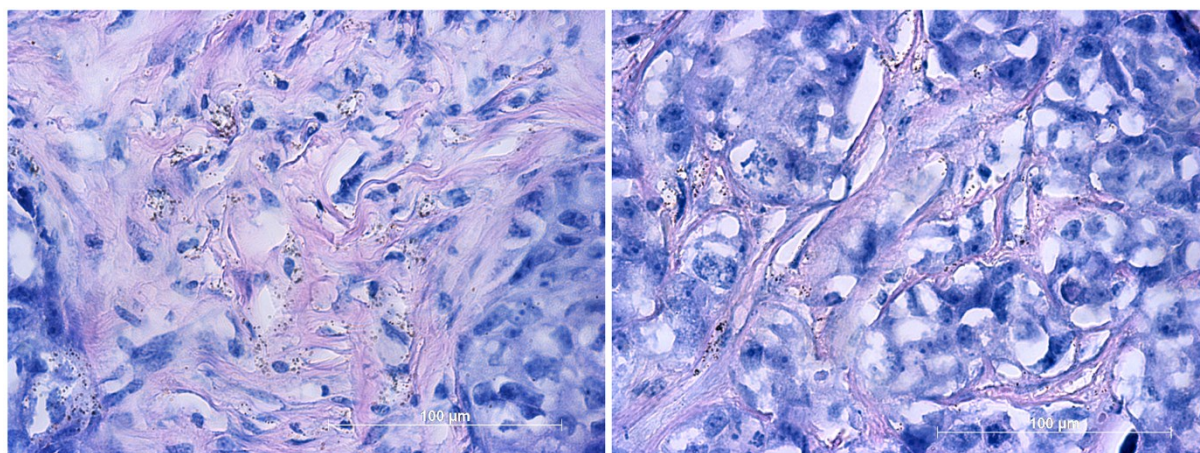


**Figure 25. Radiotracer is predominantly trapped in extra cellular matrix of the tumor.** Micro autoradiography of HCC1937 xenografts after micelle therapy, stained with H&E. Black silver grains indicate localisation of radioactivity ( $^{125}\text{I}$ iodine).

This dot-like distribution pattern of the micelles co-localized with leaky blood vessels (Figure 24A) can be explained by the basement membrane surrounding tumor vessels (Figure 25). After passing through the vascular endothelial gaps, NCs may become trapped in the subendothelial space due to the dense structure of the basement membrane, which could hinder their extravasation into the tumor tissue [256]. This entrapment may limit the therapeutic efficacy of the NCs by preventing them from effectively reaching and penetrating the tumor microenvironment [257].

However, autoradiograms indicate that radioactivity is also present in the cells adjacent to the extracellular matrix, specifically localized within the nuclei of these cells. This observation provides additional evidence that the radiotracer is successfully released from the micelles and subsequently taken up into the nucleus.

In conclusion, it has been demonstrated that nanoparticles facilitate several interactions with the tumor microenvironment, particularly through their co-localization with leaky blood vessels and subsequent predominantly entrapment in the extracellular matrix. The co-staining results with macrophages indicate that nanoparticles capable of overcoming the biological barrier of the extracellular matrix might be subsequently taken up by macrophages within the tumor. This interaction highlights the potential for macrophages to play a role in mediating the therapeutic effects of nanoparticle formulations in the TME.

## 4 Conclusions and Outlook

This PhD thesis presents the development of theranostic Auger electron-emitting polymeric micelle nanomedicines for radio-chemotherapy combination in TNBC. This formulation consists of a  $\pi$  electron-stabilized polymeric platform based on mPEG-*b*-p(HPMAm-Bz) polymers co-delivering both radioactive and non-radioactive PARPi (i.e., [ $^{125}$ I]I-PARPi-01 and I-PARPi-01, respectively) for improved treatment of BRCA<sup>mut</sup> TNBC. Based on the overall results, the following conclusions can be drawn:

1. A micelle formulation stably co-encapsulating both Auger electron-emitting [ $^{125}$ I]I-PARPi-01 and non-radioactive I-PARPi-01 therapeutics was prepared, showing homogeneous particle size and efficient retention for both PARPi drugs.
2. The polymeric micelles efficiently protected the drugs from enzymatic degradation for at least 72 h, enhanced cellular uptake *in vitro*, and induced increased cytotoxic effects in the HCC1937 cell line compared to the formulation of free drugs.
3. SPECT/CT imaging and quantification of the PARPi co-loaded micelles, using [ $^{123}$ I]I-PARPi-01, demonstrated that the micelle formulation displayed prolonged blood circulation time, improved *in vivo* tracer stability, and increased drug uptake in the tumor as compared to the co-administration of the free PARPi.
4. The co-loaded Auger electron-emitting [ $^{125}$ I]I-PARPi-01 and non-radioactive I-PARPi-01 micelle formulation demonstrated enhanced antitumor effects *in vivo* as compared to the co-administration of the free drugs. The co-loaded micelles induced over 50 % tumor regression in HCC1937 BRCA<sup>mut</sup> TNBC xenografts, while the co-administration of the free drugs and the free [ $^{125}$ I]I-PARPi-01 groups showed modest or no therapeutic effect, respectively, compared to the saline control group.
5. Repeated frequent injections of the co-loaded polymeric micelles resulted in body weight loss of up to 10 %, indicating a potential safety risk. However, by reducing the injection frequency to a single administration, the co-loaded micelle formulation showed similarly high antitumor efficacy, reducing the tumors to 50 %



## Conclusions and Outlook

of their initial volumes, while significantly improving tolerability and keeping the mouse body weight constant throughout the treatment course.

6. *Ex vivo* analysis confirmed the co-localization of the polymeric micelles with functional blood vessels and tumor-associated macrophages. Importantly, the co-loaded micelles were capable of efficiently inducing DNA double-strand breaks in tumor cells while minimizing damage to off-target organs.

In summary, this thesis presents the development of a novel and promising nanomedicine-based radio-chemotherapy combination strategy for the treatment of BRCA<sup>mut</sup> TNBC. By integrating nanotechnology with Auger electron-emitting <sup>125</sup>Iodine targeted therapy, this approach aims to enhance therapeutic efficacy and improve patient outcomes.

Ongoing and future work involves dose optimization studies to maximize eventual clinical benefit while maintaining optimal tolerability, as well as distinguishing the contributions of each individual therapeutic agent (radioactive and non-radioactive) to the overall efficacy. This will be evaluated through further *in vivo* studies utilizing polymeric micelles encapsulating only radioactive [<sup>125</sup>I]I-PARPi-01 or non-radioactive I-PARPi-01.

Furthermore, a thorough analysis of the extent and clinical implications of spleen damage observed in our experiments will be conducted via histological examinations. Finally, the possibility of monitoring drug delivery with the nanoformulation through precise imaging techniques further enhances our capacity to tailor treatments to individual patient needs, paving the way for personalized and effective image-guided cancer radio-chemotherapy.

## 5 References

1. Valent, P., et al., *Paul Ehrlich (1854-1915) and His Contributions to the Foundation and Birth of Translational Medicine*. J Innate Immun, 2016. **8**(2): p. 111-20.
2. Strebhardt, K. and A. Ullrich, *Paul Ehrlich's magic bullet concept: 100 years of progress*. Nat Rev Cancer, 2008. **8**(6): p. 473-80.
3. Marin, J.F.G., et al., *Theranostics in Nuclear Medicine: Emerging and Re-emerging Integrated Imaging and Therapies in the Era of Precision Oncology*. RadioGraphics, 2020. **40**(6): p. 1715-1740.
4. Funkhouser, J., *Reinventing pharma: The theranostic revolution*. Current Drug Discovery, 2002: p. 17-19.
5. Lee, D.Y. and K.C. Li, *Molecular theranostics: a primer for the imaging professional*. AJR Am J Roentgenol, 2011. **197**(2): p. 318-24.
6. Duan, H., A. Iagaru, and C.M. Aparici, *Radiotheranostics - Precision Medicine in Nuclear Medicine and Molecular Imaging*. Nanotheranostics, 2022. **6**(1): p. 103-117.
7. Kramer-Marek, G. and J. Capala, *The role of nuclear medicine in modern therapy of cancer*. Tumor Biology, 2012. **33**(3): p. 629-640.
8. Aboagye, E.O., T.D. Barwick, and U. Haberkorn, *Radiotheranostics in oncology: Making precision medicine possible*. CA: A Cancer Journal for Clinicians, 2023. **73**(3): p. 255-274.
9. *News of Science*. Science, 1957. **125**(3236): p. 18-22.
10. Kassis, A.I. and S.J. Adelstein, *Radiobiologic principles in radionuclide therapy*. J Nucl Med, 2005. **46 Suppl 1**: p. 4s-12s.
11. Lehrer, E.J., et al., *Safety and Survival Rates Associated With Ablative Stereotactic Radiotherapy for Patients With Oligometastatic Cancer: A Systematic Review and Meta-analysis*. JAMA Oncol, 2021. **7**(1): p. 92-106.
12. Reubi, J.C. and B. Waser, *Concomitant expression of several peptide receptors in neuroendocrine tumours: molecular basis for in vivo multireceptor tumour targeting*. Eur J Nucl Med Mol Imaging, 2003. **30**(5): p. 781-93.
13. Pomykala, K.L., et al., *Next generation radiotheranostics promoting precision medicine*. Ann Oncol, 2023. **34**(6): p. 507-519.
14. Stokke, C., M. Kvassheim, and J. Blakkisrud, *Radionuclides for Targeted Therapy: Physical Properties*. Molecules, 2022. **27**(17).
15. Donoghue, J.A.O. and T.E. Wheldon, *Targeted radiotherapy using Auger electron emitters*. Physics in Medicine & Biology, 1996. **41**(10): p. 1973.
16. Howell, R.W., *Advancements in the use of Auger electrons in science and medicine during the period 2015–2019*. International Journal of Radiation Biology, 2023. **99**(1): p. 2-27.
17. Chen, P., et al., *Nuclear localizing sequences promote nuclear translocation and enhance the radiotoxicity of the anti-CD33 monoclonal antibody HuM195 labeled with <sup>111</sup>In in human myeloid leukemia cells*. J Nucl Med, 2006. **47**(5): p. 827-36.

## References

18. Morgenroth, A., et al., *Neural Stem Cells as Carriers of Nucleoside-Conjugated Nanogels: A New Approach toward Cell-Mediated Delivery*. ACS Applied Materials & Interfaces, 2023. **15**(18): p. 21792-21803.
19. Sankaranarayanan, R.A., et al., *Correction: Sankaranarayanan et al. Auger Emitter Conjugated PARP Inhibitor for Therapy in Triple Negative Breast Cancers: A Comparative In-Vitro Study*. Cancers 2022, 14, 230. Cancers, 2023. **15**(9): p. 2641.
20. Bohdiewicz, P.J., *Indium-111 satumomab pendetide: the first FDA-approved monoclonal antibody for tumor imaging*. J Nucl Med Technol, 1998. **26**(3): p. 155-63; quiz 170-1.
21. Li, M., R. Zelchan, and A. Orlova, *The Performance of FDA-Approved PET Imaging Agents in the Detection of Prostate Cancer*. Biomedicines, 2022. **10**(10).
22. Wan, N. and M.I. Travin, *Cardiac Imaging With (123)I-meta-iodobenzylguanidine and Analogous PET Tracers: Current Status and Future Perspectives*. Semin Nucl Med, 2020. **50**(4): p. 331-348.
23. Konijnenberg, M.W., et al., *A stylized computational model of the rat for organ dosimetry in support of preclinical evaluations of peptide receptor radionuclide therapy with (90)Y, (111)In, or (177)Lu*. J Nucl Med, 2004. **45**(7): p. 1260-9.
24. Barone, R., et al., *Therapy using labelled somatostatin analogues: comparison of the absorbed doses with 111In-DTPA-D-Phe1-octreotide and yttrium-labelled DOTA-D-Phe1-Tyr3-octreotide*. Nucl Med Commun, 2008. **29**(3): p. 283-90.
25. Siegel, R.L., et al., *Cancer statistics, 2022*. CA: A Cancer Journal for Clinicians, 2022. **72**(1): p. 7-33.
26. Ataollahi, M.R., et al., *Breast cancer and associated factors: a review*. J Med Life, 2015. **8**(Spec Iss 4): p. 6-11.
27. Yedjou, C.G., et al., *Assessing the Racial and Ethnic Disparities in Breast Cancer Mortality in the United States*. Int J Environ Res Public Health, 2017. **14**(5).
28. Arbeitsgemeinschaft Gynäkologische Onkologie e.V. *Diagnosis and Treatment of Patients with early and advanced Breast Cancer*. 2024 09.05.2024; Available from: [https://www.ago-online.de/fileadmin/ago-online/downloads/leitlinien/kommission\\_mamma/2024/englisch/Einzeldateien\\_Literatur/AGO\\_2024E\\_03\\_Early\\_Detection\\_and\\_Diagnosis\\_REF.pdf](https://www.ago-online.de/fileadmin/ago-online/downloads/leitlinien/kommission_mamma/2024/englisch/Einzeldateien_Literatur/AGO_2024E_03_Early_Detection_and_Diagnosis_REF.pdf).
29. Duffy, M.J., et al., *Clinical use of biomarkers in breast cancer: Updated guidelines from the European Group on Tumor Markers (EGTM)*. Eur J Cancer, 2017. **75**: p. 284-298.
30. Schneeweiss, A., et al., *Diagnosis and Therapy of Triple-Negative Breast Cancer (TNBC) - Recommendations for Daily Routine Practice*. Geburtshilfe Frauenheilkd, 2019. **79**(6): p. 605-617.
31. Dent, R., et al., *Triple-negative breast cancer: clinical features and patterns of recurrence*. Clin Cancer Res, 2007. **13**(15 Pt 1): p. 4429-34.
32. Ellsworth, D.L., C.E. Turner, and R.E. Ellsworth, *A Review of the Hereditary Component of Triple Negative Breast Cancer: High- and Moderate-Penetrance Breast Cancer Genes, Low-Penetrance Loci, and the Role of Nontraditional Genetic Elements*. J Oncol, 2019. **2019**: p. 4382606.
33. Lehmann, B.D., et al., *Identification of human triple-negative breast cancer subtypes and preclinical models for selection of targeted therapies*. J Clin Invest, 2011. **121**(7): p. 2750-67.

## References

34. Lin, N.U., et al., *Clinicopathologic features, patterns of recurrence, and survival among women with triple-negative breast cancer in the National Comprehensive Cancer Network*. Cancer, 2012. **118**(22): p. 5463-72.
35. Mehanna, J., et al., *Triple-negative breast cancer: current perspective on the evolving therapeutic landscape*. Int J Womens Health, 2019. **11**: p. 431-437.
36. Boerner, J.L., et al., *Protein expression of DNA damage repair proteins dictates response to topoisomerase and PARP inhibitors in triple-negative breast cancer*. PLoS One, 2015. **10**(3): p. e0119614.
37. Lee, K.J., et al., *Exploiting DNA repair defects in triple negative breast cancer to improve cell killing*. Therapeutic Advances in Medical Oncology, 2020. **12**: p. 1758835920958354.
38. Shiovitz, S. and L.A. Korde, *Genetics of breast cancer: a topic in evolution*. Ann Oncol, 2015. **26**(7): p. 1291-9.
39. Hall, J.M., et al., *Linkage of early-onset familial breast cancer to chromosome 17q21*. Science, 1990. **250**(4988): p. 1684-9.
40. Wooster, R., et al., *Localization of a breast cancer susceptibility gene, BRCA2, to chromosome 13q12-13*. Science, 1994. **265**(5181): p. 2088-90.
41. Antoniou, A., et al., *Average risks of breast and ovarian cancer associated with BRCA1 or BRCA2 mutations detected in case Series unselected for family history: a combined analysis of 22 studies*. Am J Hum Genet, 2003. **72**(5): p. 1117-30.
42. Chen, S. and G. Parmigiani, *Meta-analysis of BRCA1 and BRCA2 penetrance*. J Clin Oncol, 2007. **25**(11): p. 1329-33.
43. King, M.C., J.H. Marks, and J.B. Mandell, *Breast and ovarian cancer risks due to inherited mutations in BRCA1 and BRCA2*. Science, 2003. **302**(5645): p. 643-6.
44. Venkitaraman, A.R., *Cancer suppression by the chromosome custodians, BRCA1 and BRCA2*. Science, 2014. **343**(6178): p. 1470-5.
45. Moynahan, M.E. and M. Jasin, *Mitotic homologous recombination maintains genomic stability and suppresses tumorigenesis*. Nature Reviews Molecular Cell Biology, 2010. **11**(3): p. 196-207.
46. Lieber, M.R., *NHEJ and its backup pathways in chromosomal translocations*. Nature Structural & Molecular Biology, 2010. **17**(4): p. 393-395.
47. Lord, C.J. and A. Ashworth, *The DNA damage response and cancer therapy*. Nature, 2012. **481**(7381): p. 287-294.
48. Roy, R., J. Chun, and S.N. Powell, *BRCA1 and BRCA2: different roles in a common pathway of genome protection*. Nat Rev Cancer, 2011. **12**(1): p. 68-78.
49. Byrski, T., et al., *Response to neo-adjuvant chemotherapy in women with BRCA1-positive breast cancers*. Breast Cancer Research and Treatment, 2008. **108**(2): p. 289-296.
50. Kirk, R., *Cancer risk reduction in BRCA mutation carriers*. Nature Reviews Clinical Oncology, 2010. **7**(11): p. 609-609.
51. Musolino, A., et al., *BRCA mutations, molecular markers, and clinical variables in early-onset breast cancer: A population-based study*. The Breast, 2007. **16**(3): p. 280-292.
52. Noguchi, S., et al., *Clinicopathologic analysis of BRCA1- or BRCA2-associated hereditary breast carcinoma in Japanese women*. Cancer, 1999. **85**(10): p. 2200-5.
53. Hartman, A.-R., et al., *Prevalence of BRCA mutations in an unselected population of triple-negative breast cancer*. Cancer, 2012. **118**(11): p. 2787-2795.

## References

54. Chen, H., et al., *Association Between BRCA Status and Triple-Negative Breast Cancer: A Meta-Analysis*. Front Pharmacol, 2018. **9**: p. 909.
55. Comen, E., et al., *Relative contributions of BRCA1 and BRCA2 mutations to "triple-negative" breast cancer in Ashkenazi Women*. Breast Cancer Res Treat, 2011. **129**(1): p. 185-90.
56. Maegawa, R.O. and S.C. Tang, *Triple-negative breast cancer: unique biology and its management*. Cancer Invest, 2010. **28**(8): p. 878-83.
57. Wu, M., et al., *Serum p53 protein and anti-p53 antibodies are associated with increased cancer risk: a case-control study of 569 patients and 879 healthy controls*. Mol Biol Rep, 2010. **37**(1): p. 339-43.
58. Bryant, H.E., et al., *Specific killing of BRCA2-deficient tumours with inhibitors of poly(ADP-ribose) polymerase*. Nature, 2005. **434**(7035): p. 913-917.
59. Farmer, H., et al., *Targeting the DNA repair defect in BRCA mutant cells as a therapeutic strategy*. Nature, 2005. **434**(7035): p. 917-921.
60. Mateo, J., et al., *A decade of clinical development of PARP inhibitors in perspective*. Annals of Oncology, 2019. **30**(9): p. 1437-1447.
61. Yap, T.A., et al., *Envisioning the future of early anticancer drug development*. Nature Reviews Cancer, 2010. **10**(7): p. 514-523.
62. Fong, P.C., et al., *Inhibition of poly (ADP-ribose) polymerase in tumors from BRCA mutation carriers*. New England Journal of Medicine, 2009. **361**(2): p. 123-134.
63. U.S. Food & Drug Administration. *FDA approves olaparib for germline BRCA-mutated metastatic breast cancer*. 2018 [cited 2024 27/06/2024]; Available from: <https://www.fda.gov/drugs/resources-information-approved-drugs/fda-approves-olaparib-germline-brca-mutated-metastatic-breast-cancer>.
64. U.S. Food & Drug Administration. *FDA approves talazoparib for gBRCAm HER2-negative locally advanced or metastatic breast cancer*. 2018 [cited 2024 27/06/2024]; Available from: <https://wayback.archive-it.org/7993/20201222064856/https://www.fda.gov/drugs/drug-approvals-and-databases/fda-approves-talazoparib-gbrcam-her2-negative-locally-advanced-or-metastatic-breast-cancer>.
65. D'Andrea, A.D., *Mechanisms of PARP inhibitor sensitivity and resistance*. DNA Repair (Amst), 2018. **71**: p. 172-176.
66. Beck, C., et al., *Poly(ADP-ribose) polymerases in double-strand break repair: focus on PARP1, PARP2 and PARP3*. Exp Cell Res, 2014. **329**(1): p. 18-25.
67. Shen, Y., M. Aoyagi-Scharber, and B. Wang, *Trapping Poly(ADP-Ribose) Polymerase*. J Pharmacol Exp Ther, 2015. **353**(3): p. 446-57.
68. Mandapati, A. and K.E. Lukong, *Triple negative breast cancer: approved treatment options and their mechanisms of action*. J Cancer Res Clin Oncol, 2023. **149**(7): p. 3701-3719.
69. Sellmyer, M.A., I.K. Lee, and D.A. Mankoff, *Building the Bridge: Molecular Imaging Biomarkers for 21st Century Cancer Therapies*. Journal of Nuclear Medicine, 2021. **62**(12): p. 1672-1676.
70. Jannetti, S.A., et al., *PARP-1-Targeted Radiotherapy in Mouse Models of Glioblastoma*. J Nucl Med, 2018. **59**(8): p. 1225-1233.
71. Adam, M.J. and D.S. Wilbur, *Radiohalogens for imaging and therapy*. Chem Soc Rev, 2005. **34**(2): p. 153-63.

## References

72. Puentes, L.N., M. Makvandi, and R.H. Mach, *Molecular Imaging: PARP-1 and Beyond*. J Nucl Med, 2021. **62**(6): p. 765-770.
73. Makvandi, M., et al., *A PET imaging agent for evaluating PARP-1 expression in ovarian cancer*. J Clin Invest, 2018. **128**(5): p. 2116-2126.
74. McDonald, E.S., et al., *In vivo visualization of PARP inhibitor pharmacodynamics*. JCI Insight, 2021. **6**(8).
75. Michel, L.S., et al., *PET of Poly (ADP-Ribose) Polymerase Activity in Cancer: Preclinical Assessment and First In-Human Studies*. Radiology, 2017. **282**(2): p. 453-463.
76. Ambur Sankaranarayanan, R., et al., *Advancements in PARP1 Targeted Nuclear Imaging and Theranostic Probes*. J Clin Med, 2020. **9**(7).
77. Pirovano, G., et al., *Targeted Brain Tumor Radiotherapy Using an Auger Emitter*. Clin Cancer Res, 2020. **26**(12): p. 2871-2881.
78. Wilson, T., et al., *PARP-targeted Auger therapy in p53 mutant colon cancer xenograft mouse models*. Molecular pharmaceutics, 2021. **18**(9): p. 3418-3428.
79. Ambur Sankaranarayanan, R., et al., *PARP targeted Auger emitter therapy with [(125)I]PARPi-01 for triple-negative breast cancer*. EJNMMI Res, 2022. **12**(1): p. 60.
80. Sankaranarayanan, R.A., et al., *Auger Emitter Conjugated PARP Inhibitor for Therapy in Triple Negative Breast Cancers: A Comparative In-Vitro Study*. Cancers (Basel), 2022. **14**(1).
81. Chan, C.Y., et al., *[(123)I]CC1: A PARP-Targeting, Auger Electron-Emitting Radiopharmaceutical for Radionuclide Therapy of Cancer*. J Nucl Med, 2023. **64**(12): p. 1965-1971.
82. Sreekumar, S., et al., *Preclinical Efficacy of a PARP-1 Targeted Auger-Emitting Radionuclide in Prostate Cancer*. Int J Mol Sci, 2023. **24**(4).
83. Makvandi, M., et al., *Targeting PARP-1 with Alpha-Particles Is Potently Cytotoxic to Human Neuroblastoma in Preclinical Models*. Molecular Cancer Therapeutics, 2019. **18**(7): p. 1195-1204.
84. Dabagian, H., et al., *PARP Targeted Alpha-Particle Therapy Enhances Response to PD-1 Immune-Checkpoint Blockade in a Syngeneic Mouse Model of Glioblastoma*. ACS Pharmacol Transl Sci, 2021. **4**(1): p. 344-351.
85. Riad, A., et al., *PARP Theranostic Auger Emitters Are Cytotoxic in BRCA Mutant Ovarian Cancer and Viable Tumors from Ovarian Cancer Patients Enable Ex-Vivo Screening of Tumor Response*. Molecules, 2020. **25**(24): p. 6029.
86. Destro, G., et al., *A radioiodinated rucaparib analogue as an Auger electron emitter for cancer therapy*. Nucl Med Biol, 2023. **116-117**: p. 108312.
87. Hoffman, S.L.V., et al., *Preclinical studies of a PARP targeted, Meitner-Auger emitting, theranostic radiopharmaceutical for metastatic ovarian cancer*. Nuclear Medicine and Biology, 2023. **122-123**: p. 108368.
88. Guney Eskiler, G., et al., *Synthetically Lethal BMN 673 (Talazoparib) Loaded Solid Lipid Nanoparticles for BRCA1 Mutant Triple Negative Breast Cancer*. Pharm Res, 2018. **35**(11): p. 218.
89. Wu, M., et al., *Olaparib nanoparticles potentiated radiosensitization effects on lung cancer*. Int J Nanomedicine, 2018. **13**: p. 8461-8472.
90. Rangger, C. and R. Haubner, *Radiolabelled Peptides for Positron Emission Tomography and Endoradiotherapy in Oncology*. Pharmaceuticals (Basel), 2020. **13**(2).

## References

91. Ting, G., et al., *Nanotargeted radionuclides for cancer nuclear imaging and internal radiotherapy*. J Biomed Biotechnol, 2010. **2010**.
92. Buzea, C., I.I. Pacheco, and K. Robbie, *Nanomaterials and nanoparticles: Sources and toxicity*. Biointerphases, 2007. **2**(4): p. MR17-MR71.
93. Chen, Z., *Small-molecule delivery by nanoparticles for anticancer therapy*. Trends in molecular medicine, 2010. **16**(12): p. 594-602.
94. Ghezzi, M., et al., *Polymeric micelles in drug delivery: An insight of the techniques for their characterization and assessment in biorelevant conditions*. Journal of Controlled Release, 2021. **332**: p. 312-336.
95. Caddeo, C., et al., *Nanocarriers for antioxidant resveratrol: formulation approach, vesicle self-assembly and stability evaluation*. Colloids and surfaces B: Biointerfaces, 2013. **111**: p. 327-332.
96. Younis, M.A., et al., *Clinical translation of nanomedicines: Challenges, opportunities, and keys*. Adv Drug Deliv Rev, 2022. **181**: p. 114083.
97. Yoo, J.W., E. Chambers, and S. Mitragotri, *Factors that control the circulation time of nanoparticles in blood: challenges, solutions and future prospects*. Curr Pharm Des, 2010. **16**(21): p. 2298-307.
98. Desai, P., et al., *Tuning the Elasticity of Nanogels Improves Their Circulation Time by Evading Immune Cells*. Angew Chem Int Ed Engl, 2022. **61**(20): p. e202116653.
99. Hussain, Z., et al., *PEGylation: a promising strategy to overcome challenges to cancer-targeted nanomedicines: a review of challenges to clinical transition and promising resolution*. Drug Delivery and Translational Research, 2019. **9**(3): p. 721-734.
100. Knop, K., et al., *Poly(ethylene glycol) in Drug Delivery: Pros and Cons as Well as Potential Alternatives*. Angewandte Chemie International Edition, 2010. **49**(36): p. 6288-6308.
101. Farzin, L., et al., *An overview of nanoscale radionuclides and radiolabeled nanomaterials commonly used for nuclear molecular imaging and therapeutic functions*. Journal of Biomedical Materials Research Part A, 2019. **107**(1): p. 251-285.
102. Garcia, J., T. Tang, and A.Y. Louie, *Nanoparticle-based multimodal PET/MRI probes*. Nanomedicine, 2015. **10**(8): p. 1343-1359.
103. Matsumura, Y. and H. Maeda, *A new concept for macromolecular therapeutics in cancer chemotherapy: mechanism of tumoritropic accumulation of proteins and the antitumor agent smancs*. Cancer research, 1986. **46**(12\_Part\_1): p. 6387-6392.
104. Kirpotin, D.B., et al., *Antibody targeting of long-circulating lipidic nanoparticles does not increase tumor localization but does increase internalization in animal models*. Cancer Res, 2006. **66**(13): p. 6732-40.
105. Chen, W.C., A.X. Zhang, and S.-D. Li, *Limitations and niches of the active targeting approach for nanoparticle drug delivery*. European Journal of Nanomedicine, 2012. **4**(2-4): p. 89-93.
106. Bazak, R., et al., *Cancer active targeting by nanoparticles: a comprehensive review of literature*. J Cancer Res Clin Oncol, 2015. **141**(5): p. 769-84.
107. Zhao, Y., et al., *Gold Nanoparticles Doped with (199) Au Atoms and Their Use for Targeted Cancer Imaging by SPECT*. Adv Healthc Mater, 2016. **5**(8): p. 928-35.



## References

108. Pang, B., et al., *<sup>64</sup>Cu-Doped PdCu@Au Tripods: A Multifunctional Nanomaterial for Positron Emission Tomography and Image-Guided Photothermal Cancer Treatment*. ACS Nano, 2016. **10**(3): p. 3121-31.
109. Heo, G.S., et al., *Assessment of Copper Nanoclusters for Accurate in Vivo Tumor Imaging and Potential for Translation*. ACS Appl Mater Interfaces, 2019. **11**(22): p. 19669-19678.
110. Ilyas, S., et al., *Validation of Dual-Action Chemo-Radio-Labeled Nanocarriers with High Efficacy against Triple-Negative Breast Cancer*. ACS Appl Mater Interfaces, 2023. **15**(42): p. 48963-48977.
111. Wen, H., et al., *A PEG-assisted membrane coating to prepare biomimetic mesoporous silicon for PET/CT imaging of triple-negative breast cancer*. International Journal of Pharmaceutics, 2024. **652**: p. 123764.
112. Gibbens-Bandala, B., et al., *<sup>177</sup>Lu-Bombesin-PLGA (paclitaxel): A targeted controlled-release nanomedicine for bimodal therapy of breast cancer*. Materials Science and Engineering: C, 2019. **105**: p. 110043.
113. Marshall, S.K., et al., *Evaluation of Single Dose and Fractionated Dose of I-131 Radiolabeled Nanoparticles for Triple-Negative Breast Cancer Treatment*. Biomedicines, 2023. **11**(8).
114. Sadeghzadeh, M., et al., *P-210 - Development of <sup>89</sup>Zr-radiolabeled paclitaxel-loaded polymeric micelles for potential applications in personalized treatment of triple-negative breast cancer*. Nuclear Medicine and Biology, 2022. **108-109**: p. S163-S164.
115. Qian, R., et al., *Minimizing adverse effects of Cerenkov radiation induced photodynamic therapy with transformable photosensitizer-loaded nanovesicles*. Journal of Nanobiotechnology, 2022. **20**(1): p. 203.
116. Hajiramezanali, M., et al., *(<sup>68</sup>Ga)-radiolabeled bombesin-conjugated to trimethyl chitosan-coated superparamagnetic nanoparticles for molecular imaging: preparation, characterization and biological evaluation*. Int J Nanomedicine, 2019. **14**: p. 2591-2605.
117. Lahooti, A., S. Shanehsazzadeh, and S. Laurent, *Preliminary studies of (<sup>68</sup>Ga)-NODA-USPION-BBN as a dual-modality contrast agent for use in positron emission tomography/magnetic resonance imaging*. Nanotechnology, 2020. **31**(1): p. 015102.
118. Presant, C.A., A.F. Turner, and R.T. Proffitt, *Potential for improvement in clinical decision-making: tumor imaging with in-111 labeled liposomes results of a phase ii-iii study*. Journal of liposome research, 1994. **4**(2): p. 985-1008.
119. Jensen, G.M. and D.F. Hodgson, *Opportunities and challenges in commercial pharmaceutical liposome applications*. Adv Drug Deliv Rev, 2020. **154-155**: p. 2-12.
120. Gommans, G.M., et al., *<sup>99m</sup>Tc Nanocoll: a radiopharmaceutical for sentinel node localisation in breast cancer--in vitro and in vivo results*. Appl Radiat Isot, 2009. **67**(9): p. 1550-8.
121. Alazraki, N.P., et al., *Lymphoscintigraphy, the sentinel node concept, and the intraoperative gamma probe in melanoma, breast cancer, and other potential cancers*. Semin Nucl Med, 1997. **27**(1): p. 55-67.
122. Thakor, A.S., et al., *Clinically Approved Nanoparticle Imaging Agents*. J Nucl Med, 2016. **57**(12): p. 1833-1837.



## References

123. Pijeira, M.S.O., et al., *Radiolabeled nanomaterials for biomedical applications: radiopharmacy in the era of nanotechnology*. EJNMMI Radiopharm Chem, 2022. **7**(1): p. 8.
124. Wicki, A., et al., *Nanomedicine in cancer therapy: challenges, opportunities, and clinical applications*. Journal of controlled release, 2015. **200**: p. 138-157.
125. Wu, L.-P., D. Wang, and Z. Li, *Grand challenges in nanomedicine*. Materials Science and Engineering: C, 2020. **106**: p. 110302.
126. Aillon, K.L., et al., *Effects of nanomaterial physicochemical properties on in vivo toxicity*. Advanced drug delivery reviews, 2009. **61**(6): p. 457-466.
127. Mihyar, R., et al., *Microfluidic formulation, cryoprotection and long-term stability of paclitaxel-loaded  $\pi$  electron-stabilized polymeric micelles*. Journal of Controlled Release, 2024. **375**: p. 614-626.
128. Bodei, L., et al., *Radiotheranostics in oncology: current challenges and emerging opportunities*. Nat Rev Clin Oncol, 2022. **19**(8): p. 534-550.
129. Sargazi, S., et al., *Active Targeted Nanoparticles for Delivery of Poly(ADP-ribose) Polymerase (PARP) Inhibitors: A Preliminary Review*. Int J Mol Sci, 2021. **22**(19).
130. Mensah, L.B., et al., *Layer-by-layer nanoparticles for novel delivery of cisplatin and PARP inhibitors for platinum-based drug resistance therapy in ovarian cancer*. Bioeng Transl Med, 2019. **4**(2): p. e10131.
131. Caster, J.M., et al., *Nanoparticle delivery of chemosensitizers improve chemotherapy efficacy without incurring additional toxicity*. Nanoscale, 2015. **7**(6): p. 2805-11.
132. Cheng, H.W., et al., *Dextran-modified Quercetin-Cu(II)/hyaluronic acid nanomedicine with natural poly(ADP-ribose) polymerase inhibitor and dual targeting for programmed synthetic lethal therapy in triple-negative breast cancer*. J Control Release, 2021. **329**: p. 136-147.
133. Neufeld, M.J., et al., *Co-delivery of PARP and PI3K inhibitors by nanoscale metal-organic frameworks for enhanced tumor chemoradiation*. Nano Research, 2019. **12**: p. 3003-3017.
134. Kopeček, J. and P. Kopečková, *HPMA copolymers: Origins, early developments, present, and future*. Advanced Drug Delivery Reviews, 2010. **62**(2): p. 122-149.
135. Cabral, H., et al., *Block Copolymer Micelles in Nanomedicine Applications*. Chemical Reviews, 2018. **118**(14): p. 6844-6892.
136. Varela-Moreira, A., et al., *Clinical application of polymeric micelles for the treatment of cancer*. Materials Chemistry Frontiers, 2017. **1**(8): p. 1485-1501.
137. Hwang, D., J.D. Ramsey, and A.V. Kabanov, *Polymeric micelles for the delivery of poorly soluble drugs: From nanoformulation to clinical approval*. Adv Drug Deliv Rev, 2020. **156**: p. 80-118.
138. Cho, H., T.C. Lai, and G.S. Kwon, *Poly(ethylene glycol)-block-poly( $\epsilon$ -caprolactone) micelles for combination drug delivery: evaluation of paclitaxel, cyclophosphamide and gossypol in intraperitoneal xenograft models of ovarian cancer*. J Control Release, 2013. **166**(1): p. 1-9.
139. Torchilin, V.P., *Micellar nanocarriers: pharmaceutical perspectives*. Pharm Res, 2007. **24**(1): p. 1-16.
140. Shi, Y., et al., *Complete Regression of Xenograft Tumors upon Targeted Delivery of Paclitaxel via  $\pi$ - $\pi$  Stacking Stabilized Polymeric Micelles*. ACS Nano, 2015. **9**(4): p. 3740-52.

## References

141. Shalmani, A.A., et al., *Tunable polymeric micelles for taxane and corticosteroid co-delivery*. Drug Deliv Transl Res, 2024. **14**(10): p. 2642-2654.
142. Zhang, D., et al., *Nanoformulated Talazoparib enhances the efficacy and reduces the toxicity of this PARP inhibitor in a preclinical model of BRCA-deficient breast cancer*. The FASEB Journal, 2018. **32**: p. 565.10-565.10.
143. Belz, J.E., et al., *Sustained Release Talazoparib Implants for Localized Treatment of BRCA1-deficient Breast Cancer*. Theranostics, 2017. **7**(17): p. 4340-4349.
144. Li, D., et al., *Enhanced Anti-Cancer Effect of Folate-Conjugated Olaparib Nanoparticles Combined with Radiotherapy in Cervical Carcinoma*. Int J Nanomedicine, 2020. **15**: p. 10045-10058.
145. McCrorie, P., et al., *Etoposide and olaparib polymer-coated nanoparticles within a bioadhesive sprayable hydrogel for post-surgical localised delivery to brain tumours*. Eur J Pharm Biopharm, 2020. **157**: p. 108-120.
146. Landry, M.R., et al., *Low dose novel PARP-PI3K inhibition via nanoformulation improves colorectal cancer immunoradiotherapy*. Mater Today Bio, 2020. **8**: p. 100082.
147. Magalhães, J.A., et al., *Co-Encapsulation of Methylene Blue and PARP-Inhibitor into Poly(Lactic-Co-Glycolic Acid) Nanoparticles for Enhanced PDT of Cancer*. Nanomaterials (Basel), 2021. **11**(6).
148. Misra, R., et al., *Establishing the promising role of novel combination of triple therapeutics delivery using polymeric nanoparticles for Triple negative breast cancer therapy*. Bioimpacts, 2021. **11**(3): p. 199-207.
149. Yang, Y., et al., *In Vitro and Circulation Kinetic Studies on  $\pi$ - $\pi$ -stacked Poly ( $\epsilon$ -caprolactone)-based Micelles Loaded with Olaparib*. Oncology Advances, 2024. **2**(1): p. 1-9.
150. Amreddy, N., et al., *Polymeric Nanoparticle-Mediated Gene Delivery for Lung Cancer Treatment*. Top Curr Chem (Cham), 2017. **375**(2): p. 35.
151. U.S. Food and Drug Administration. *Lynparza prescribing information*. 2017; Available from: [https://www.accessdata.fda.gov/drugsatfda\\_docs/label/2017/208558s000lbl.pdf](https://www.accessdata.fda.gov/drugsatfda_docs/label/2017/208558s000lbl.pdf).
152. Gao, Z., L. Zhang, and Y. Sun, *Nanotechnology applied to overcome tumor drug resistance*. J Control Release, 2012. **162**(1): p. 45-55.
153. Sofias, A.M. and T. Lammers, *Multidrug nanomedicine*. Nature Nanotechnology, 2023. **18**(2): p. 104-106.
154. Letchford, K. and H.M. Burt, *Copolymer micelles and nanospheres with different in vitro stability demonstrate similar paclitaxel pharmacokinetics*. Mol Pharm, 2012. **9**(2): p. 248-60.
155. Miller, T., et al., *Premature drug release of polymeric micelles and its effects on tumor targeting*. Int J Pharm, 2013. **445**(1-2): p. 117-24.
156. Gaucher, G., et al., *Effect of poly(N-vinyl-pyrrolidone)-block-poly(D,L-lactide) as coating agent on the opsonization, phagocytosis, and pharmacokinetics of biodegradable nanoparticles*. Biomacromolecules, 2009. **10**(2): p. 408-16.
157. Letchford, K., et al., *In vitro human plasma distribution of nanoparticulate paclitaxel is dependent on the physicochemical properties of poly(ethylene glycol)-block-poly(caprolactone) nanoparticles*. Eur J Pharm Biopharm, 2009. **71**(2): p. 196-206.

## References

158. van Nostrum, C.F., *Covalently cross-linked amphiphilic block copolymer micelles*. Soft Matter, 2011. **7**(7): p. 3246-3259.
159. Talelli, M., et al., *Polymeric micelles for cancer therapy: 3 C's to enhance efficacy*. Current Opinion in Solid State & Materials Science, 2012. **16**: p. 302-309.
160. Talelli, M., et al., *Core-crosslinked polymeric micelles with controlled release of covalently entrapped doxorubicin*. Biomaterials, 2010. **31**(30): p. 7797-804.
161. Soga, O., et al., *Physicochemical characterization of degradable thermosensitive polymeric micelles*. Langmuir : the ACS journal of surfaces and colloids, 2004. **20** **21**: p. 9388-95.
162. Shi, Y., et al.,  *$\Pi$ - $\pi$  stacking increases the stability and loading capacity of thermosensitive polymeric micelles for chemotherapeutic drugs*. Biomacromolecules, 2013. **14**(6): p. 1826-37.
163. Sheybanifard, M., et al., *Systematic evaluation of design features enables efficient selection of  $\Pi$  electron-stabilized polymeric micelles*. International Journal of Pharmaceutics, 2020. **584**: p. 119409.
164. Altunay, B., et al., *Radiosynthesis, Quality Control, and Small Animal Positron Emission Tomography Imaging of  $^{68}\text{Ga}$ -labelled Nano Molecules*. JoVE, 2024(212): p. e67048.
165. Yuan, F., et al., *Vascular permeability in a human tumor xenograft: molecular size dependence and cutoff size*. Cancer research, 1995. **55**(17): p. 3752-3756.
166. Cabral, H., et al., *Accumulation of sub-100 nm polymeric micelles in poorly permeable tumours depends on size*. Nature nanotechnology, 2011. **6**(12): p. 815-823.
167. Truong, N.P., et al., *The importance of nanoparticle shape in cancer drug delivery*. Expert Opinion on Drug Delivery, 2015. **12**(1): p. 129-142.
168. Geng, Y., et al., *Shape effects of filaments versus spherical particles in flow and drug delivery*. Nat Nanotechnol, 2007. **2**(4): p. 249-55.
169. Gabizon, A., H. Shmeeda, and Y. Barenholz, *Pharmacokinetics of pegylated liposomal Doxorubicin: review of animal and human studies*. Clin Pharmacokinet, 2003. **42**(5): p. 419-36.
170. Zhang, K., et al., *Shape effects of nanoparticles conjugated with cell-penetrating peptides (HIV Tat PTD) on CHO cell uptake*. Bioconjug Chem, 2008. **19**(9): p. 1880-7.
171. Champion, J.A. and S. Mitragotri, *Shape induced inhibition of phagocytosis of polymer particles*. Pharm Res, 2009. **26**(1): p. 244-9.
172. Varela-Moreira, A., et al., *Utilizing in vitro drug release assays to predict in vivo drug retention in micelles*. International Journal of Pharmaceutics, 2022. **618**: p. 121638.
173. Johnston, M.J.W., et al., *Therapeutically optimized rates of drug release can be achieved by varying the drug-to-lipid ratio in liposomal vincristine formulations*. Biochimica et Biophysica Acta (BBA) - Biomembranes, 2006. **1758**(1): p. 55-64.
174. Biancacci, I., et al., *Monitoring EPR Effect Dynamics during Nanotaxane Treatment with Theranostic Polymeric Micelles*. Adv Sci (Weinh), 2022. **9**(10): p. e2103745.
175. Wilson, T.C., et al., *Improved radiosynthesis of  $(^{123}\text{I})\text{-MAPI}$ , an auger theranostic agent*. Int J Radiat Biol, 2023. **99**(1): p. 70-76.

## References

176. *Iodine Radionuclides*, in *RADIOIONIDATION REACTIONS FOR RADIO PHARMACEUTICALS*, H.H. Coenen, J. Mertens, and B. MazieÈRe, Editors. 2006, Springer Netherlands: Dordrecht. p. 5-16.
177. Yoo, J. and Y.-Y. Won, *Phenomenology of the Initial Burst Release of Drugs from PLGA Microparticles*. ACS Biomaterials Science & Engineering, 2020. **6**(11): p. 6053-6062.
178. Tzogani, K., et al., *EMA Review of Daunorubicin and Cytarabine Encapsulated in Liposomes (Vyxeos, CPX-351) for the Treatment of Adults with Newly Diagnosed, Therapy-Related Acute Myeloid Leukemia or Acute Myeloid Leukemia with Myelodysplasia-Related Changes*. Oncologist, 2020. **25**(9): p. e1414-e1420.
179. Asrorov, A.M., et al., *Albumin is a reliable drug-delivering molecule: Highlighting points in cancer therapy*. Medicine in Drug Discovery, 2024. **22**: p. 100186.
180. Guo, X.X., et al., *The efficacy and safety of olaparib in the treatment of cancers: a meta-analysis of randomized controlled trials*. Cancer Manag Res, 2018. **10**: p. 2553-2562.
181. Shalmani, A.A., et al., *Effect of Radical Polymerization Method on Pharmaceutical Properties of  $\Pi$  Electron-Stabilized HPMA-Based Polymeric Micelles*. Biomacromolecules, 2023. **24**(10): p. 4444-4453.
182. Zhu, Y., et al., *Negative surface shielded polymeric micelles with colloidal stability for intracellular endosomal/lysosomal escape*. Molecular pharmaceutics, 2018. **15**(11): p. 5374-5386.
183. Diezi, T.A., Y. Bae, and G.S. Kwon, *Enhanced Stability of PEG-block-poly(N-hexyl stearate l-aspartamide) Micelles in the Presence of Serum Proteins*. Molecular Pharmaceutics, 2010. **7**(4): p. 1355-1360.
184. American Type Culture Collection. *Cell Products*. 31/07/2024]; Available from: <https://www.atcc.org/cell-products#t=productTab&numberOfResults=24>.
185. Lee, J.O., et al., *Metformin overcomes resistance to cisplatin in triple-negative breast cancer (TNBC) cells by targeting RAD51*. Breast Cancer Research, 2019. **21**(1): p. 115.
186. Loibl, S., et al., *PARP expression in early breast cancer and its predictive value for response to neoadjuvant chemotherapy*. Journal of Clinical Oncology, 2010. **28**(15\_suppl): p. 10511-10511.
187. Fröhlich, L.M., et al., *PARP1 expression predicts PARP inhibitor sensitivity and correlates with metastatic potential and overall survival in melanoma*. International Journal of Cancer, 2024. **155**(2): p. 203-210.
188. Rajawat, J., N. Shukla, and D.P. Mishra, *Therapeutic Targeting of Poly(ADP-Ribose) Polymerase-1 (PARP1) in Cancer: Current Developments, Therapeutic Strategies, and Future Opportunities*. Medicinal Research Reviews, 2017. **37**(6): p. 1461-1491.
189. Domagala, P., et al., *PARP-1 expression in breast cancer including BRCA1-associated, triple negative and basal-like tumors: possible implications for PARP-1 inhibitor therapy*. Breast Cancer Research and Treatment, 2011. **127**(3): p. 861-869.
190. Cotter, M.B., et al., *PARP1 in triple-negative breast cancer: Expression and therapeutic potential*. Journal of Clinical Oncology, 2011. **29**(15\_suppl): p. 1061-1061.

## References

191. Makvandi, M., et al., *A Radiotracer Strategy to Quantify PARP-1 Expression In Vivo Provides a Biomarker That Can Enable Patient Selection for PARP Inhibitor Therapy*. Cancer Res, 2016. **76**(15): p. 4516-24.
192. Yang, J., et al., *Cancer metabolism and carcinogenesis*. Experimental Hematology & Oncology, 2024. **13**(1): p. 10.
193. Asim, M., et al., *Synthetic lethality between androgen receptor signalling and the PARP pathway in prostate cancer*. Nature Communications, 2017. **8**(1): p. 374.
194. Cai, D., et al., *Current Development of Nano-Drug Delivery to Target Macrophages*. Biomedicines, 2022. **10**(5): p. 1203.
195. Medrano-Bosch, M., A. Moreno-Lanceta, and P. Melgar-Lesmes, *Nanoparticles to Target and Treat Macrophages: The Ockham's Concept?* Pharmaceuticals, 2021. **13**(9).
196. Bagheri, M., et al., *In Vitro and In Vivo Studies on HPMa-Based Polymeric Micelles Loaded with Curcumin*. Molecular Pharmaceutics, 2021. **18**(3): p. 1247-1263.
197. Zmuda, F., et al., *Synthesis and Evaluation of a Radioiodinated Tracer with Specificity for Poly(ADP-ribose) Polymerase-1 (PARP-1) in Vivo*. J Med Chem, 2015. **58**(21): p. 8683-93.
198. Salinas, B., et al., *Radioiodinated PARP1 tracers for glioblastoma imaging*. EJNMMI Research, 2015. **5**(1): p. 46.
199. Daniel, R.M. and M.J. Danson, *Temperature and the catalytic activity of enzymes: A fresh understanding*. FEBS Letters, 2013. **587**(17): p. 2738-2743.
200. Kumar, A., et al., *Curcumin-loaded lipid nanocarrier for improving bioavailability, stability and cytotoxicity against malignant glioma cells*. Drug Delivery, 2016. **23**(1): p. 214-229.
201. Swinney, D.C., *Chapter 18 - Molecular Mechanism of Action (MMoA) in Drug Discovery*, in *Annual Reports in Medicinal Chemistry*, J.E. Macor, Editor. 2011, Academic Press. p. 301-317.
202. Tobalina, L., et al., *A meta-analysis of reversion mutations in BRCA genes identifies signatures of DNA end-joining repair mechanisms driving therapy resistance*. Ann Oncol, 2021. **32**(1): p. 103-112.
203. Li, X., et al., *PARP inhibitors promote stromal fibroblast activation by enhancing CCL5 autocrine signaling in ovarian cancer*. NPJ Precis Oncol, 2021. **5**(1): p. 49.
204. Keung, M.Y., et al., *Response of Breast Cancer Cells to PARP Inhibitors Is Independent of BRCA Status*. J Clin Med, 2020. **9**(4).
205. Jagtap, P. and C. Szabó, *Poly(ADP-ribose) polymerase and the therapeutic effects of its inhibitors*. Nat Rev Drug Discov, 2005. **4**(5): p. 421-40.
206. Wang, L., et al., *PARP1 in Carcinomas and PARP1 Inhibitors as Antineoplastic Drugs*. International Journal of Molecular Sciences, 2017. **18**(10): p. 2111.
207. Zhang, S., et al., *c-Jun N-terminal kinase mediates hydrogen peroxide-induced cell death via sustained poly(ADP-ribose) polymerase-1 activation*. Cell Death Differ, 2007. **14**(5): p. 1001-10.
208. Wang, F., et al., *PARP1 Upregulation in Recurrent Oral Cancer and Treatment Resistance*. Front Cell Dev Biol, 2021. **9**: p. 804962.
209. Weaver, A.N. and E.S. Yang, *Beyond DNA Repair: Additional Functions of PARP-1 in Cancer*. Front Oncol, 2013. **3**: p. 290.

## References

210. Frizzell, K.M., et al., *Global analysis of transcriptional regulation by poly(ADP-ribose) polymerase-1 and poly(ADP-ribose) glycohydrolase in MCF-7 human breast cancer cells*. J Biol Chem, 2009. **284**(49): p. 33926-38.
211. Simbulan-Rosenthal, C.M., et al., *Misregulation of gene expression in primary fibroblasts lacking poly(ADP-ribose) polymerase*. Proc Natl Acad Sci U S A, 2000. **97**(21): p. 11274-9.
212. Nedeljković, M. and A. Damjanović, *Mechanisms of Chemotherapy Resistance in Triple-Negative Breast Cancer—How We Can Rise to the Challenge*. Cells, 2019. **8**(9): p. 957.
213. Maeda, H., T. Sawa, and T. Konno, *Mechanism of tumor-targeted delivery of macromolecular drugs, including the EPR effect in solid tumor and clinical overview of the prototype polymeric drug SMANCS*. J Control Release, 2001. **74**(1-3): p. 47-61.
214. Anselmo, A.C. and S. Mitragotri, *Nanoparticles in the clinic: An update*. Bioeng Transl Med, 2019. **4**(3): p. e10143.
215. Huynh, E. and G. Zheng, *Cancer nanomedicine: addressing the dark side of the enhanced permeability and retention effect*. Nanomedicine (Lond), 2015. **10**(13): p. 1993-5.
216. Gullberg, G.T., 1.03 - *Dynamic Single-Photon Emission Computed Tomography*, in *Comprehensive Biomedical Physics*, A. Brahme, Editor. 2014, Elsevier: Oxford. p. 61-91.
217. Yu, M. and J. Zheng, *Clearance Pathways and Tumor Targeting of Imaging Nanoparticles*. ACS Nano, 2015. **9**(7): p. 6655-6674.
218. Zhang, Y.-N., et al., *Nanoparticle–liver interactions: Cellular uptake and hepatobiliary elimination*. Journal of Controlled Release, 2016. **240**: p. 332-348.
219. Narum, S.M., et al., *Chapter 4 - Passive targeting in nanomedicine: fundamental concepts, body interactions, and clinical potential*, in *Nanoparticles for Biomedical Applications*, E.J. Chung, L. Leon, and C. Rinaldi, Editors. 2020, Elsevier. p. 37-53.
220. Fang, J., W. Islam, and H. Maeda, *Exploiting the dynamics of the EPR effect and strategies to improve the therapeutic effects of nanomedicines by using EPR effect enhancers*. Adv Drug Deliv Rev, 2020. **157**: p. 142-160.
221. Cavina, L., et al., *Design of Radioiodinated Pharmaceuticals: Structural Features Affecting Metabolic Stability towards in Vivo Deiodination*. European Journal of Organic Chemistry, 2017. **2017**(24): p. 3387-3414.
222. Ross, M.H. and W. Pawlina, *Histology*. 2006: Lippincott Williams & Wilkins.
223. Verger, P., et al., *Iodine Kinetics and Effectiveness of Stable Iodine Prophylaxis After Intake of Radioactive Iodine: A Review*. Thyroid®, 2001. **11**(4): p. 353-360.
224. Wilson, T.C., et al., *PET Imaging of PARP Expression Using (18)F-Olaparib*. J Nucl Med, 2019. **60**(4): p. 504-510.
225. Carlisle, M., A. Cortés, and I.R. McDougall, *Uptake of I-131 in the biliary tract: a potential cause of a false-positive result of scintiscan*. Clin Nucl Med, 1998. **23**(8): p. 524-7.
226. Oh, J.R. and B.C. Ahn, *False-positive uptake on radioiodine whole-body scintigraphy: physiologic and pathologic variants unrelated to thyroid cancer*. Am J Nucl Med Mol Imaging, 2012. **2**(3): p. 362-85.

## References

227. Tsoi, K.M., et al., *Mechanism of hard-nanomaterial clearance by the liver*. Nat Mater, 2016. **15**(11): p. 1212-1221.
228. Tamori, Y., E. Suzuki, and W.-M. Deng, *Epithelial Tumors Originate in Tumor Hotspots, a Tissue-Intrinsic Microenvironment*. PLOS Biology, 2016. **14**(9): p. e1002537.
229. Lewis, C.E. and J.W. Pollard, *Distinct Role of Macrophages in Different Tumor Microenvironments*. Cancer Research, 2006. **66**(2): p. 605-612.
230. Hare, J.I., et al., *Challenges and strategies in anti-cancer nanomedicine development: An industry perspective*. Advanced Drug Delivery Reviews, 2017. **108**: p. 25-38.
231. Arora, G., et al., *Evaluation of cytotoxic and tumor targeting capability of (177)Lu-DOTATATE-nanoparticles: a trailblazing strategy in peptide receptor radionuclide therapy*. Ann Nucl Med, 2016. **30**(5): p. 334-45.
232. Drude, N., et al., *Multistage Passive and Active Delivery of Radiolabeled Nanogels for Superior Tumor Penetration Efficiency*. Biomacromolecules, 2017. **18**(8): p. 2489-2498.
233. Jin, H., L. Wang, and R. Bernards, *Rational combinations of targeted cancer therapies: background, advances and challenges*. Nature Reviews Drug Discovery, 2023. **22**(3): p. 213-234.
234. Jaaks, P., et al., *Effective drug combinations in breast, colon and pancreatic cancer cells*. Nature, 2022. **603**(7899): p. 166-173.
235. Gelderblom, H., et al., *Cremophor EL: the drawbacks and advantages of vehicle selection for drug formulation*. European Journal of Cancer, 2001. **37**(13): p. 1590-1598.
236. Patel, M., et al., *The role of poly(ADP-ribose) polymerase inhibitors in the treatment of cancer and methods to overcome resistance: a review*. Cell Biosci, 2020. **10**: p. 35.
237. Yakuzo, H.M.S.T.S., Emilia; Shaari, Rumaizi; Yaacob, Nik Soriani, *Correlation of Tumour Response with Starting Tumour Size and Dose of Tamoxifen in an N-Methyl-N-Nitrosourea (NMU)-Induced Rat Mammary Cancer Model*. Asian Pacific Journal of Cancer Prevention, 2014. **15**(16): p. 6721-6726.
238. Abe, I., et al., *Some aspects of size-dependent differential drug response in primary and metastatic tumors*. Cancer and Metastasis Reviews, 1985. **4**(1): p. 27-39.
239. Kuo, L.J. and L.X. Yang, *Gamma-H2AX - a novel biomarker for DNA double-strand breaks*. In Vivo, 2008. **22**(3): p. 305-9.
240. Rose, M., et al., *PARP Inhibitors: Clinical Relevance, Mechanisms of Action and Tumor Resistance*. Front Cell Dev Biol, 2020. **8**: p. 564601.
241. Ngo, W., et al., *Why nanoparticles prefer liver macrophage cell uptake in vivo*. Advanced Drug Delivery Reviews, 2022. **185**: p. 114238.
242. Blanco, E., H. Shen, and M. Ferrari, *Principles of nanoparticle design for overcoming biological barriers to drug delivery*. Nat Biotechnol, 2015. **33**(9): p. 941-51.
243. Cooley, M., et al., *Influence of particle size and shape on their margination and wall-adhesion: implications in drug delivery vehicle design across nano-to-micro scale*. Nanoscale, 2018. **10**(32): p. 15350-15364.
244. Stroeve, P.A.M., Morteza, *Drug Delivery Systems*. Drug Delivery Systems.

## References

245. Hoshyar, N., et al., *The effect of nanoparticle size on in vivo pharmacokinetics and cellular interaction*. Nanomedicine (Lond), 2016. **11**(6): p. 673-92.
246. Wilhelm, S., et al., *Analysis of nanoparticle delivery to tumours*. Nature Reviews Materials, 2016. **1**(5): p. 16014.
247. Thurston, G., et al., *Permeability-related changes revealed at endothelial cell borders in inflamed venules by lectin binding*. Am J Physiol, 1996. **271**(6 Pt 2): p. H2547-62.
248. Hunter, F., et al., *Rhodamine-RCA in vivo labeling guided laser capture microdissection of cancer functional angiogenic vessels in a murine squamous cell carcinoma mouse model*. Mol Cancer, 2006. **5**: p. 5.
249. Nakamura-Ishizu, A., et al., *Characterization of sinusoidal endothelial cells of the liver and bone marrow using an intravital lectin injection method*. J Mol Histol, 2008. **39**(5): p. 471-9.
250. Biancacci, I., et al., *Repurposing Tamoxifen for Tumor Microenvironment Priming and Enhanced Tumor-Targeted Drug Delivery*. Advanced Therapeutics, 2023. **6**(11): p. 2300098.
251. Sofias, A.M., et al., *Tumor Targeting by  $\alpha v\beta 3$ -Integrin-Specific Lipid Nanoparticles Occurs via Phagocyte Hitchhiking*. ACS Nano, 2020. **14**(7): p. 7832-7846.
252. Momoh, J., et al., *Intravital microscopy for real-time monitoring of drug delivery and nanobiological processes*. Advanced Drug Delivery Reviews, 2022. **189**: p. 114528.
253. Engin, A.B., et al., *Mechanistic understanding of nanoparticles' interactions with extracellular matrix: the cell and immune system*. Part Fibre Toxicol, 2017. **14**(1): p. 22.
254. Lieleg, O., R.M. Baumgärtel, and A.R. Bausch, *Selective filtering of particles by the extracellular matrix: an electrostatic bandpass*. Biophys J, 2009. **97**(6): p. 1569-77.
255. Pluen, A., et al., *Role of tumor-host interactions in interstitial diffusion of macromolecules: cranial vs. subcutaneous tumors*. Proc Natl Acad Sci U S A, 2001. **98**(8): p. 4628-33.
256. Sindhvani, S., et al., *The entry of nanoparticles into solid tumours*. Nature Materials, 2020. **19**(5): p. 566-575.
257. Li, X., et al., *Transvascular transport of nanocarriers for tumor delivery*. Nature Communications, 2024. **15**(1): p. 8172.



## 6 Acknowledgments

I want to express my gratitude to **Prof. Dr. Felix. M. Mottaghy** for the opportunity to pursue my Ph.D. thesis in his group, focusing on such an exciting and challenging topic. Thank you for your belief in my abilities, especially on a project that necessitates expertise from various fields. I truly appreciate your genuine interest in my progress and for taking the time from your busy schedule to discuss my results and provide guidance on data presentation. In addition to our productive scientific discussions, I am also grateful for the warm and supportive work environment you fostered, where I was recognized not only as a researcher but also encouraged to develop my personal skills and interests.

I would like to extend my heartfelt appreciation to my supervisor, **Dr. Agnieszka Morgenroth**. You were always available to answer my questions, brainstorm new ideas, and always gave me scientific freedom. I am incredibly grateful for that. I am truly grateful for your patience, understanding, and support during the challenging moments of my animal experiments. Your guidance has not only directed me professionally but has also positively impacted my personal development. Most importantly, thank you for believing in my ability to carry out this project.

My sincere gratitude to my second supervisor, **Dr. Quim Peña**. Your ability to approach projects from diverse perspectives has greatly improved my understanding and has inspired me to think creatively. This is a skill I aspire to develop in the future. I truly appreciate all the insightful discussions we've had about the project; I always walk away with new knowledge after our conversations. Thank you for consistently taking the time to address all of my questions.

I want to thank my first examiner, **Prof. Dr. Stefan Schillberg**, and my second examiner **Prof. Dr. Andreas Herrmann**, for their fruitful discussions on my project and, of course, for the examination of my Ph.D. thesis.

I am deeply grateful for the opportunity to meet such exceptional mentors through the Research Training Group (RTG) 2375, funded by the Deutsche Forschungsgemeinschaft (DFG). A heartfelt thank you to **Prof. Dr. Fabian Kießling** and **Prof. Dr. Twan Lammers** for this invaluable opportunity and for the constructive feedback you provided throughout my

## Acknowledgments

Ph.D. The skills I have acquired during my doctoral journey were made possible by RTG 2375 and the collaborative training experiences it facilitated.

Moreover, I would like to express my heartfelt gratitude to **Mr. Alec Wang** for dedicating his time to teach me nanochemistry and for always being available to address my questions. Your constructive feedback throughout this project has been invaluable. Collaborating with you felt like working alongside a friend, and I truly appreciate your support and motivation. The nanochemistry aspect of this thesis would not have been possible without your guidance. Thank you!

Lastly, I would like to extend my heartfelt gratitude to **Dr. Dr. Alexandru Florea**. Your patience and guidance in teaching me the proper techniques for working with animals have been invaluable to my development as a researcher. Your unwavering belief in my abilities has been a source of motivation, and your support has truly been heartwarming. I have greatly appreciated our scientific discussions, which have deepened my understanding of the subject matter, as well as our personal conversations, which have made my time in the lab enjoyable and enriching.

The majority of this thesis work would not have been possible without the unwavering support and motivation from everyone in the **nuclear medicine department**. A heartfelt thank you to **Amelie and Betül** for making my time in the labs, as well as outside of them, truly enjoyable! I also want to express my gratitude to Natascha, Sarah, Andreas Vogg, Massoud, Susanne, Andreas Keuhlartz, Steffi, Fabian, Karolin, Najaf and Sabri. Thank you all for the wonderful moments, the engaging conversations, and for fostering such a pleasant working environment.

I would like to express my endless gratitude to my sister **Nina**, who has always stood by my side like a rock and supported me in every situation without hesitation. I am also immensely thankful to my parents, **Dunja and Klaus**, for their unwavering encouragement and support. I hold the deepest appreciation for my parents, who have always prioritized education above all else, motivated me to pursue my dreams, and supported me in every decision I made.

**David, Mara, Melissa, Lisa and Ricarda:** You are truly my greatest supporters. Thank you for always being by my side and for your unwavering belief in me. Your encouragement has meant the world to me, and I am so grateful to have found you and have you for life. I cherish our bond and look forward to sharing many more memories together.